A Physical Model Describing the Transport Mechanisms of Cytoplasmic Dynein

Laurie Elizabeth Trott

August 2016

Submitted for the degree of *Doctor of Philosophy*

University of Sussex

Department of Mathematics, School of Mathematical and Physical Sciences, and School of Life Sciences

Declaration of Submission

I hereby declare that this thesis has not been and will not be, submitted in whole or part to another University for award of any other degree. However, the thesis incorporates to the extent indicated below, material already submitted as part of required coursework and for the degree of:

Masters project consisted of the derivation of the continuous model presented in Chapter 3 and various types of functions were tested within the model, this included the functions given in equations (4.27) - (4.26)*,* (4.29) - (4.32) *and* (4.33) - (4.36) *only.*

In the degree of: *MMath Mathematics*

which was awarded by: *University of Sussex (2012)*

Signature: Laurie E. Trott

UNIVERSITY OF SUSSEX

LAURIE ELIZABETH TROTT

SUBMITTED FOR THE DEGREE OF DOCTOR OF PHILOSOPHY

A PHYSICAL MODEL DESCRIBING THE TRANSPORT MECHANISMS OF CYTOPLASMIC DYNEIN

Summary

Cytoplasmic dynein 1 is crucial for many cellular processes including endocytosis and cell division. Dynein malfunction can lead to neurodevelopmental and neurodegenerative disease, such as intellectual disability, Charcot-Marie-Tooth disease and spinal muscular atrophy with lower extremity predominance. We formulate, based on physical principles, a mechanical model to describe the stepping behaviour of cytoplasmic dynein walking on microtubules. Unlike previous studies on physical models of this nature, we base our formulation on the whole structure of dynein to include the temporal dynamics of the individual components such as the cargo (for example an endosome or bead), two rings of six ATPase domains associated with diverse cellular activities and the microtubule binding domains. This mathematical framework allows us to examine experimental observations across different species of dynein as well as being able to make predictions (not currently experimentally measured) on the temporal behaviour of the individual components of dynein.

Initially, we examine a continuous model using plausible force functions to model the ATP force and binding affinity to the microtubule. Our results show hand-over-hand and shuffling stepping patterns in agreement with experimental observations. We are able to move from a hand-over-hand to a shuffling stepping pattern by changing a single parameter. We also explore the effects of multiple motors.

Next, we explore stochasticity within the model, modelling the binding of ATP as a random event. Our results reflect experimental observations that dynein walks using a predominantly shuffling stepping pattern. Furthermore, we study the effects of mutated dynein and extend the model to include variable step sizes, backward stepping and dwelling. Independent stepping is studied and the results show that coordinated stepping is needed in order to obtain experimental run lengths.

Acknowledgements

I would like to thank Prof. Anotida Madzvamuse for all his encouragement, guidance and insight during my time at Sussex, without whom this work would not have been possible. I would also like to thank Dr. Majid Hafezparast for his advice and knowledge, which has been invaluable to me. Thanks also to Dr. Caroline A. Garrett for all her help and allowing me access to her results.

I am grateful to the School of Mathematical and Physical Sciences and the School of Life Sciences for funding this work and the University of Sussex for funding a JRA position, which was fundamental in setting this work in motion.

Thanks to Tom and my parents for their love and patience over the years.

Contents

List of Abbreviations

AAA+	ATPase domains associated with diverse cellular activities
ADP	Adenosine diphosphate
ADP.Vi	ADP and vanadate
ALS	Amyotrophic lateral sclerosis
Arp1	Actin related protein-1
ASEP	Asymmetric simple exclusion process
ATP	Adenosine triphosphate
CMT2	Charcot-Marie-Tooth disease type 2
Cra1	*Cramping 1*
DYNC1H1	Dynein heavy chain 1
DYNC1I	Dynein intermediate chain
DYNC1LI	Dynein light intermediate chain
DYNLL	Dynein LC8 light chain
DYNLRB	Dynein roadblock light chain
DYNLT	Dynein Tctex-1 light chain
Dynein	Cytoplasmic dynein 1
EGF	Epidermal growth factor
IFT	Intraflagellar transport
Lis1	Lissencephaly 1
Loa	*Legs at odd angles*
MEF	Mouse embryonic fibroblast
MTBD	Microtubule binding domain
NudE	Nuclear distribution E
NudEL	NudE-like
ODE	Ordinary differential equation
Pi	Phosphate

SBMA	Spinal and bulbar muscular atrophy
SMA-LED	Spinal muscular atrophy with lower extremity predominance
Swl	*Sprawling*
Vi	Vanadate

Mathematical Notation: Variables

t	Time
x_A	Position of AAA+ ring A
x_B	Position of AAA+ ring B
x_C	Position of the cargo
x_D	Position of MTBD D
x_E	Position of MTBD E
x_T	Position of the tail domain
y_A	Vertical position of AAA+ ring A
y_B	Vertical position of AAA+ ring B
y_C	Vertical position of the cargo
y_D	Vertical position of MTBD D
y_E	Vertical position of MTBD E
y_T	Vertical position of the tail domain
τ	Non-dimensional time
χ_A	Non-dimensional position of AAA+ ring A
χ_B	Non-dimensional position of AAA+ ring B
χ_C	Non-dimensional position of the cargo
χ_D	Non-dimensional position of MTBD D
χ_E	Non-dimensional position of MTBD E
χ_T	Non-dimensional position of the tail domain
ψ_A	Non-dimensional vertical position of AAA+ ring A
ψ_B	Non-dimensional vertical position of AAA+ ring B
ψ_C	Non-dimensional vertical position of the cargo
ψ_D	Non-dimensional vertical position of MTBD D
ψ_E	Non-dimensional vertical position of MTBD E
ψ_T	Non-dimensional vertical position of the tail domain

Mathematical Notation:

Parameters

d	Maximum separation distance of the MTBDs
F_C	External force acting on the cargo
G	Maximal binding force to the microtubule
H	Maximal force produced by the AAA+ ring
K_{ATP} ($K_{ATP,i}$)	Approximated ATP force: spring constant (for MTBD i)
K_C	Spring constant between the cargo and the tail/AAA+ ring
K_S	Spring constant between the AAA+ ring and the MTBD
K_T	Spring constant between the tail and the AAA+ ring
L_{ATP} ($L_{ATP,i}$)	Approximated ATP force: unstressed length between the binding sites (for MTBD i)
L_C	Unstressed length between the cargo and the tail/AAA+ ring
L_S	Unstressed length between the AAA+ ring and the MTBD
L_T	Unstressed length between the tail and the AAA+ ring
M_C	Mass of the cargo
M_M	Mass of the AAA+ ring
M_S	Mass of the MTBD
M_T	Mass of the tail domain
n	Scale of the step size, i.e. step size given by nL_{ATP}
N	Number of steps
P_{Back}	Probability of random backward stepping
P_D	Probability that MTBD E steps given that MTBD D stepped previously
P_E	Probability that MTBD E steps given that MTBD E stepped previously
p_n	Position of the nth binding site on the microtubule

$\mathbf{q}$	Random vector from the uniform distribution on $(0, 1)$
$\mathbf{q_1}$	Random vector from the exponential distribution with mean μ
$\mathbf{q_2}$, $\mathbf{q_3}$	Random vector from the uniform distribution on $(0, 1)$
q_{Back}	Random number taken from the uniform distribution on $(0, 1)$
$\mathbf{q_D}$, $\mathbf{q_E}$	Random vector from the exponential distribution with mean μ
Q_F	Total time spent dwelling
R_C	Radius of the cargo
R_M	Radius of the AAA+ ring
R_S	Radius of the MTBD
R_T	Radius of the tail domain
t_{bind}	Time when ATP binds to a AAA+ ring
T	End time
T_F	Total time spent stepping
T_{Final}	End time
T_{Step}	Length of stepping time interval
γ_{ATP} ($\gamma_{ATP,i}$)	Approximated ATP force: drag coefficient (for MTBD i)
γ_A	Drag coefficient of AAA+ ring A
γ_B	Drag coefficient of AAA+ ring B
γ_C	Drag coefficient of the cargo
γ_D	Drag coefficient of MTBD D
γ_E	Drag coefficient of MTBD E
γ_T	Drag coefficient of the tail domain
η	Viscosity of the cytoplasm
$\theta_{A,C}$	Angle of the stalk between AAA+ ring A and cargo
$\theta_{A,D}$	Angle of the stalk between AAA+ ring A and MTBD D
$\theta_{A,T}$	Angle of the spring between AAA+ ring A and the tail domain
$\theta_{B,C}$	Angle of the stalk between AAA+ ring B and cargo
$\theta_{B,E}$	Angle of the stalk between AAA+ ring B and MTBD E
$\theta_{B,T}$	Angle of the spring between AAA+ ring B and the tail domain
μ	Mean dwell time
τ_{Final}	Non-dimensional end time
τ_{Step}	Non-dimensional length of stepping time interval

List of Tables

List of Figures

Chapter 1

Introduction

Cytoplasmic dynein 1, a motor protein present in eukaryotic cells, is involved in a vast range of cellular activities in metazoan cells including the transport of a multitude of organelles, cell division, and cell migration (see review [1] for further details). The devastating effect of dynein malfunction presented in mutation studies on mouse models as well as in humans shows the need for greater understanding of the mechanics and processes used by dynein [2, 3, 4, 5]. The dynein family is particularly interesting as it has evolved separately from the other motor protein families, of kinesin and myosin, and has a very different structure and mechanics (see review [6]).

The dynein family includes three classes: cytoplasmic dynein 1, cytoplasmic dynein 2 (or intraflagellar transport (IFT) dynein), and axonemal dyneins [7, 8]. Compared to cytoplasmic dynein 1, cytoplasmic dynein 2 has a slightly different structure and is involved with transport along flagella [7, 8]. Axonemal dynein is involved with the beating of cilia and flagella [7]. There are seven types of axonemal dynein, with both outer and inner arm forms [7, 8]. The main structural difference is that outer arm dynein can have two to three head domains, whilst inner arm dynein can have one to two heads [7, 8]. This thesis will be based on cytoplasmic dynein 1, although this study could be easily extended to cytoplasmic dynein 2 as well as being able to be adapted to study flagella dynein.

Cytoplasmic dynein 1 (hereafter referred to as dynein) is vital to the transportation of cellular cargo such as vesicles, endosomes or organelles in a process known as endocytosis. For example, in mammalian cells epidermal growth factor (EGF) receptors activated by EGF are transported from the cell membrane to the perinucleur region to be degraded or recycled back to the cell membrane (see Figure 1.1 [9]) [10]. Activated EGF receptors are transported in clathrin-coated

vesicles which undergo fusion to form early endosomes [10, 11]. Receptors to be degraded will then be transported in late endosomes which fuse with lysosomes [10, 11, 12]. Endosomes are bidirectional and experience fusion and fission along the endocytic pathway [12, 13, 14].

The endocytic pathway involves the action of motor proteins which attach to the vesicles or endosomes and move along microtubules or actin filaments which form the cytoskeleton. Microtubules are polarised, with the plus-end usually pointing towards the cell membrane, away from the nucleus [11]. Vale *et al.,* suggest a 'toolbox' of five motor proteins required for intracellular transport which includes three types of kinesin, myosin V, and cytoplasmic dynein [15]. Different motor proteins are involved in the process at different stages [13, 16, 17, 18, 19, 20, 21]. Kinesins are motor proteins which usually move towards the plus-end of microtubules, i.e. towards the cell membrane, however there are notable exceptions such as KIFC2 and KIFC3 which are minus-end directed [6, 15, 22]. Myosins move on actin filaments and can be processive, such as myosin V, or non-processive, such as myosin II [6, 15]. It is a topic of debate as to whether motor proteins act on cargoes to pull in different directions, with the resultant movement determined by a tug-of-war effect, or whether there is some switch that enables one type of motor protein to become inactive and then to activate again when needed [14, 23, 24].

The largest components of the dynein complex are two homodimerized heavy chains, each of which is made up of a tail and a motor domain. The N-terminal tail domain (residues 1 to $\sim$1400) binds to other regulatory and structural components of dynein, through which cargo and adaptor proteins bind to the complex. The motor (or head) domain at the C-terminal consists of six ATPase domains associated with diverse cellular activities (AAA+), of which only four are thought to bind ATP, and a microtubule-interacting stalk region [4, 25, 26, 27]. The coupling of ATP hydrolysis and force generation is not yet fully understood, although recent progress has been made with structural cycles being suggested by Carter *et al.,* and Lin *et al.,* [28, 29]. The stalk is formed of an anti-parallel coiled-coil, which extends from between the AAA4 and AAA5 domains ending with a microtubule binding domain (MTBD); a recently identified component labelled a strut or buttress is proposed to support the stalk under load [25, 26, 27].

Dynein moves in the centripetal direction along microtubules, i.e. from the cell membrane towards the nucleus. Research has shown that dynein moves processively, i.e. takes multiple steps without detaching from the microtubule, using a variable step size but with the majority of steps being 8nm in distance [30]. However, this reflects the position of the tail of dynein rather than the motor domain, and further investigations have shown that the motor domain moves with a usual step size of around 16nm [30, 31, 32]. We note that dynein steps are not always parallel

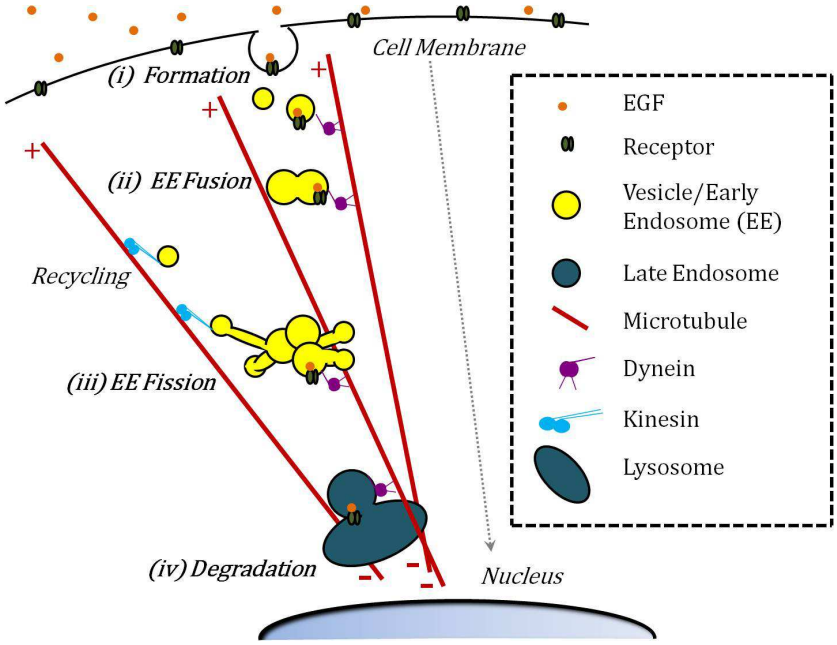

Figure 1.1: From the cell membrane to the nucleus: A schematic diagram of the clathrin-mediated endocytic pathway for EGF receptors. (i) Activated EGF receptors and the surrounding membrane invaginates whilst a clathrin coat forms around it. (ii) The clathrin coat dissembles and the receptors are transported along microtubules in vesicles, which undergo fusion to form early endosomes. (iii) Endosomes undergo fission, resulting in the separation of the contents destined for degradation and those to be recycled back to the cell membrane. (iv) Activated receptors to be degraded will then be transported in late endosomes which fuse with lysosomes. The transport process involves the action of motor proteins which attach to the vesicles or endosomes and move along microtubules. Reproduced from Bulletin of Mathematical Biology, *From the Cell Membrane to the Nucleus: Unearthing Transport Mechanisms for Dynein*, v.7, 2012, p.2032, Laurie Crossley, Caroline A. Garrett, Majid Hafezparast and Anotida Madzvamuse, (© Society of Mathematical Biology 2012) with permission of Springer [9].

to the microtubule and usually have off-axis components [30, 31, 32]. Backwards stepping also occurs, with experiments showing approximately 13% of the total number of steps for a single motor domain. Dynein is seen to dwell between steps, with an average dwell time of 2s best fit to an exponential distribution [30]. Papers by DeWitt *et al.,* and Qiu *et al.,* have found that dynein can use both uncoordinated and co-ordinated stepping, with a random stepping pattern occurring when the distance between the two motor domains is small, and the pattern becoming more co-ordinated as this distance increases; hence it is proposed that tension within dynein may govern its stepping mechanism [31, 32, 33]. Qiu *et al.,* found that 74% of steps taken by dynein alternated in time and that 83% did not pass each other, suggesting that dynein may move predominantly by shuffling rather than in a hand-over-hand fashion [32].

Mutations in cytoplasmic dynein heavy chain 1 (*DYNC1H1*) cause spinal muscular atrophy with lower extremity predominance (SMA-LED), Charcot-Marie-Tooth disease type 2 (CMT2), and intellectual disability (reviewed in ref. [4]; [5, 34]). Investigations into mutations in dynein

have shown particular behavioural differences, such as a decrease in velocity and distance travelled in a mouse strain known as *Legs at odd angles* (*Loa*) [2, 35, 36]. Hafezparast *et al.,* have shown that the *Dync1h1*^{F580Y} mutation in the *Loa* mouse strain negatively affects fast retrograde transport mediated by dynein, including an increase in pauses in motion [2, 3]. Work by Deng *et al.,* has shown that the *Loa* mutation gives rise to a lower affinity of dynein to dynactin [37], which regulates cargo binding and dynein processivity.

In the following chapter we review the relevant literature, looking at what experimental data is available for dynein and discussing significant mathematical models in the field. In Part I we present a continuous model for the motion of dynein along a microtubule. In Chapter 3 we derive the model from first principles and in Chapter 4 we present results for numerical simulations of the model, including model refinements exploring alternative ways to model ATP force and multiple motors. Next, in Part II we look at a stochastic model. We derive a model of continual forward stepping in Chapter 5 and study various numerical simulations. In Chapter 6 we extend the model to consider backward stepping, variable step size and dwelling. In Chapter 7 we look at independent head domains and the effects on run length. The key differences between the stochastic models are presented in Table 1.1. Finally in Chapter 8 we present our conclusions and discuss possible future work.

Chapter/ Section	Step Sizes	Backward Stepping	Dwelling	Multi-scale	Coordinated/Independent Stepping
5	Fixed	No	No	No	Coordinated
6.2	Fixed	Yes	Yes	No	Coordinated
6.3	Variable	Yes	Yes	No	Coordinated
6.4	Variable	Yes	Yes	Yes	Coordinated
7	Fixed	No	Yes	Yes	Independent
7.2.1	Variable	Yes	Yes	Yes	Independent

Table 1.1: Key differences between the stochastic models presented in this study: modelling fixed versus variable step sizes, backward stepping, and dwelling between steps; whether a multi-scale framework is used; modelling coordinated versus independent stepping of the two motor domains.

Chapter 2

Literary Review

The structure, function and behaviour of dynein is a topic at the forefront of current research. Crystallographic structures have only recently revealed the detailed conformations of dynein's motor domain, and the precise mechanisms behind dynein's stepping behaviour are still to be discovered. Below we discuss the relevant literature on dynein's structure, stepping mechanism and behaviour.

2.1 Experimental results for cytoplasmic dynein 1

2.1.1 Structure

Dynein consists of heavy chains, intermediate chains, light intermediate chains and light chains (see Figure 2.1) [1, 15, 38, 39, 40, 41]. Intermediate chains, light intermediate chains and other subunits of dynein have been identified with cargo binding [1, 15, 42]. The motor domain of dynein lies in the heavy chain, and is composed of an AAA+ ring, linker unit, C-sequence domain, stalk, microtubule binding domain (MTBD) and a newly identified component known as a strut or buttress [25, 26, 27, 43] (discussed in [28, 44, 45, 46]).

AAA+ ring

The AAA+ ring is formed of six AAA modules, AAA1 to AAA6 ordered around the central pore, each with structural variations in order to serve different functions [28, 47, 56]. Every module is

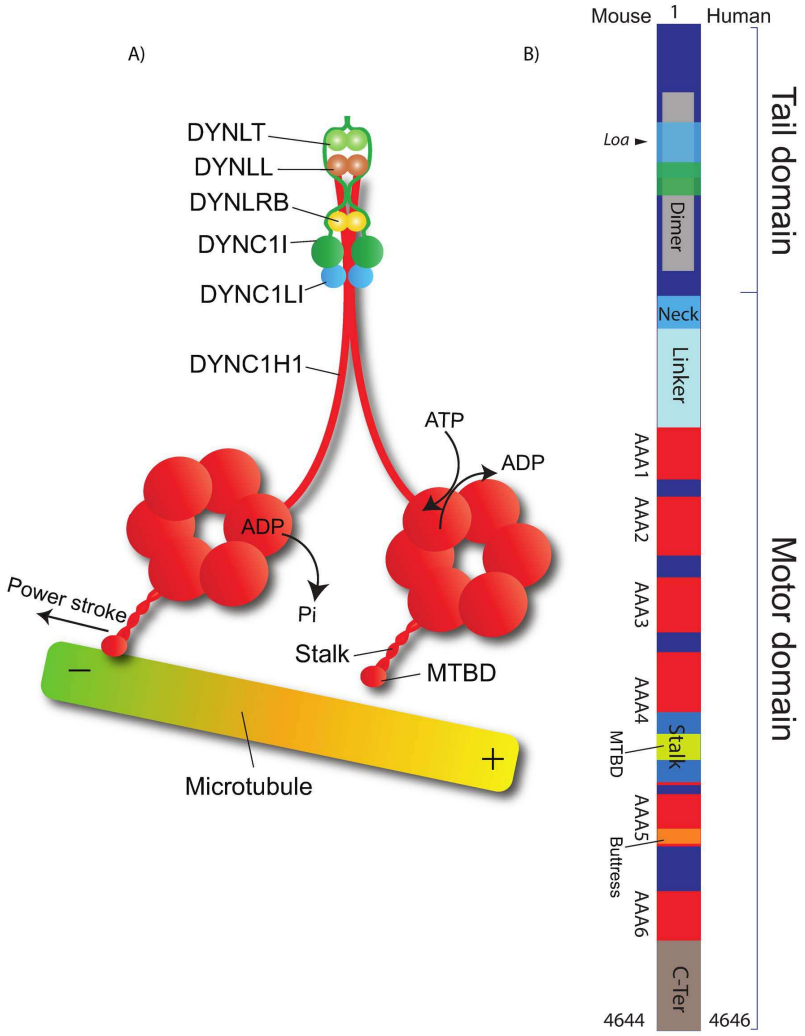

Figure 2.1: A schematic diagram of cytoplasmic dynein protein complex. A) Cytoplasmic dynein is a protein complex consisting of two homodimerized heavy chains (DYNC1H1) and associated proteins intermediate (DYNC1I), light intermediate (DYNC1LI), and light chains (DYNLRB, DYNLL, DYNLT). The C-terminal portion of the heavy chain encompasses the microtubule binding (MTBD) and motor domains. The N-terminal domain is responsible for the heavy chain homodimerization and binding of accessory proteins to the complex. B) DYNC1H1 domains and the site of the *Legs at odd angles* mutation in the mouse protein. Reproduced with permission from M. Hafezparast

formed of a large subdomain (α/β-domain) and a small subdomain (α-domain) [25, 26, 27, 43, 47]. Carter *et al.,* found the ring to be slightly asymmetric with gaps between both the AAA1-AAA2 and AAA5-AAA6 domains for a functional dimer of yeast cytoplasmic dynein from *Saccharomyces cerevisiae* in the nucleotide free state [25]. Kon *et al.,* studied a motor domain of cytoplasmic dynein with ADP from *Dictyostelium discoideum* and found that the small subdomains were arranged in 'pseudo-six-fold-symmetry' whereas the large subdomains were arranged in two groups [27]. The AAA5, AAA6 and AAA1 large domains were loosely packed together in one half of the ring, whilst the AAA2, AAA3 and AAA4 large domains were tightly packed on the other half, with no direct contact between the two halves [27]. This differs from the findings of Carter *et al.,* as these results give a gap between AAA4-AAA5, rather than AAA5-AAA6, although they do also give the AAA1-AAA2 gap [25, 27]. This may be an interspecies difference, a result of the different nucleotide states or due to differences in experimental procedures. These results suggest that the conformation of the ring depends on the ATPase state, with the gaps closing during the ATPase cycles of the domains. Indeed, Roberts *et al.,* also find a gap between the AAA1-AAA2 domains in dynein c from *Chlamydomonas reinhardtii* flagella in the absence of nucleotide and they propose that this is an 'intrinsic feature' of the AAA+ ring in this state [48]. They also find that in the primed state, i.e. ATP or ADP and vanadate (ADP.Vi) bound, where vanadate inhibits ATPase activity, trapping the ring in the primed state, the gap between the AAA1 and AAA2 domains of dynein c closes and that there is a change near the contact site of the linker to the ring at AAA4 or AAA5 [48]. Schmidt *et al.,* study the motor domain of human cytoplasmic dynein 2 in the ADP.Vi state and also find that the gap between the AAA1 and AAA2 domains is closed [49].

Of the six AAA+ domains, only four are able to bind ATP and the specific roles they play in the mechanics of dynein are still unclear [47]. Nucleotide binding sites lie between two AAA+ domains, suggested to be between one AAA module and the large domain of the adjacent module [27, 43]. Domains AAA5 and AAA6 cannot bind or hydrolyse ATP and Cho *et al.,* find that 'a single nucleotide binding site dominates the ATPase reaction', hence the four domains serve different functions during the cycle [50].

The first domain, AAA1, is the primary site for ATP hydrolysis and is essential for motility [51]. Schmidt *et al.,* find that in the nucleotide free state, the *Saccharomyces cerevisiae* AAA1 domain has a low affinity to the nucleotide and suggest that this may stop the nucleotide becoming trapped in the motor and hence stalling the ATP cycle [43]. Nicholas *et al.,* found that ADP binding at the AAA1 domain causes the head domain to exhibit stronger binding to microtubules [52], whilst DeWitt *et al.,* found that ATP binding at the AAA1 domain, as opposed to hydrolysis, causes the head domain to release from microtubules [53].

Studies have found that the AAA2 domain serves a purely structural role, with Kon *et al.,* suggesting that it can bind either ATP or ADP but cannot perform hydrolysis [27] whereas Schmidt *et al.,* find that it is 'tightly closed and appears unlikely to open' [43]. Mutations in this domain, causing an inability to bind ADP or ATP, do lead to a reduction in ATPase rates, but these changes are mild compared to mutations in the other domains and it is suggested that they may in fact only have an effect through altered communication [43, 51].

The function of the AAA3 domain has been the subject of recent study with Nicholas *et al.,* and DeWitt *et al.,* making clear progress [52, 53]. Studies of this domain have shown that its function is related to microtubule binding, with mutation studies showing an increase in the affinity to microtubules, a decrease in velocity and longer attachment times to the microtubule [50, 51]. Cho *et al.,* found that the mutant forms of dynein still exhibited processive behaviour and only gave a small reduction in run length [50]. Kon *et al.,* propose that AAA3 domain functionality is crucial for the 'ATP-induced release of dynein from microtubules' [51], whereas Schmidt *et al.,* suggest that the AAA3 domain can 'contribute to the catalytic cycle, without being essential' [43]. Nicholas *et al.,* and DeWitt *et al.,* have found that the AAA3 domain plays a significant role in microtubule release during the ATP cycle [52, 53]. Nicholas *et al.,* find that ADP binding to the AAA3 domain weakens microtubule binding and propose that ADP may only be bound 'at "appropriate" points in the cycle' [52]. DeWitt *et al.,* find that the ATP hydrolysis cycles of the AAA1 and AAA3 domains are not directly coordinated, with only 'a single hydrolysis event per step', and that the AAA3 domain 'hydrolyses ATP at an order of magnitude more slowly' than the AAA1 domain [53]. They propose that a functional AAA3 domain is required to enable communication between the AAA1 domain and the MTBD, with mutations in the AAA3 domain impeding ATP induced microtubule release [53]. They go further in their analysis proposing that the AAA3 domain acts as a 'switch' for the function of dynein required in the cell, suggesting that regulation by the AAA3 domain can switch the purpose of dynein from transport, with the AAA3 domain switched 'on', to an anchoring function, with the AAA3 domain switched 'off' [53]. Bhabha *et al.,* also propose that the AAA3 domain can serve a regulatory function, suggesting that ATP binding to the AAA3 domain 'blocks the conformational change' of the motor domain and hence allows the dynein complex to remain tightly bound to microtubules or reduces its velocity [54].

The AAA4 domain can also bind ADP but studies by Schmidt *et al.,* on nucleotide free yeast cytoplasmic dynein from *Saccharomyces cerevisiae* found that it is unlikely to be able to 'catalyse ATP hydrolysis' and its role in the ATP hydrolysis cycle is uncertain [43]. Studies by Kon *et al.,* show that mutations in this domain lead to lower ATPase rates [51], whilst Cho *et al.,* show that they cause a 'modest decrease in velocity' and a '[two]-fold increase in run length' [50]. Schmidt *et*

al., suggest that it may become activated during the hydrolysis cycle under a conformational change of the ring [43], whilst Kon *et al.,* suggest that a functional AAA4 domain may not be required but that it might 'ensure maximum stimulation of microtubule-activated ATPase activity' or that it might regulate the step size in response to force [51].

Linker

The linker unit, found to be 10nm long in flagella dynein from *Chlamydomonas reinhardtii*, is located across the front of the AAA+ ring and is connected to the tail (or stem) [55]. The linker is normally docked but can become undocked [55]. Work by Roberts *et al.,* on a functional motor domain of cytoplasmic dynein from *Dictyostelium discoideum*, suggests that in the unprimed position the linker spans the ring from the AAA1 domain to near the base of the stalk (around AAA4-AAA5) and then during the priming stroke the linker moves to a position close to the AAA2 domain [56].

Detailed crystallographic structures have built on this work. Studies by Carter *et al.,* on a functional dimer of yeast cytoplasmic dynein from *Saccharomyces cerevisiae*, in a nucleotide free state, show that the linker 'arches over the centre of the ring' with its C-terminus interacting with the AAA1 domain and the small domain of AAA6 whilst its N-terminus interacts with the AAA5 large domain [25]. Roberts *et al.,* also find that in the nucleotide free state, the linker domain of dynein c from *Chlamydomonas reinhardtii* flagella interacts with the AAA5 domain [48]. Whilst studies by Kon *et al.,* looking at the motor domain of cytoplasmic dynein from *Dictyostelium discoideum* with ADP, showed the linker lying over the hole of the ring between the AAA1 and AAA4 domains [26, 27]. The different nucleotide states of the motor domains may have a significant impact on the location of the linker domain, with a movement of the linker from AAA5 to AAA4 from the nucleotide free state to binding ADP suggested by Roberts *et al.,* [48]; although species and experimental differences may also have had an affect.

Further studies by Schmidt *et al.,* have shown that the linker is composed of four subdomains, with the first subdomain making contacts with the large domain of the AAA5 module, the second subdomain bridging the hole of the ring, and the third and fourth subdomains interacting extensively with the large domain of AAA1 [43]. Alternatively, Kon *et al.,* suggest that the linker has five subdomains and only interacts through the AAA1 and AAA6 domains, with two subdomains 'sandwiched' between the large and small domains of AAA1 and the small domain of AAA6, as well as the AAA2 domain, through two inserts [27]. Schmidt *et al.,* identify AAA2 as an alternative docking site for the linker [43].

Roberts *et al.,* find that the base of the linker does not appear to move significantly and hence suggest that the movement between states is caused by 'a rotation of the distal segment relative to the base' [48]. Schmidt *et al.,* find that there is a 'deep cleft' between the second and third subdomains of the linker which could act like a hinge [43]. Two possible models of linker movement are proposed by Roberts *et al.,* in the first they propose that the linker could be flexible at the site of the cleft however they favour a second scenario in which the linker is stiff and hinging at the cleft site requires 'energy from interactions with the AAA+ modules' [48]. Schmidt *et al.,* later find that, in the ADP.Vi state of the human cytoplasmic dynein 2 motor domain, the linker is bent by 90° between subdomains two and three (of four) [49]. They propose that the linker bend is caused by a 'steric clash' between the linker and the AAA4 domain (specifically a PS-I insert), causing subdomains one and two to bend whilst subdomains three and four remain static due to their interactions with the AAA+ ring [49].

C-sequence

The C-sequence lies on the back of the AAA+ ring across the AAA1, AAA5 and AAA6 small subdomains [25, 26, 27]. Numata *et al.,* found that the processivity of dynein homodimers was reduced after a deletion of the distal segment of the C-sequence [57], Roberts *et al.,* propose that linker undocking is preferred under a deletion of the C-sequence [56], and Kon *et al.,* suggest that it is 'crucial for communication' [27]. The structure of dynein is generally conserved across species, however yeast dynein lack the final 32kDa section of the C-terminal, also known as the CT-cap [58]. Nicholas *et al.,* found that the differences in behaviour between species, as described in Section 2.1.4 below, are likely to be caused by the presence of the CT-cap, in particular the removal of the CT-cap caused increased processivity and stall force in mammalian dynein [58].

Stalk

The AAA+ ring is responsible for the hydrolysis cycle of dynein, whereas microtubule binding is performed by a stalk structure extending from the ring and ending with a 'globular' microtubule binding domain [59]. A relatively new structure, known as a strut or buttress, has also been found as an additional coiled coil that extends from the AAA5 small domain and contacts the stalk [25, 26, 27]. The stalk extends from the AAA4 small domain as a coiled coil, with two helices denoted by CC1 and CC2 [25, 26, 27, 60, 61]. Carter *et al.,* studied the crystal structure of the MTBD and the distal portion of the stalk in a mouse cytoplasmic dynein [60]. They find that the MTBD is composed of six α helices, labelled H1 to H6, where docking to the microtubule places

H1 and H3 in 'a groove [on the microtubule] at the interface between the α and β tubulin subunits' [60]. Redwine *et al.,* suggest that the interactions between the microtubule and the MTBD are at the H1-H2 loop, H3 and H6, with intramolecular salt bridges formed by residues in H1 and H6 in a low affinity conformation which change to intermolecular salt bridges in a high affinity conformation [62].

Carter *et al.,* find that the stalk helices CC1 and CC2 connect to the MTBD α helices in the following way:

> 'The distal portion of CC2 makes extensive hydrophobic interactions with H2, H4, H5 and H6, whereas CC1 makes only a few contacts with H4 . . . before joining directly into H1. This asymmetry suggests that the interface between the stalk and the MTBD serves an important role in the dynein mechanism. ' [60].

Indeed, the possible mechanisms for modulating the microtubule binding affinity are considered extensively in the literature. Gibbons *et al.,* propose that sliding movements between the two helices of the stalk coiled coil could regulate the affinity of the MTBD [63]. Kon *et al.,* also found that by fixing the registry of the stalk coiled coil the microtubule binding affinity could be trapped into a strong or weak binding state [64]. Nishikawa *et al.,* suggest that binding to the microtubule may anchor the CC2 helix in place, which could in turn cause a registry shift in the stalk coiled coil [61]. Carter *et al.,* find a kink in the coiled coil of the stalk, caused by a pair of prolines and leading to a change in registry of CC1 compared to CC2 by a half-heptad [60]. Burgess *et al.,* also find a kink 5nm from the tip in the stalk of flagella dynein from *Chlamydomonas reinhardtii* in the nucleotide free state [55]. Imai *et al.,* describe a flexible 'hinge' within the stalk close to the MTBD and find that the stalk angles vary significantly but exhibit some dependence on the distance between the MTBDs [65].

Carter *et al.,* propose that the 'movement of CC1 is responsible for bidirectional communication along the stalk' [60]. Roberts *et al.,* find that the stalk tilts between different nucleotide states, with a shift from the nucleotide free or ADP to ADP.Vi state causing a shift of 5nm of the MTBD [56]. They hypothesize that the priming stroke of dynein causes the MTBD to 'skate along the [microtubule] surface' [56]. Kon *et al.,* also found two distinct conformations of the stalk, in one conformation it is straight and in another there is a 37° kink below the strut; they suggest that the stalk is therefore flexible and that the strut supports the stalk under load [26]. In the second conformation they also saw a change in the MTBD, and they suggest that the kinked stalk may 'modulate [microtubule] binding affinity' [26]. Schmidt *et al.,* also observed a kink in the CC2 helix

of the stalk near to the contact site of the strut, in human cytoplasmic dynein 2 in the ADP.Vi state, causing the CC2 helix to 'slip relative to CC1' [49].

Nicholas *et al.,* find that the backward force required to unbind a dynein monomer from the microtubule is much greater than in the forwards direction [52]. In particular they find that dynein exhibits slip bonding in the forwards direction, where the 'unbinding rate increases with increasing load', whereas 'slip-ideal bonding' is exhibited in the backwards direction, here the 'unbinding rate increases only up to [loads of] $\sim$ 2pN and then remains relatively constant as greater forces are applied' [52].

2.1.2 Stepping mechanism

Here we discuss the current knowledge on the mechanism dynein uses to walk along microtubules. It is of note that dynein can take steps of a variable step size and direction, as discussed below in Section 2.1.4, however it is unclear how these variations are achieved. Carter *et al.,* suggest that the angle of attachment of MTBD determines the direction of dynein's step, rather than the position of the AAA+ ring [60]. Whilst Gennerich *et al,* have found that applied force can alter dynein's stepping behaviour, discussed in more detail below in Section 2.1.4 [66]. The main features of dynein's stepping mechanism are the ATPase cycle, allosteric communication and interhead coordination.

ATPase cycle

Adenosine triphosphate (ATP) hydrolysis, where ATP is converted to adenosine diphosphate (ADP) and phosphate (Pi), is used by dynein in order to release energy to power its movement along the microtubule. This ATPase activity must be coordinated with its mechanical cycle so that dynein can walk processively along microtubules (reviewed in [67]). Although four of the AAA domains can bind ATP, it is thought that only one ATP hydrolysis event initiates a step, at the AAA1 domain, with the other AAA sites performing regulatory functions [30, 50, 53, 54]. The structural conformations of dynein are usually classified as pre- and post-power-stroke conformations, the power stroke changes dynein from the pre- to the post-power-stroke conformation, and the recovery stroke changes dynein from the post- to the pre-power-stroke conformation. Imamula *et al.,* [68] propose the following model for the ATP cycle of dynein:

- Initially dynein, in the post-power-stroke conformation and nucleotide free, is bound to the

microtubule.

- After ATP binds to the complex, it 'rapidly dissociates' from the microtubule and dynein changes to the pre-power-stoke conformation.
- ATP hydrolysis converts ATP to ADP.Pi.
- The power stoke occurs where Pi is released, dynein changes to the post-power stroke conformation and dynein binds back on to the microtubule.
- ADP is then released and the cycle starts again.

The authors suggest that in order for the recovery stroke to be successful, the dissociation from the microtubule must occur before the 'tail swing' [68]. Carter *et al.,* suggest a similar structural cycle with specific timings after ATP hydrolysis, proposing that Pi is released before dynein binds back on to the microtubule, and then the power stroke occurs once it is bound [28].

Lin *et al.,* studied dynein from sea urchin sperm flagella and found two distinct pre-power-stroke conformations, one unbound from the microtubule ('pre-I') and the other bound to the microtubule ('pre-II') with a 20° difference in orientation of the heads [29]. Previous studies have focused on the conformational change of the linker, however Lin *et al.,* found that the most significant movement was that the head pivoted around the C-terminal of the linker swinging the stalk along the microtubule [29]. Lin *et al.,* [29] propose a similar model to that described above, where ATP binding to the AAA1 domain causes the microtubule binding affinity to weaken and leads to the MTBD detaching from the microtubule, the conformational changes then occur in the following order:

- The recovery stroke causes the stalk to rotate towards the minus end of the microtubule (pre-I).
- Tilting of the stalk then allows the MTBD to bind to the microtubule (pre-II), weakly at first but then strongly once Pi is released.
- The power stroke then pulls the tail and cargo towards the minus end of the microtubule (post-power-stroke).

Note that the recovery stroke could also accompany the dissociation step [29]. A study by Burgess *et al.,* looked at flagella dynein from *Chlamydomonas reinhardtii* using electron microscopy and image processing [55] (discussed in [69]). They found that the emergence points of the tail and

stalk from the AAA+ ring were closer in the nucleotide free state compared to the ADP.Vi state, the mean angle increased from 136° to 160°, whilst the MTBD was displaced by 15nm [55].

Allosteric communication

The separation between the ATP binding site in the AAA+ ring and the microtubule binding domain at the end of the stalk means that there must be some form of communication between the two sites in order to coordinate the ATP activity with the microtubule binding activity, which is the subject of much debate in the literature (reviewed in [70]). Carter *et al.,* suggest that microtubule binding could cause a structural change in the MTBD leading to a shift in CC1 compared to CC2, which then causes a conformational change in the AAA+ ring and hence triggers part of the ATPase cycle and vice versa [60]. Kon *et al.,* found that sliding of the helices in the stalk relative to one another changes the microtubule binding affinity and the ATPase rate, providing an important link between the two activities [64].

Roberts *et al.,* suggest that the conformation of dynein in the unprimed position (post-power-stroke) has the linker domain lying across the ring between the AAA1 domain and the AAA4/AAA5 domains, whilst in the primed position (pre-power-stroke) the linker moves to the AAA2 domain [56]. In later work, they suggest that the binding of ATP to the AAA1 domain leads to conformational changes in the AAA+ ring which causes the linker to hinge thereby enabling the stalk to reach further along the microtubule, whilst the release of ADP and Pi after microtubule binding causes the linker to straighten and hence pull the complex and its associated cargo forwards [48]. Carter *et al.,* propose that ATP binding at the AAA1 domain closes the gap in the ring between the AAA1 and AAA2 domains and the change 'propagates around the ring', potentially causing the linker to detach from the AAA5 domain and a conformational change in the stalk [25]. Schmidt *et al.,* propose that the linker then attaches at the AAA2 domain and that the release of phosphate may cause the linker to move back to the AAA5 domain [43]. Interestingly, Bhabha *et al.,* find that ATP binding to the AAA1 domain can cause a conformational change in the linker, but suggest that this is only when the AAA3 domain has ADP bound and that ATP bound to the AAA3 domain prevents this change [54]. In later work, Schmidt *et al.,* propose that once the AAA1-AAA2 gap opens again, 'the bent linker reverts to its preferred straight conformation and generates force' [49]. Alternatively, Kon *et al.,* suggest that rather than changes propagating around the ring to the AAA4/AAA5 linker contact site, it is the inserts in the AAA2 domain that interact with the linker and cause it to bend, whilst they suggest that the C-terminal is also essential for communication across the ring [27]. However, Schmidt *et al.,* find that the inserts in

the AAA2 domain 'contact only the static part of the linker' and propose instead that it is a 'steric clash' with an insert in the AAA4 domain which causes the linker to bend [49]. Bhabha *et al.,* propose that the linker could also act in a regulatory capacity, suggesting that the gap between the AAA1-AAA2 domains cannot close completely until the linker has undocked from the AAA5 domain [54].

Kon *et al.,* propose that the strut (buttress) plays an important role in communication, with conformational changes in the stalk and strut, between straight and kinked profiles, coordinating the ATPase cycle and microtubule binding [26, 27]. Carter *et al.,* also suggest that the buttress may effect the conformation of the stalk and may play a part in translating changes in the AAA+ ring to the stalk [25]. In a recent study on the motor domain, Schmidt *et al.,* propose that the closure of the AAA1-AAA2 gap causes conformational changes in the ring, ultimately causing a rotation of the AAA5 small and AAA6 large domains which then moves the buttress relative to the CC1 helix of the stalk whilst the CC2 helix moves with the buttress [49].

Interhead coordination

Dynein requires both head domains in order to achieve processive movement, which suggests that interhead coordination plays an important role in dynein's stepping mechanism [71]. However, it is unclear how this occurs with possible mechanisms including AAA+ ring interactions, tension within the complex and a high duty ratio (reviewed in [28, 41, 72]). Belyy *et al.,* find that each head domain has a different stall force depending on its state, the bound head domain has a much higher stall force than an unbound head domain undergoing a search for a binding site [73]. Hence, they propose a 'load-sharing' model for the stepping of a dynein dimer, where the backward force from the cargo is balanced by the bound head alone whilst the unbound head diffuses to the next binding site, the load is then shared when both are bound; the work done to move the cargo forwards is carried out by the priming stroke of the stepping head once bound to the microtubule [73]. However, it is unclear what mechanism would enable the attached head domain to take the full load of the cargo whilst the other head is detached. Imai *et al.,* used cryo-electron microscopy to study the structure of a dynein homodimer as it moves on microtubules (using artificially dimerized dynein from *Dictyostelium discoideum* with the MTBD from human axonemal dynein 7) [65]. They found that the dynein dimer adopted a wide variety of positions, classified by two groups in which the AAA+ rings were either 'offset' or 'superposed', and propose that in the superposed conformation the two head domains interact in a front-to-back-conformation via the linker and C-terminal [65]. Nicholas *et al.,* propose that tension could regulate dynein's stepping by increasing the strength of

microtubule binding, inhibiting ATP binding or hydrolysis at the AAA1 domain, and modulating communication between the AAA1 and AAA3 domains [52]. Kon *et al.,* suggest that tension could cause the stalk to tilt and hence change the microtubule binding affinity of the MTBD [64].

2.1.3 Dynactin and dynein regulatory proteins

Regulators of cargo binding include dynactin, nuclear distribution E (NudE), NudE-like (NudEL), lissencephaly 1 (Lis1), and Bicaudal D (reviewed in [38, 39, 40, 41]; [1, 15, 74, 75, 76, 77, 78]). The presence of dynactin is essential for dynein to perform most of its diverse roles [38, 39, 79]. The structure of the dynactin complex includes an actin related protein-1 (Arp1) minifilament, which enables cargo binding to the Golgi and other membranous cargoes, and $p150^{Glued}$, which also enables cargo binding, has microtubule binding domains at the N-terminus, and can bind to dynein's intermediate chains [38, 39, 40, 41, 79]. The presence of dynactin has been found to increase dynein processivity [78, 79, 80], with disruptions to dynein-dynactin interactions causing a reduction in processivity [81]. Ross *et al.,* found that the motion of the dynein-dynactin complex was bidirectional [82], whilst Kardon *et al.,* found that the addition of dynactin did not affect the direction of movement [80]. King and Schroer suggest that dynactin may act as a 'tether' to the microtubule, stopping the cargo diffusing away so that dynein can easily rebind to the microtubule if it becomes dissociated [79]. However, Kardon *et al.,* find that in yeast, dynactin increases dynein processivity independently of dynactin's microtubule binding activity [80]. Dynactin also helps to target dynein to the plus ends of microtubules [38].

2.1.4 Stepping patterns

Dynein moves processively towards the minus end of microtubules [83]. Reck-Peterson *et al.,* have shown that two motor domains are required for processive motion, however only part of the heavy chain is required with an artificially dimerized truncated form named GST-$Dyn1_{314kDa}$ suggested to be the minimal form which gives processive motion [30]. Processivity may only require one functional motor domain as DeWitt *et al.,* have shown that a complex with one wild-type motor domain and one mutant motor domain, which lacks the ability to hydrolyse ATP at the AAA1 domain, is able to walk processively along microtubules [31]. Typical run lengths for cytoplasmic dynein vary by species, with bovine dynein having an average run length of 700nm compared to 300nm for murine dynein, which increases to 1.5μm and 800nm respectively in the presence of dynactin [84]. *In vivo* measurements have shown that most species of dynein are capable of high velocities, with ranges given from 500nm s^{-1} to 1.5μm s^{-1} [83, 84]. However, dynein in mammalian

neurons can reach speeds of 2 to 3μm s^{-1} [84] and yeast dynein species move much slower with Reck-Peterson *et al.,* recording velocities averaging 90nm s^{-1} *in vitro* [30].

Step sizes

The stepping of dynein has been shown to be highly variable compared to other motor proteins. Although the predominant direction of travel along microtubules is towards the minus end, hereafter described as the forwards direction, dynein can also take backward steps [66, 31, 32, 30, 83]. Reck-Peterson *et al.,* studied GST truncated yeast cytoplasmic dynein from *Saccharomyces cerevisiae* and found that when labelled at the tail domain 20% of steps moved backwards, compared to 13% of steps when labelled at the AAA+ ring [30]. Qiu *et al.,* and DeWitt *et al.,* also studied yeast cytoplasmic dynein and found that 23% and 20% of steps moved backwards respectively [31, 32]. The step size of dynein is highly variable with most studies finding the predominant step size of the tail domain to be 8nm with larger steps of 12 to 24nm present [32, 30, 66, 83, 85], although DeWitt *et al.,* find the distribution of step sizes to peak at 4.8nm and 8.7nm [31]. When labelled at the motor domain, the predominant step size is found to be 16nm by Reck-Peterson *et al.,* although Qiu *et al.,* find it to be slightly smaller and DeWitt *et al.,* find it to be slightly larger at 17.5nm as well as suggesting another peak at 9.3nm [30, 31, 32]. Backward steps were found to be predominantly 8 to 16nm [30, 66, 83]. The steps of dynein are not one-dimensional and have been shown to have an off-axis component, i.e. can step sideways as well as along the microtubule [30, 32]. Reck-Peterson *et al.,* find that 18% of motor domain labelled steps had an off-axis component which ranged in size from 4 to 40nm [30]. Qiu *et al.,* find the two-dimensional step size of dynein to be 10nm when labelled at the tail domain and between 14 to 16nm when labelled at the motor domain [32].

The variability of dynein's stepping behaviour has raised the question of how this benefits the motor in order for it to accomplish its cellular tasks. Mallik *et al.,* looked at bovine cytoplasmic dynein and found step sizes of predominately 8nm under high load, which then increased to 24 to 32nm under close to zero loads [85]. They suggest that dynein could act like a 'gear' by reducing its step size in order to increase the productive force to move larger loads [85]. However, Toba *et al.,* studied porcine cytoplasmic dynein and found that the step size was independent of both the applied force and ATP concentration (for forces in the range of 0 to 7pN and ATP concentrations in the range of 10μM to 1mM) [83]. It is unclear whether these contrasting results are caused by experimental differences [83, 84]. Studies by Gennerich *et al.,* on artificially dimerized yeast cytoplasmic dynein find that the applied force affects the distribution of step sizes with higher

loads, in the range of 6 to 10pN, increasing the prevalence of steps of 4nm and intermediate loads (3 to 6pN) increasing the prevalence of large steps of 12 to 20nm [66].

Stepping patterns

How the two motor domains coordinate their stepping in order to achieve high velocities and long run lengths has been a topic of interest and developments in experimental techniques have enabled the two motor domains to be labelled individually in order to compare their stepping trajectories. Studies by Qiu *et al.,* and DeWitt *et al.,* who both looked at artificially dimerized yeast cytoplasmic dynein from *Saccharomyces cerevisiae*, found that dynein exhibits a predominantly alternating stepping pattern, with Qiu *et al.,* finding that 74% of steps alternated in time compared to 68% in experiments by DeWitt *et al.,* [31, 32]. Qiu *et al.,* also found that 83% of steps did not pass the stationary motor domain [32]. Both studies found distinct characteristics between the leading and lagging heads, with the leading head more likely to be on the right, when looking along the direction of motion [31, 32]. DeWitt *et al.,* found that the leading head took much shorter steps of 1.5nm and was more likely to step backwards (45% of steps); where as, the lagging head took larger forward steps of 17.5nm but was less likely to step backwards (14% of steps) [31]. Qiu *et al.,* found that the lagging head is likely to spend less time attached to the microtubule, with the mean time a lagging head spends attached to the microtubule when both heads are bound at 4.3s compared to 5.4s for the leading head [32]. The mean duration that both heads were bound to the microtubule decreased as the separation distance between the two motor domains increased [32]. Both DeWitt *et al.,* and Qiu *et al.,* propose that the two motor domains walk along different protofilaments of the microtubule, with DeWitt *et al.,* suggesting that a stacking interaction between the two AAA+ rings is excluded by the large distance separating the heads (23nm) [31, 32]. Qiu *et al.,* and DeWitt *et al.,* also find that when the motor domains are in close proximity, along the length of the microtubule, then they both have an equal probability of stepping, but that the lagging head is increasingly likely to step as the separation distance between them is increased [32]. Qiu *et al.,* propose that dynein can use both stochastic and tension-based stepping, with stochastic stepping used when the two motor domains are close together and moving to tension based stepping as they separate over larger distances [32]. DeWitt *et al.,* also suggest that the tension within the complex may cause the lagging head to detach when the two motor domains are separated over larger distances [31].

Dwell times

The dwell time is defined as the period of time before the step that the complex, if labelled at the tail, or motor domain, if labelled at the AAA+ ring, takes. Reck-Peterson *et al.,* analysed the dwell times of tail labelled GST truncated yeast cytoplasmic dynein from *Saccharomyces cerevisiae* and found that they fit to a single exponential distribution with an average dwell time of 2s [30]. They suggest that this relates to a single ATP binding event per step of the tail [30]. They also found that the dwell times of the motor domains were best fit to a distribution of a convolution of two exponentials and suggest that each motor domain steps only once for every two ATP cycles of the entire complex [30]. DeWitt *et al.,* also find that the motor domain dwell times are best fit to a convolution of two exponentials, with one slow and one fast rate, however they also fit the tail dwell times to a convolution of two exponentials with two unequal rate constants [31]. Toba *et al.,* find that dwell times for tail labelled porcine dynein under load (3 to 5pN) fit a single exponential distribution with mean 27ms, while the average dwell time in the absence of load is 10ms [83].

Force

In vivo dynein will be subjected to load, such as that from vesicles it is transporting, or force, for example from a tug-of-war with positively directed motors. The response to load or force can be studied in experiments by the use of an optical trap. Mallik *et al.,* find that the stall force of bovine cytoplasmic dynein is 1.1pN at saturating levels of ATP [85], and similar stall forces have been found for both rat and murine dynein [35, 84]; whilst Toba *et al.,* [83] find the stall force for porcine cytoplasmic dynein to be 7pN, independent of ATP concentration.

Gennerich *et al.,* initially studied native yeast cytoplasmic dynein attached to a 1μm bead and bound to sea urchin axonemes and found the stall force to be 7pN independent of the ATP concentration [66]. An interesting finding of their study was that dynein was shown to walk in the absence of ATP, with a 10pN force (opposing the minus end directed motion of dynein) causing dynein to move processively towards the plus end and a -3pN force causing minus end directed motion [66]. Their results showed clear stepping along the microtubule with a predominant step size of 8nm [66]. They also investigated stepping in the presence of ATP (1mM), a small rearward load (1pN) led to mainly minus end direction motion with 30% of steps in the backwards direction, a higher load of 7pN caused approximately equal numbers of forward and backward steps, whilst a load of 10pN saw predominantly backward stepping, with only 25% of steps in the forwards direction [66]. They propose that the stepping behaviour can be split into two types, an 'advancing mode ' and a 'non-advancing mode' [66]. The advancing mode is defined by two or more successive

steps in one direction and dominates at low forces with mainly small step sizes of around 4 to 8nm [66]. Whereas the non-advancing mode is defined as two or more successive forward then backward steps usually of the same large step size and becomes more prevalent as the load increases [66]. Gennerich *et al.,* propose that the forward step in the non-advancing mode is driven by ATP whereas the backward step is caused by the leading head detaching from the microtubule and rebinding to a rearward site [66]. They suggest that the strength of the binding affinity of the MTBD to the microtubule is dependent on the angle of the stalk and that the asymmetry in the applied force required for movement biases the motor to be directed towards the minus end of microtubules [66].

2.1.5 Mutations

Mouse models have been used to study the effects of mutations in the dynein heavy chain including the *Legs at odd angles* (*Loa*), *Cramping 1* (*Cra1*) and *Sprawling* (*Swl*) mutants. The *Loa* mutation occurs in the tail domain at a site identified as the binding site for dynein intermediate chains and also the proposed site of homodimerization [3]. Hafezparast *et al.,* find that the percentage of high speed carriers falls from 67% in wild-type neurons to 21% in *Loa/Loa* mutants and that there was an increase in pauses in mutants [3]. Garrett *et al.,* tracked endosomes in *Loa/Loa* mutant mouse embryonic fibroblasts (MEFs) and neurons, finding lower numbers of high speed carriers and an increase in plus-end directed motion [2]. Endosomes in *Loa/Loa* mutant MEFs travelled with a median speed of 0.11μm s^{-1} compared to 0.17μm s^{-1} for wild type cells and after ten minutes *Loa/Loa* mutant endosome displacement was only 4.4μm compared to 13.4μm for wild type cells [2]. Ori-McKenney *et al.,* also study the *Loa* mutation and found that the average run length *in vitro* fell from 339nm for wild type dynein to 259nm in *Loa +/-* mutants and to 175nm in *Loa -/-* mutants [35]. Interestingly, they found no difference in average velocity or step size and little change in stall force *in vitro* [35]. However, they do find reduced average velocity *in vivo* for lysosome transport in neurons with velocity falling by 22% and 43% for *Loa +/-* and *Loa -/-* respectively compared to wild type velocity [35]. They suggest that this is a result of an increase in run terminations and find no change in the instantaneous velocity [35]. They also find a reduction in run length *in vivo* by 53% and 83% for *Loa +/-* and *Loa -/-* respectively compared to wild type [35]. Both studies by Garrett *et al.,* and Ori-McKenney *et al.,* found an increase in the number of off axis steps for *Loa* mutants [2, 35]. Ori-McKenney *et al.,* additionally found a reduced affinity for microtubules in the *Loa +/-* mutant in the presence of ATP and a decreased Michaelis constant for ATP which they suggest is a result of early binding of ATP to an attached motor domain (i.e. whilst the other is detached) through a problem with communication between the head domains

[35]. Sivagurunathan *et al.,* study the *Loa* mutation in *Neurospora crassa*, also finding a decrease in minus-end directed velocity and run length [36].

Deng *et al.,* find that there are fewer interactions with the p150^{Glued} subunit of dynactin for *Loa/Loa* mutants in mice and that there is an increase in the binding affinity of the dynein intermediate chains, dynein light intermediate chains and Tctex-1 [37]. They find that the homodimerization of the dynein complex is not affected and instead suggest that the mutation causes a reduction in dynein-dynactin complexes available for cargo transport and hence reduces endosome velocity [37]. Whilst Sivagurunathan *et al.,* found that dynactin still co-localized with a *Loa* mutant dynein in *Neurospora crassa* and suggest that the *Loa* mutation could cause a problem with interhead coordination between the two motor domains [36].

The *Cra1* mutation lies in the proposed homodimerization site of the dynein heavy chain and presents with a similar phenotype to the *Loa* mutant [3]. Chen *et al.,* study the *Swl* mutation which also presents a similar phenotype to the *Loa* mutation and occurs in the dynein heavy chain in the cargo binding region and also in the proposed site of homodimerization [86]. They suggest that this mutation is connected to hereditary sensory neuropathy or some forms of Charcot-Marie-Tooth disease [86].

Mutations in the dynein heavy chain 1 (DYNC1H1) have been identified in humans with Charcot-Marie-Tooth disease type 2 (CMT2), spinal muscular atrophy with lower extremity predominance (SMA-LED) and intellectual disability [5, 34] (reviewed in [4]). Weedon *et al.,* find a DYNC1H1 mutation in three individuals with CMT2 which occurred in the proposed homodimerization domain [34]. Scoto *et al.,* suggest that the mutations that they identify in humans with SMA-LED, occurring in the tail and motor domain of DYNC1H1, have a similar effect to the *Loa* mutation and cause SMA-LED with malformation of cortical development [5]. Fiorillo *et al.,* present two mutations in DYNC1H1, one occurring in the neck and the other in the motor domain, which result in a phenotype of 'congenital motor neuron disease associated with focal areas of cortical malformation' [87]. Schiavo *et al.,* report that genetic background may be significant in the resulting phenotype from a specific mutation in the DYNC1H1 [4]. Banks *et al.,* study a mutation in the light intermediate chain of dynein and find that the mutant mice have altered neural development and suffer from increased anxiety [88].

The interactions of dynein with its regulators are also important, with mutations in Lis1 causing severe neuronal migration defects [89]. Whilst mutations in $p150^{Glued}$ of dynactin have been found in patients with amyotrophic lateral sclerosis (ALS) and distal spinal and bulbar muscular atrophy (SBMA), as well as being linked to Perry syndrome [90].

2.2 Relevant models

Endocytosis and intracellular transport has been a significant topic of interest for modelling as well as the motion and distribution of kinesin motors, however in comparison relatively few authors have studied dynein and its processes. Lan and Sun model myosin monomers, dimers and collective assemblies of motors by studying the 'energy landscape', which can be reduced to ratchet, power stroke or Markov models depending on the assumptions made; their work can also be applied to other motor proteins [91]. Relevant models are discussed below.

2.2.1 Intracellular transport

Intracellular transport is a wide field of study, for example Rubinow and Blum model general transport in axons [92], I. A. Kuznetsov and A. V. Kuznetsov model the transport of short microtubules in an axon [93], and Gou *et al.,* model the transport of early endosomes in fungal hyphae [94]. Of particular interest is the model by Smith and Simmons [95] on bi-directional transport by motor proteins, described in detail below, which has been extended and studied by several other authors [96, 97, 98, 99, 100, 101]. Gou *et al.,* model dynein population densities studying various mechanisms for the transition between dynein walking along microtubules to being carried by kinesin-3 in the opposite direction [94].

Lipowsky *et al.,* have studied lattice models for motor proteins using an asymmetric simple exclusion process (ASEP), with a specific focus on kinesin motors, modelling the microtubule as a one-dimensional line within a three-dimensional lattice [102, 103, 104, 105]. They model motor motion as a random walk, either stepping on the microtubule or unbinding and diffusing, in both open and closed domains [102, 103, 104, 105]. Klumpp and Lipowsky extend this work to patterns of filaments with opposite polarities, from two parallel filaments to square lattices with intersecting filaments [106]. In another paper by Klumpp *et al.,* they study multiple microtubules arranged in either parallel or radial arrangements with the same polarity [107]. Chai *et al.,* consider stepping, binding and unbinding defects within the model [108]. In their later work, Chai *et al.,* model the population dynamics of multiple types of motor proteins together in a domain, where the microtubule continues to be modelled as a one dimensional lattice, motors perform random walks biased towards a certain direction depending on the species and are considered as part of a reservoir when unbound [109].

Ashwin *et al.,* [110] study the population dynamics of dynein on tracks also using an asymmetric simple exclusion process, described in detail below, the model is extended in later papers by the

group [111, 112] and a general model is analysed by Juhász [113, 114]. Ebbinghaus and Santen study a two lane lattice model for intracellular transport, using one lane to model transport on the microtubule and the other for diffusion in the cytoplasm [115]. In later work Ebbinghaus *et al.,* extend this model to include a dynamic track where binding sites can be eliminated [116]

Many authors have also considered multiple-motor transport, by motors of either the same or different types. Klumpp and Lipowsky consider a cargo pulled by N motors of the same type which can bind to and from the microtubule or filament modelling this as a continuous-time Markov process [117]. This model is extended to study a tug-of-war between two types of motor proteins acting on a cargo [118, 119, 120]. Berger *et al.,* study the elastic coupling between two motor proteins [121, 122, 123]. Kunwar *et al.,* model multiple-motor transport by kinesin motors, modelling the kinesin motors as springs and the attachment to and from the microtubule stochastically [124]. Korn *et al.,* also study transport by multiple kinesin motors using a Langevin equation to model the dynamics of the cargo, modelling the kinesin motors as either a harmonic spring or a cable, and microtubule binding is modelled stochastically [125]. Driver *et al.,* look at the behaviour of two kinesin-1 motors, with each motor modelled as a linear spring and connected together by a rigid rod whilst using a kinetic model for stepping [126].

Reaction diffusion transport model

Smith and Simmons model the bi-directional motion of organelles and vesicles, referred to as particles, along microtubules both when attached and when diffusing freely [95]. Focusing on transport in axons and dendrites, they consider one spatial dimension and make the following assumptions:

1. "a 'particle ' consists of a complex between an organelle or vesicle and motor proteins (permanently attached to the surface membrane);
2. particles either diffuse freely in solution or move on a filament at a steady velocity v (the 'motor velocity '), which may depend on the number of motors on the particle;
3. binding to and detachment from filaments are kinetic processes specified by first-order rate constants, which include factors as appropriate for lateral diffusion and the density of motor proteins and filaments; and
4. in the general case of bidirectional transport, binding is followed by motion in either direction, as a result of the presence of filaments and/or motors with both polarities. " [95]

For simplicity they further assume that the filaments solely determine the direction of travel [95]. The following reaction-diffusion-transport equations are thus derived:

$$\frac{\partial n_0(x,t)}{\partial t} - D\frac{\partial^2 n_0(x,t)}{\partial x^2} = -(k_+ + k_-)n_0 + k'_+ n_+ + k'_- n_-, \tag{2.1}$$

$$\frac{\partial n_\pm(x,t)}{\partial t} + v_\pm \frac{\partial n_\pm(x,t)}{\partial x} = k_\pm n_0 - k'_\pm n_\pm, \tag{2.2}$$

where $n_0(x,t)$ is the density of free particles and $n_\pm(x,t)$ are the densities on the outward $(+)$ and inward $(-)$ filaments, at time t and position x [95]. The parameters $v_+ > 0$ and $v_- < 0$ are the motor velocities, k_+ and k_- are the rate constants for binding to filaments, k'_+ and k'_- are the rate constants for detachment, all on outward and inward filaments respectively; and D is the diffusion constant for free particles [95].

This model is helpful in understanding the macroscopic behaviour of endosomes, however we are concerned with the particular mechanisms of cytoplasmic dynein which cannot be studied using this model. A drawback with this model is the use of constant velocity, where experiments have shown oscillatory velocity profiles [2]. The presence of free diffusion in the model is questionable due to the crowded nature of the cytoplasm. The high speeds seen in experiments for axonal transport would also suggest that there is little diffusion, and the transport is solely through the action of motor proteins. The large numbers of different motor proteins acting on an endosome at any one time would also limit the possibility for free diffusion. The pauses and changes in direction of organelles may instead be caused by the interactions of multiple motor proteins, such as the effects caused by a tug-of-war.

Asymmetric simple exclusion process model

Ashwin *et al.,* propose a bi-directional transport model for the population dynamics of dynein on a single microtubule where either dynein moves by itself to the minus end or is carried by kinesin to the plus end [110]. They make the following assumptions:

- "All the motors are of one of two types - moving either to the right or to the left.
- Right and left moving motors pass without interaction, but there is an 'exclusion principle' that means a motor can only move forwards if the site ahead is free of motors of the same type.
- In the dilute state, the motors move at a mean velocity v_+ and v_- to the right/left, respectively.

- There is a random switching of direction where right-moving motors change to left-moving at a rate p_d, and left-moving motors change to right-moving at a rate p_u, where $p_{d,u}$ can be expressed by velocities and $M_{a,r}$, the mean free run length of left (right) moving motors before turning as $p_d = v_+/M_a$ ($p_u = v_-/M_r$)." [110]
- "The right boundary of the MT has no-flux boundary conditions.
- The right-moving motors appear at the left boundary with flux rate $\alpha_+ = F_{in}$ while the left-moving motors exit without impediment.
- The system is in statistical equilibrium." [110]

The microtubule is discretized into two tracks, a mean field approximation and further simplifications are used in order to obtain the following system of partial differential equations:

$$\frac{\partial \rho}{\partial t} = -p_d\rho(1-\sigma) + p_u\sigma(1-\rho) + \frac{v_+}{L}(2\rho - 1)\frac{\partial \rho}{\partial x} + \delta\frac{v_+}{2L}\frac{\partial^2 \rho}{\partial x^2}, \tag{2.3}$$

$$\frac{\partial \sigma}{\partial t} = p_d\rho(1-\sigma) - p_u\sigma(1-\rho) + \frac{v_-}{L}(1 - 2\sigma)\frac{\partial \sigma}{\partial x} + \delta\frac{v_-}{2L}\frac{\partial^2 \sigma}{\partial x^2}, \tag{2.4}$$

where ρ and σ represent the densities for the right and left tracks respectively, t is the time variable, v_+ and v_- are the mean velocities of the right and left motors respectively, and $\delta = \frac{h}{L}$ where h is the spatial step and L is the spatial length of the simulation [110]. In this paper they focus on the effects of queueing, assuming that there is zero flux at the plus end of the microtubule and studying the accumulation of motors at this end [110]. The model produces results similar to experimental observations [111]. They extend this model in later work to include thirteen tracks, in order to reflect the thirteen protofilaments comprising a microtubule, and allowing some loss of dynein at the plus end of the microtubule to account for detachment [111]. They continue to use a fixed step size of 8nm [111], which does not reflect the variability in step size or the step size of the MTBD which is primarily 16nm [30]. The possibility of dynein side stepping to a different protofilament is included however they do not include backward steps taken by dynein [111]. In later work, the original model is extended to study the transportation of early endosomes via two microtubules arranged in an antipolar bundle (i.e. two parallel microtubules with one orientated from minus to plus end and the other orientated from plus to minus end, which overlap for a portion of their minus ends allowing motors to switch between the two microtubules in this section) [112].

The mathematical framework provides a significant contribution to the understanding of the behaviour of dynein populations on microtubule tips as well as the transportation of early endosomes, however the mechanism employed by individual dynein motors is not considered. We wish to consider a more detailed model of the involvement of dynein within the transport process,

concentrating on the mechanics of a single dynein rather than the population in order to fully understand how mutation will effect the transport process.

2.2.2 Kinesin

Several authors have studied the stepping and processes of kinesin from various different approaches. Liepelt and Lipowsky study the chemomechanical cycle of kinesin using a six and seven state model describing the motor dynamics as a continuous-time Markov process, this model is extended in later work [127, 128, 129, 130, 131]. Keller *et al.,* extend this model to consider the transport of a cargo by kinesin-1 motor proteins [132]. Munárriz *et al.,* model the stepping of kinesin using a simple flashing ratchet model [133]. Bier proposes that motor proteins can be modelled as a Brownian ratchet [134], extending this simple model to the stepping of kinesin for which the stepping cycle is categorised by two distinct phases: a 'power stroke phase' and a 'ratcheted diffusion phase' [135, 136]. In later work Bier suggests that the 'flashing ratchet' model best describes kinesin monomers whilst a 'feedback control ratchet' is more appropriate to describe kinesin dimers [137]. Bier later considers backward stepping of kinesin, assuming that a backward step is caused by the rearward head re-binding to the same binding site [138]; whilst Bier and Cao propose that these backward steps can actually maximise the speed of kinesin [139]. Zhang builds on earlier work by Bier including an additional phase to categorise ATP binding in order to account for ATP dependence [140]. In other work, Zhang studies the mechanochemical cycle of kinesin obtaining an expression for the mean velocity [141]. Fisher and Kolomeisky propose a mechanochemical model for kinesin that describes the transitions between the chemical states [142, 143]. In work by Zhang and Fisher, they study the proposed 'limping' of kinesin [144]. Imafuku *et al.,* model the 'hopping' of kinesin, which occurs when the attached head becomes detached from the microtubule due to external load before reattachment at an alternative binding site [145]. Hendricks *et al.,* look at the components of the kinesin complex in more detail, deriving a mechanistic model to describe the stepping process, as discussed below [146].

Lisowski *et al.,* consider a model in which kinesin serves purely as a 'tether' to keep the cargo attached to the microtubule whilst it undergoes diffusion [147]. In other work, Lisowski *et al.,* develop a model for a general two head motor using overdamped Langevin equations where the motor is subjected to Lévy white noise, the two heads are connected by a harmonic spring, experience repulsion when they are too close to each other and their interaction with the microtubule (or track) is modelled using a ratchet potential which is anisotropic and periodic [148]. Jamali *et al.,* model kinesin stepping using a stochastic model with Gaussian white noise, including potentials

representing the elastic interaction between the two heads of the dimer, repulsion between head domains from other kinesins, and a ratchet potential for the interaction with the microtubule [149].

Mechanistic model for kinesin

Hendricks *et al.,* derive a mechanistic model to describe the transient dynamics of kinesin [146]. They study the motion of the individual components of kinesin (the strongly bound head, weakly bound head, neck and linker) attached to a bead [146]. In the model the two head domains connect to a neck via a spring, and the neck is also connected to the cargo by a spring [146]. The motion of the bead, strongly bound head and neck are then described by the following system of first order differential equations:

$$\gamma_b \dot{x_b} = -F_L + K_b(x_n - x_b), \tag{2.5}$$

$$\gamma_s \dot{x_s} = K_s(u - x_s) + K_h(\Psi_s - \psi_s), \tag{2.6}$$

$$\gamma_n \dot{x_n} = -K_b(x_n - x_b) - K_h(\Psi_s - \psi_s) - K_h(\Psi_w - \psi_w), \tag{2.7}$$

where x is the position, with the subscripts b, s, n and w referring to the bead, strongly bound head, neck and weakly bound head respectively, $\psi_s = x_s - x_n$, and $\psi_w = x_w - x_n$ [146]. The model parameters are as follows: γ is the viscous damping coefficient, F_L is the external load acting on the bead, spring constants K_b and K_h for the springs connecting the bead to the neck and the neck to the head respectively, the equilibrium positions Ψ_s and Ψ_w of the neck with respect to the strongly and weakly bound heads respectively, spring constant K_s representing the affinity to the microtubule in the strongly bound state, and u the binding site [146]. The motion of the weakly bound head, which is assumed to be the rearward head, is modelled separately [146]. It is assumed that the weakly bound head is propelled forward by the elastic forces acting on it and that it moves to the next available binding site through Brownian motion. This diffusion process is modelled using the mean first-passage time based on past and future potentials for the microtubule binding affinity and the internal stresses of the complex [146]. Once the weakly bound head binds to a binding site, the two heads switch states, so that the strongly bound head now becomes the weakly bound head and vice versa [146]. This switching is modelled by a single variable, assuming inter-head coordination, using Michaelis-Menton kinetics [146]. The model agrees well with experimental results for the behaviour of kinesin velocity under varying load and ATP concentrations, however it is limited as it does not include backward stepping and can not be used to study mean run length due to the use of a single variable to describe the chemical state.

2.2.3 Dynein

The stepping process of kinesin has been much more widely studied than that of dynein, studies of dynein have generally focused on the mechanochemical cycle. Singh *et al.,* use Monte Carlo simulations in order to model dynein, they assume that dynein has a single head and that the step size is determined by the chemical state of the secondary ATP binding sites [150]. These are significant assumptions as interhead coordination plays an important role in dynein stepping and there is little evidence that suggests that the step size is governed by the secondary binding sites. Mukherji proposes a model for dynein based on its chemical transition rates and studies the probabilities of the molecule being at certain points on a lattice in a certain chemical state, however their model is fairly simplistic as in particular they treat dynein as a single head hence neglecting interhead coordination [151]. Tsygankov *et al.,* also consider the mechanochemical cycle but here they look at a two-headed complex, discussed in more detail below [152]. They couple this model to Langevin equations in order to model the structural conformation of the complex, again this is discussed in more detail below [153]. Šarlah and Vilfan also study the structural conformation of the molecule and use a kinetic model of the ATP cycle to study the stepping patterns, see below for more detail [154]. Zheng uses an elastic network model to study the conformations and transitions between the pre-power-stroke and post-power-stroke states of a single dynein motor domain [155].

Chemomechanical model for dynein

Tsygankov *et al.,* study the coordinated stepping of cytoplasmic dynein by modelling its chemomechanical cycle [152, 153]. In their first model, they initially consider stepping in the absence of ATP induced by applied force, studying the association and dissociation rates of the two head domains using the Arrhenius Equation:

$$k = A\exp(\frac{-E_a}{k_B T}), \tag{2.8}$$

where k is the rate constant, A a prefactor known from experiments, E_a the activation energy, k_B the Boltzmann constant and T absolute temperature [152]. The prefactors are taken to be the association and disassociation rates in the absence of force from experimental data; and the activation energy is taken to be $D_i F$ for $i = 1, 2, 3, 4$ where $D_1 - D_2 + D_3 - D_4 = \Delta x$, given Δx as the step size of the motor, and F is the horizontal force applied to the motor [152]. They proceed to derive expressions for the mean run time, run length and velocity, and analysis of these results shows that as the force increases the mean velocity also increases however the mean run

time decreases illustrating a 'trade-off' between high processivity and high velocity [152]. This raises the question of whether this trade off is species specific, as different species exhibit different velocities and run lengths, as well as how the presence of dynactin might effect this trade off given its positive impact on run length. Tsygankov *et al.,* introduce ATP hydrolysis into their model by considering both a four and six state cycle, and within their analysis they propose a set of minimal chemomechanical cycles of two distinct types: one head at a time and out of phase motion [152]. The authors propose that coordination between the two motor domains in the ATP hydrolysis cycle is required to achieve the high velocity and run length seen in experiments [152].

In later work Tsygankov *et al.,* studied conformations of the dynein homodimer, moving between pre-power-stroke and post-power-stroke states whilst the forward MTBD remains fixed to the microtubule [153]. They develop a stochastic model using Langevin equations to model the dynamics of the angles determining the conformation of the motor; representing the curvature of the tail and stalk, the angle between the positions that the tail and stalk exit the AAA+ ring, the angle of MTBD attachment and the angle describing the relative orientation of the two head domains [153]. Their results show that the stepping MTBD is constrained to motion in one dimension along the microtubule and to a position close to the binding site 8.2nm away from the bound MTBD [153]. Tsygankov *et al.,* combine this structural model with their previous chemomechanical model as described above, the results show processive motion with both forward and backward steps, although they do not achieve the range of step sizes seen experimentally [153]. The authors suggest that interhead coordination may occur between the two AAA+ rings at a site which is located in the same region as the C-sequence domain when the rings are in close proximity [153]. They also suggest that both the power stroke and recovery stroke are needed in order to move the MTBD to the next binding site [153].

This work provides significant insight into the stepping process of dynein. However, alternative models may be of more interest when studying how tension and force affect the complex. For example, the effects of force are only studied through dissociation and association rates within this model [153]. Alternative approaches to modelling may also be of more interest when studying mutations which occur outside of the motor domain if their mechanistic effects do not directly impact on the chemical cycle or conformation of the motor domain.

Winch model for dynein

Šarlah and Vilfan also propose a mechanochemical model for cytoplasmic dynein combining an elastomechanical with a kinetic approach under the assumption that dynein behaves like a winch,

with its MTBD moving forward to the next binding site and then pulling the cargo forwards [154]. They model the AAA+ ring as a rigid disc, the linker as a rigid rod which can take two conformations, the stalk is modelled as an ideal elastic rod, and the dimerized tails are modelled as an elastic cord [154]. The two AAA+ rings are assumed to interact with this interaction modelled by: 'hard-core repulsion between two cylinders and an additional attractive interaction that [favours] parallel stacking of the two rings'. They then compute the conformations of the dynein homodimer with minimal energy using Monte Carlo methods, assuming that the molecule prefers to be in a front-to-back conformation of the AAA+ rings [154]. A kinetic model for the ATP hydrolysis cycle is then used in order to model the stepping of the dimer [154]. Their results reflect experimental observations on the effects of applied force, however the step size distributions do not exhibit the larger step sizes seen in experiments or the proportion of off axis stepping [154]. They do find comparable levels of alternating stepping when modelling loosely coupled dimers but their model still gives a predominately hand-over-hand stepping pattern rather than the shuffling seen for this complex, this may be due to the existence of ring-to-ring interactions still present in the loosely coupled model which may weaken or disappear if the two head domains are located far enough apart as suggested in some experiments [154].

We therefore set out to derive a mechanistic model from first principles to describe the stepping behaviour of cytoplasmic dynein 1. We wish to consider a general integrative model for dynein attached to a cargo, which could be applied to an individual species by the choice of parameters and considers the motion of the various structural components such as the MTBDs and AAA+ rings separately. Research outcomes for the study are to develop a mathematical model that corroborates and investigates current experimental observations, to make predictions that are experimentally testable and to study the mechanistic effects of mutations on dynein function.

Part I

Continuous Model

Chapter 3

Derivation of the Mechanical Model

We propose a general integrative mechanical model for the motion of a single dynein, attached to a cargo, walking along a single microtubule [9]. The cargo modelled represents various cellular objects such as a vesicle or endosome *in vivo* or a bead *in vitro*, and any regulators of cargo binding, such as dynactin, are modelled as part of the cargo. We model the cargo, AAA+ rings, and MTBDs as spheres with small Reynolds numbers, as shown in Figure 3.1 [9]. The stalks and associated strut or buttress are modelled as springs. The tail section of dynein is modelled as two springs each connecting an AAA+ ring to the cargo. The fixed part of the linker domain is assumed to be modelled as part of the sphere representing the AAA+ ring and the rest of the linker domain is modelled as part of the tail spring. The microtubule is modelled as a one-dimensional line with positive direction towards the nucleus (and therefore negative direction towards the membrane, the inverse of usual signs). We will only consider movement along this microtubule, leaving detachment and switching between microtubules for later studies. For simplicity we will only consider one space dimension, looking at forces and movement in the horizontal direction, leaving higher dimensions to future studies. Let $x_C(t)$, $x_A(t)$, $x_B(t)$, $x_D(t)$ and $x_E(t)$ denote the positions of the cargo, AAA+ rings A and B, and MTBDs D and E respectively at time $t \in [0, T]$ for some end time $T > 0$, taking $\mathbf{x} = [x_C(t), x_A(t), x_B(t), x_D(t), x_E(t)]$. We define $F_C(t)$ to be a force acting on the cargo from external effects that varies over time. This force could be caused by other motor proteins, such as kinesins, for example. In order to model the effects of ATP hydrolysis we initially assume that a force, denoted by $F_A(\mathbf{x}, t)$ and $F_B(\mathbf{x}, t)$, acts on AAA+ rings A and B respectively and is dependent on the positions of the AAA+ rings and MTBDs and varies over time. We assume

that there are forces acting between the microtubule and the MTBDs. We refer to these forces as binding affinities and denote them by $g_D(\mathbf{x}, t)$ and $g_E(\mathbf{x}, t)$ for MTBDs D and E respectively. We assume that they depend on the positions of the AAA+ rings and MTBDs and vary over time.

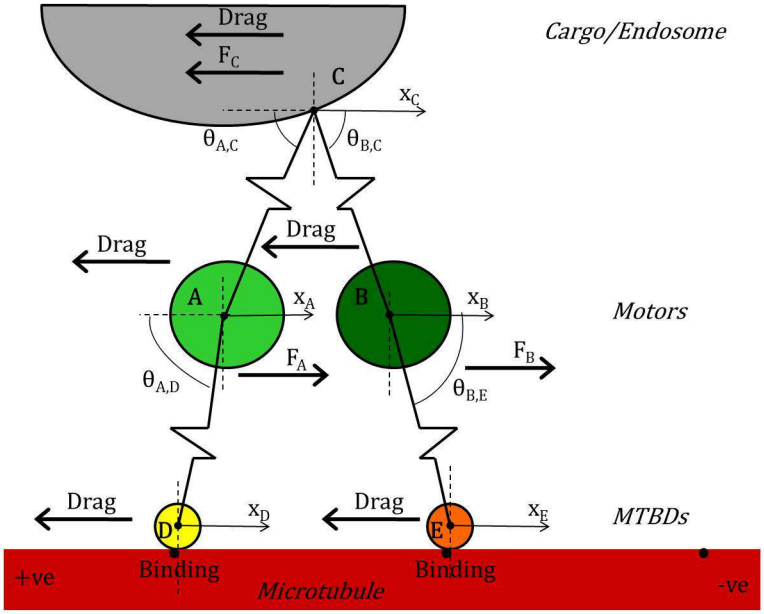

Figure 3.1: Schematic diagram of the mechanical model. The cargo is modelled as a sphere and depicted in grey. The dynein motor domain is modelled by two spheres, representing the AAA+ rings and depicted in green, connected via springs, representing the stalks, to two smaller spheres, representing the MTBDs D and E; depicted in yellow and orange respectively. The tail section of the dynein complex is modelled as two springs connecting the AAA+ rings to the cargo. The microtubule is modelled as a line and is depicted in red. Reproduced from Bulletin of Mathematical Biology, *From the Cell Membrane to the Nucleus: Unearthing Transport Mechanisms for Dynein*, v.7, 2012, p.2032, Laurie Crossley, Caroline A. Garrett, Majid Hafezparast and Anotida Madzvamuse, (© Society of Mathematical Biology 2012) with permission of Springer [9].

Three main results are used to model the forces acting on the complex: Newton's second law of motion, Hooke's law, and Stokes' law. Newton's second law of motion states that the rate of change of momentum of a body must be equal to the net forces acting on it:

$$\frac{d}{dt}\Big(m(t)\frac{dx(t)}{dt}\Big) = \sum_{i=1}^{n} F_i(x,t),$$

where $m(t)$ is the mass, $x(t)$ is the position of the body at time t and F_i are the n forces acting on the body. We assume that the masses of the cargo, AAA+ rings and MTBDs remain constant and hence this translates to equating the mass multiplied by the acceleration to the net force:

$$m\frac{d^2x(t)}{dt^2} = \sum_{i=1}^{n} F_i(x,t).$$

If we assume that the springs are linear, then we can use Hooke's law to model the force exerted

by the springs, this states that the spring force is proportional to the displacement:

$$F_1(t) = K(y(t) - l), \tag{3.1}$$

where F_1 is the force exerted by the spring, l is the unstressed length of the spring, y is the length of the spring and K is the associated spring constant [156]. We are considering the motion of a complex inside the cytoplasm *in vivo* or in a viscous medium *in vitro*, hence the complex and the cargo will experience viscous drag. Stokes' law states that for a spherical body with low Reynolds number the viscous drag can be modelled as proportional to the settling velocity:

$$F_2 = -6\pi\eta R v, \tag{3.2}$$

where F_2 is the frictional force, η the dynamic viscosity, R the radius of the sphere and v the settling velocity [156].

Remark 3.0.1. In order to apply Stokes' law, we assume that the viscous forces dominate the motion and that the cargo and components of the complex have a low Reynolds number. The Reynolds number is given by $Re = \frac{\rho L v}{\eta}$ where η is the viscosity, ρ is the density of the fluid, L is the length and v is the velocity [156]. Howard gives the Reynolds number for a protein and bacterium to be 0.05 and 5×10^{-5} respectively [156], if we use similar values for the viscosity and density of the fluid we obtain $Re \leq 3 \times 10^{-6}$ for a maximum length of 1000nm (see Table 3.1) and maximum velocity of $3\mu\text{ms}^{-1}$ [84]. Therefore, the assumption of low Reynolds number is appropriate.

Remark 3.0.2. For Stokes' law to apply, the Knudsen number (K_n) must also be low, with $K_n < 1$. The Knudsen number is given by $K_n = \frac{\lambda}{L}$ where λ is the mean free path and L is the representative physical length [157]. The mean free path in an aqueous solution under normal conditions can be computed to be approximately $\lambda = 0.1$ to 0.3nm [157]. Assuming a no-slip condition, the Knudsen number must satisfy $K_n < 0.01$ [158] and hence the characteristic length must satisfy $L > 30$nm. Given the size of the cargo, with radius greater than 100nm (see Table 3.1), the characteristic length would indeed exceed 30nm. Note that the characteristic lengths of the AAA+ rings and MTBDs satisfy $K_n < 0.1$, which suggests that continuum methods can be used but that there may be benefits from applying statistical mechanics, which could be the subject of future research [157]. It should also be noted that the mean free path in the cytoplasm could be much lower than in an aqueous solution due to the presence of other molecules, organelles and cytoskeletal structures which may reduce the value of the Knudsen number further, thereby strengthening the case for the use of the continuum model.

Using these results, the following system of second order non-linear ordinary differential equations (ODEs) is derived:

$$\begin{aligned}
m_C\frac{d^2x_C}{dt^2} =& K_{B,C}\Big[x_B - x_C - L_{B,C}\cos[\theta_{B,C}(\mathbf{x},t)]\Big] \\
&- K_{A,C}\Big[x_C - x_A - L_{A,C}\cos[\theta_{A,C}(\mathbf{x},t)]\Big] - F_C - \gamma_C\frac{dx_C}{dt}, \qquad (3.3)\\
m_A\frac{d^2x_A}{dt^2} =& F_A(\mathbf{x},t) + K_{A,C}\Big[x_C - x_A - L_{A,C}\cos[\theta_{A,C}(\mathbf{x},t)]\Big] \\
&- K_{A,D}\Big[x_A - x_D - L_{A,D}\cos[\theta_{A,D}(\mathbf{x},t)]] - \gamma_A\frac{dx_A}{dt}, \qquad (3.4)\\
m_B\frac{d^2x_B}{dt^2} =& F_B(\mathbf{x},t) + K_{B,E}\Big[x_E - x_B - L_{B,E}\cos[\theta_{B,E}(\mathbf{x},t)]\Big] \\
&- K_{B,C}\Big[x_B - x_C - L_{B,C}\cos[\theta_{B,C}(\mathbf{x},t)]\Big] - \gamma_B\frac{dx_B}{dt}, \qquad (3.5)\\
m_D\frac{d^2x_D}{dt^2} =& g_D(\mathbf{x},t) + K_{A,D}\Big[x_A - x_D - L_{A,D}\cos[\theta_{A,D}(\mathbf{x},t)]\Big] - \gamma_D\frac{dx_D}{dt}, \qquad (3.6)\\
m_E\frac{d^2x_E}{dt^2} =& g_E(\mathbf{x},t) - K_{B,E}\Big[x_E - x_B - L_{B,E}\cos[\theta_{B,E}(\mathbf{x},t)]\Big] - \gamma_E\frac{dx_E}{dt}, \qquad (3.7)
\end{aligned}$$

for $t \in [0,T]$ and $\mathbf{x} = [x_C, x_A, x_B, x_D, x_E]$. Note that we denote by B,C the connection between B and C and similarly for other connections. The full derivations are detailed below.

Remark 3.0.3. The assumption that the mass of the cargo will remain constant is significant for modelling *in vivo* events. During endocytosis the mass of a vesicle or endosome will change significantly as it moves from the cell membrane towards the nucleus due to fission and fusion [12, 14]. For *in vitro* events, latex beads or Qdots are used in experiments which can be approximated well by spheres with constant mass. In future studies, a more complex system could be derived in order to model the mass and shape changes of an endosome *in vivo*.

First, the derivation of the equation of motion for the cargo (3.3) is presented. Let m_C denote the mass of the cargo, then on the left hand side of the equation we have the mass multiplied by the acceleration, i.e.

$$m_C\frac{d^2x_C}{dt^2}.$$

The right hand side is given by the net forces acting on the cargo. There are two spring forces acting on the cargo: the spring force between the cargo and AAA+ ring A, denoted by $F_{A,C}$, and the spring force from the spring connecting the cargo to AAA+ ring B, similarly denoted by $F_{B,C}$. Using Hooke's law, (3.1), and evaluating the force in the horizontal direction by trigonometry gives:

$$F_{B,C} = K_{B,C}\Big[\frac{x_B - x_C}{\cos[\theta_{B,C}(\mathbf{x},t)]} - L_{B,C}\Big]\cos[\theta_{B,C}(\mathbf{x},t)],$$

where $K_{B,C}$ is the spring constant associated with the spring, $L_{B,C}$ is the unstressed length of the

spring, $\theta_{B,C}(\mathbf{x},t)$ is the acute angle of the spring from the horizontal and

$$\frac{x_B - x_C}{\cos[\theta_{B,C}(\mathbf{x},t)]}$$

is the length of the spring at time t. This simplifies to:

$$F_{B,C} = K_{B,C}\Big[x_B - x_C - L_{B,C}\cos[\theta_{B,C}(\mathbf{x},t)]\Big].$$

Similarly, the spring force for the spring connecting the cargo to AAA+ ring A is given by:

$$F_{A,C} = -K_{A,C}\Big[x_C - x_A - L_{A,C}\cos[\theta_{A,C}(\mathbf{x},t)]\Big],$$

where $K_{A,C}$ is the spring constant, $L_{A,C}$ is the unstressed spring length and $\theta_{A,C}(\mathbf{x},t)$ is the acute angle of the spring from the horizontal. Note, that this force is acting in the negative direction. As described above, a force F_C also acts on the cargo from external sources. This force is assumed to be constant over time and is fixed as a parameter value. The cargo will also be subjected to viscous drag, denoted by D_C, which can be modelled using Stokes' law, (3.2):

$$D_C = -\gamma_C \frac{dx_C}{dt},$$

where $\gamma_C = 6\pi\eta R_C$ is the damping coefficient with η the viscosity of the cytoplasm and R_C the radius of the cargo. The force is negative as it acts in the opposite direction to the velocity to oppose motion. The forces $F_{B,C}$, $F_{A,C}$, F_C and D_C can then be summed to obtain the right hand side of equation (3.3). This completes the derivation of the equation of motion for the cargo.

The equation of motion for AAA+ ring A (3.4) is derived in a similar fashion, with the left hand side given by

$$m_A \frac{d^2 x_A}{dt^2}$$

where m_A denotes the mass of AAA+ ring A. For the right hand side of the equation, the net force is considered. To model the effects of ATP hydrolysis, it is assumed that AAA+ ring A produces a force $F_A(\mathbf{x},t)$, the exact form of this function will be investigated in Chapter 4. As derived above, the spring force between AAA+ ring A and the cargo is given by:

$$-F_{A,C} = K_{A,C}\Big[x_C - x_A - L_{A,C}\cos[\theta_{A,C}(\mathbf{x},t)]\Big],$$

with the force acting in the positive direction with respect to AAA+ ring A. There is also a spring force from the spring connecting AAA+ ring A to MTBD D, denoted by $F_{A,D}$. Using Hooke's law

the force can be expressed as:

$$F_{A,D} = -K_{A,D}\Big[x_A - x_D - L_{A,D}\cos[\theta_{A,D}(\mathbf{x},t)]\Big],$$

where $K_{A,D}$ is the spring constant, $L_{A,D}$ is the unstressed spring length and $\theta_{A,D}(\mathbf{x},t)$ is the acute angle of the spring. Note that this spring force also acts in the negative direction. The viscous drag acting on the AAA+ ring, denoted D_A, is modelled using Stokes' law and hence:

$$D_A = -\gamma_A \frac{dx_A}{dt},$$

where $\gamma_A = 6\pi\eta R_A$ is the damping coefficient with R_A the radius of the AAA+ ring A. These forces are summed to give the right hand side of equation (3.4).

The equation of motion for AAA+ ring B (3.5) can be derived similarly with parameters $K_{B,E}$, $L_{B,E}$ and $\theta_{B,E}(\mathbf{x},t)$ representing the spring constant, unstressed length and acute angle for the spring between AAA+ ring B and MTBD E respectively; γ_B the damping coefficient with R_B the radius; $F_B(\mathbf{x},t)$ the force produced by AAA+ ring B during ATP hydrolysis and m_B the mass of AAA+ ring B.

Let m_D denote the mass of MTBD D, then the left hand side of the equation of motion of MTBD D (3.6) is given by:

$$m_D \frac{d^2 x_D}{dt^2}.$$

To obtain the right hand side of equation (3.6) the forces acting on MTBD D must be balanced. The spring force between MTBD D and AAA+ ring A is given as above:

$$-F_{A,D} = K_{A,D}\Big[x_A - x_D - L_{A,D}\cos[\theta_{A,D}(x_A, x_B)]\Big],$$

where the force acts in a positive direction on MTBD D. It is also assumed that there is a binding force acting on the MTBD in order to keep it bound to the microtubule. This binding affinity is denoted by $g_D(\mathbf{x},t)$ and the form of the function will be investigated later in the study. A viscous drag will also act on MTBD D, denoted by D_D and given by:

$$D_D = -\gamma_D \frac{dx_D}{dt},$$

from Stokes' law where $\gamma_D = 6\pi\eta R_D$ is the damping coefficient with R_D the radius of MTBD D.

The derivation of the equation of motion of MTBD E is similar, where $g_E(\mathbf{x},t)$ denotes the

binding affinity, γ_E the damping coefficient with R_E the radius, and m_E the mass of MTBD E.

To proceed, the following reasonable mathematical assumptions are made:

- The springs between the AAA+ rings and the cargo are equivalent;

$$\begin{cases} K_{A,C} = K_{B,C} =: K_C, \\ L_{A,C} = L_{B,C} =: L_C. \end{cases} \tag{A1}$$

- The springs between the AAA+ rings and the MTBDs are equivalent;

$$\begin{cases} K_{A,D} = K_{B,E} =: K_S, \\ L_{A,D} = L_{B,E} =: L_S. \end{cases} \tag{A2}$$

- The masses of the AAA+ rings are equal and the masses of the MTBDs are equal;

$$\begin{cases} m_A = m_B =: m_M, \\ m_D = m_E =: m_S. \end{cases} \tag{A3}$$

- The damping coefficients of the AAA+ rings are equal and the damping coefficients of the MTBDs are equal;

$$\begin{cases} \gamma_A = \gamma_B =: \gamma_M, \\ \gamma_D = \gamma_E =: \gamma_S. \end{cases} \tag{A4}$$

- The cargo is allowed to move freely, it is only subjected to the action of a single motor in a viscous medium and undergoes no fusion or fission. Hence, there is no added force such as that from other motors or from an optical trap;

$$F_C = 0. \tag{A5}$$

- The cargo is pulled by dynein such that its tail section is horizontal;

$$\begin{cases} \theta_{B,C} = 0, \\ \theta_{A,C} = \pi. \end{cases} \tag{A6}$$

- The stalks are at an angle such that:

$$\begin{cases} \cos[\theta_{A,D}(\mathbf{x},t)] \approx 0, \\ \cos[\theta_{B,E}(\mathbf{x},t)] \approx 0. \end{cases} \tag{A7}$$

Note that some of the above assumptions, (A5) - (A7), will be adapted in later chapters and relaxed in future studies. The goal here is to derive the most amenable model possible.

Remark 3.0.4. The simplifying assumption of fixed angles means that the AAA+ rings and cargo will move according to the extension and relaxation of the springs horizontally. This is an appropriate assumption for the model whilst we remain in one space dimension but will need to be considered when moving to higher dimensions. It is likely that there is some rigidity within the complex with regards to these angles, with the main variation arising from the conformational change under ATP hydrolysis. A stochastic model in two space dimensions with variable angles is considered in Chapter 5.1.

Using assumptions (A1), (A2), (A5)-(A7) reduces equations (3.3) - (3.7) to:

$$\begin{aligned} m_C\frac{d^2x_C}{dt^2} + \gamma_C\frac{dx_C}{dt} + 2K_Cx_C &= K_C(x_A + x_B - 2L_C), \\ m_A\frac{d^2x_A}{dt^2} + \gamma_A\frac{dx_A}{dt} + (K_C + K_S)x_A &= F_A(\mathbf{x},t) + K_Cx_C + K_Sx_D + K_CL_C, \\ m_B\frac{d^2x_B}{dt^2} + \gamma_B\frac{dx_B}{dt} + (K_C + K_S)x_B &= F_B(\mathbf{x},t) + K_Cx_C + K_Sx_E + K_CL_C, \\ m_D\frac{d^2x_D}{dt^2} + \gamma_D\frac{dx_D}{dt} + K_Sx_D &= g_D(\mathbf{x},t) + K_Sx_A, \\ m_E\frac{d^2x_E}{dt^2} + \gamma_E\frac{dx_E}{dt} + K_Sx_E &= g_E(\mathbf{x},t) + K_Sx_B. \end{aligned}$$

Applying the further assumptions (A3) and (A4) gives the following system of ordinary differential equations:

$$m_C\frac{d^2x_C}{dt^2} + \gamma_C\frac{dx_C}{dt} + 2K_Cx_C = K_C(x_A + x_B - 2L_C), \tag{3.8}$$

$$m_M\frac{d^2x_A}{dt^2} + \gamma_M\frac{dx_A}{dt} + (K_C + K_S)x_A = F_A(\mathbf{x},t) + K_Cx_C + K_Sx_D + K_CL_C, \tag{3.9}$$

$$m_M\frac{d^2x_B}{dt^2} + \gamma_M\frac{dx_B}{dt} + (K_C + K_S)x_B = F_B(\mathbf{x},t) + K_Cx_C + K_Sx_E + K_CL_C, \tag{3.10}$$

$$m_S\frac{d^2x_D}{dt^2} + \gamma_S\frac{dx_D}{dt} + K_Sx_D = g_D(\mathbf{x},t) + K_Sx_A, \tag{3.11}$$

$$m_S\frac{d^2x_E}{dt^2} + \gamma_S\frac{dx_E}{dt} + K_Sx_E = g_E(\mathbf{x},t) + K_Sx_B. \tag{3.12}$$

for $t \in [0,T]$.

3.1 Non-dimensionalisation

To achieve appropriate scaling we proceed to nondimensionalise the model system given by equations (3.8) - (3.12), setting:

$$x_C = \hat{x}_C\chi_C, \quad x_A = \hat{x}_A\chi_A, \quad x_B = \hat{x}_B\chi_B, \quad x_D = \hat{x}_D\chi_D, \quad x_E = \hat{x}_E\chi_E, \quad \text{and} \quad t = \hat{t}\tau;$$

with $\hat{x}_i$, $\hat{t}$ the characteristics and χ_i, τ the nondimensional variables for $i = A, B, C, D, E$. For scaling purposes, we will assume that the ATP force and binding affinities can be written in the form:

$$F_A(\mathbf{x}, t) = H\bar{F}_A(\chi, \tau),\ F_B(\mathbf{x}, t) = H\bar{F}_B(\chi, \tau),\ g_D(\mathbf{x}, t) = G\bar{g}_D(\chi, \tau),\ \text{and}\ g_E(\mathbf{x}, t) = G\bar{g}_E(\chi, \tau),$$

where H and G represent the maximum force produced during ATP hydrolysis or microtubule binding. Let M, L and T denote mass, length and time respectively, with megadaltons (MDa), nanometres (nm) and nanoseconds (ns) as the units of mass, length and time respectively. The dimensions of the model parameters are:

$$\begin{aligned}
[m_C] = [m_M] = [m_S] &= M, \\
[\gamma_C] = [\gamma_M] = [\gamma_S] &= MT^{-1}, \\
[K_C] = [K_S] &= MT^{-2}, \\
[G] = [H] &= MLT^{-2}, \\
[L_C] &= L.
\end{aligned}$$

The dimensions of the model variables are:

$$[x_C] = [x_A] = [x_B] = [x_D] = [x_E] = L, \quad \text{and} \quad [t] = T.$$

The characteristics are chosen as follows:

$$\begin{aligned}
x_C &= L_C\chi_C, \qquad x_A = \frac{H}{K_C + K_S}\chi_A, \qquad x_B = \frac{H}{K_C + K_S}\chi_B, \\
x_D &= \frac{G}{K_S}\chi_D, \qquad x_E = \frac{G}{K_S}\chi_E, \qquad \text{and} \quad t = \frac{\gamma_C}{K_C}\tau.
\end{aligned}$$

Substituting in equations (3.8) - (3.12) and simplifying gives:

$$\epsilon_1 \frac{d^2\chi_C}{d\tau^2} + \frac{d\chi_C}{d\tau} + 2\chi_C = b_1(\chi_A + \chi_B) - 2, \tag{3.13}$$

$$\epsilon_2 \frac{d^2\chi_A}{d\tau^2} + a_2 \frac{d\chi_A}{d\tau} + \chi_A = \bar{F}_A(\chi, \tau) + b_2\chi_C + c_2\chi_D + b_2, \tag{3.14}$$

$$\epsilon_2 \frac{d^2\chi_B}{d\tau^2} + a_2 \frac{d\chi_B}{d\tau} + \chi_B = \bar{F}_B(\chi, \tau) + b_2\chi_C + c_2\chi_E + b_2, \tag{3.15}$$

$$\epsilon_4 \frac{d^2\chi_D}{d\tau^2} + a_4 \frac{d\chi_D}{d\tau} + \chi_D = \bar{g}_D(\chi, \tau) + b_4\chi_A, \tag{3.16}$$

$$\epsilon_4 \frac{d^2\chi_E}{dt\tau^2} + a_4 \frac{d\chi_E}{d\tau} + \chi_E = \bar{g}_E(\chi, \tau) + b_4\chi_B, \tag{3.17}$$

where

$$\begin{aligned}
\epsilon_1 =& \frac{m_C K_C}{\gamma_C^2}, \quad \epsilon_2 = \frac{m_M K_C^2}{(K_C + K_S)\gamma_C^2}, \quad \epsilon_4 = \frac{m_S K_C^2}{K_S \gamma_C^2}, \\
a_2 =& \frac{\gamma_M K_C}{\gamma_C(K_C + K_S)}, \quad a_4 = \frac{\gamma_S K_C}{\gamma_C K_S}, \quad b_1 = \frac{H}{L_C(K_C + K_S)}, \\
b_2 =& \frac{K_C L_C}{H}, \quad b_4 = \frac{H K_S}{G(K_C + K_S)}, \quad c_2 = \frac{G}{H}.
\end{aligned}$$

It is reasonable to assume that $1 \leq K_C, K_S \leq 20$ [146], and using the values of our parameters given in Table 3.1 (converted to MDa, nm and ns) gives:

$$\epsilon_1 \leq \frac{m_C}{36000\pi^2}, \quad \epsilon_2 \leq \frac{m_M}{7200\pi^2}, \quad \text{and} \quad \epsilon_4 \leq \frac{m_S}{3600\pi^2}.$$

Hence, if the masses are small compared to the denominators, the coefficients of the acceleration terms in our equation will also be small. The mass of the dynein complex is 1.2MDa [26] hence $m_S < 1.2$ and $m_M < 1.2$. It follows that $\epsilon_2 \ll 1$ and $\varepsilon_4 \ll 1$. To the author's knowledge there are no experimental ranges for the mass of an endosome, hence our model parameter m_C is unknown. For experimental purposes Qdots can be used for monitoring endocytosis in cells. The largest Qdots, supplied by *Invitrogen - Life Technologies* (personal communication, 2012 [159]), are 800nm in size and have an estimated mass of 2MDa. We assume that Qdots can approximate endosomes well in experiments and hence take $m_C \leq 2$. It follows therefore that $\varepsilon_1 \ll 1$. The experimental data suggests strongly that the acceleration is small and the viscous forces dominate the dynamics [9, 146], therefore we assume that $\epsilon_1 \frac{d^2\chi_C}{d\tau^2} \ll 1$, $\epsilon_2 \frac{d^2\chi_M}{d\tau^2} \ll 1$ and $\epsilon_4 \frac{d^2\chi_S}{d\tau^2} \ll 1$. We

can now neglect the acceleration terms and our system becomes:

$$\frac{d\chi_C}{d\tau} + 2\chi_C = b_1(\chi_A + \chi_B) - 2, \tag{3.18}$$

$$a_2\frac{d\chi_A}{d\tau} + \chi_A = \bar{F}_A(\chi, \tau) + b_2\chi_C + c_2\chi_D + b_2, \tag{3.19}$$

$$a_2\frac{d\chi_B}{d\tau} + \chi_B = \bar{F}_B(\chi, \tau) + b_2\chi_C + c_2\chi_E + b_2, \tag{3.20}$$

$$a_4\frac{d\chi_D}{d\tau} + \chi_D = \bar{g}_D(\chi, \tau) + b_4\chi_A, \tag{3.21}$$

$$a_4\frac{d\chi_E}{d\tau} + \chi_E = \bar{g}_E(\chi, \tau) + b_4\chi_B, \tag{3.22}$$

where

$$\begin{aligned} a_2 =& \frac{\gamma_M K_C}{\gamma_C(K_C + K_S)}, \quad a_4 = \frac{\gamma_S K_C}{\gamma_C K_S}, \quad b_1 = \frac{H}{L_C(K_C + K_S)}, \\ b_2 =& \frac{K_C L_C}{H}, \quad b_4 = \frac{HK_S}{G(K_C + K_S)}, \quad \text{and} \quad c_2 = \frac{G}{H}. \end{aligned}$$

3.2 Parameter values

From Stokes' law the damping coefficients are given by:

$$\gamma_C = 6\pi\eta R_C, \quad \gamma_M = 6\pi\eta R_M \quad \text{and} \quad \gamma_S = 6\pi\eta R_S$$

where η is the viscosity, R_C, R_M and R_S are the radii of the cargo, AAA+ rings and microtubule-binding domains respectively. Hence, the coefficients in equations (3.18) - (3.22) can be expressed as:

$$\begin{aligned} a_2 =& \frac{R_M K_C}{R_C(K_C + K_S)}, \quad a_4 = \frac{R_S K_C}{R_C K_S}, \quad b_1 = \frac{H}{L_C(K_C + K_S)}, \\ b_2 =& \frac{K_C L_C}{H}, \quad b_4 = \frac{HK_S}{G(K_C + K_S)}, \quad \text{and} \quad c_2 = \frac{G}{H}. \end{aligned}$$

From experimental measurements, the motor domain exhibits a predominant step size of 16nm [30], with potential binding sites located approximately 8nm apart due to the structure of the microtubule [60, 160]. Hence, it is initially assumed that a MTBD binds to binding sites that are 16nm apart (see Remark 3.2.1). Furthermore, it is assumed that only one MTBD can bind to a binding site at any one time. The microtubule is modelled as a one dimensional line with possible binding sites 8nm apart. Let p_n, $n \in \mathbb{N}_0$, be the position of a binding site on a microtubule, where $p_{n+1} - p_n = 8$. MTBD D is assumed to bind to binding sites p_{2b} and MTBD E is assumed to bind to binding sites p_{2b+1} for $b \in \mathbb{N}_0$ (see Figure 3.2 [9]).

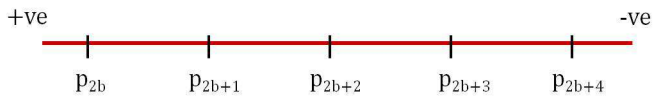

Figure 3.2: Diagram depicting the binding sites on the microtubule. Here the microtubule is modelled as a line. The +ve represents the cell membrane location and -ve the nucleus location. Reproduced from Bulletin of Mathematical Biology, *From the Cell Membrane to the Nucleus: Unearthing Transport Mechanisms for Dynein*, v.7, 2012, p.2032, Laurie Crossley, Caroline A. Garrett, Majid Hafezparast and Anotida Madzvamuse, (© Society of Mathematical Biology 2012) with permission of Springer [9].

Remark 3.2.1. Fixing the step size to 16nm with predetermined binding sites is a strong assumption on where the MTBDs can bind. The MTBD is restricted to binding to specific sites on the microtubule due to the position of tubulin [60, 160]. The displacement of the MTBD, under a conformational change during the ATP cycle, has been suggested to be close to the 16nm step size [55], with this being the predominant step size in studies [30]. Other step sizes have been recorded and shall be explored using a stochastic model in Chapter 6, however, here we will consider the simplest model of dynein stepping in one space dimension.

Consider a scaling parameter G representing the size of the force applied by the binding affinity to the microtubule. Assume that the binding affinity opposes the spring force applied by the stalk, with the maximum corresponding with a displacement of half the distance between the binding sites, hence $G = 4K_S$. The model parameters therefore consist of radii (R_C, R_M, R_S), spring constants (K_C, K_S), natural spring length (L_C) and force (H). The measured values of these parameters are given in Table 3.1.

3.3 Initial conditions

For simplicity the initial position of the cargo is taken to be at zero; the AAA+ rings are taken to be at a distance equal to the natural spring length (L_C) from the cargo; MTBD D is bound to initial binding site p_0 and MTBD E is bound to binding site $p_1 = p_0 + 8$:

$$\begin{cases} x_C(0) &= 0, \\ x_A(0) &= L_C \\ x_B(0) &= L_C, \\ x_D(0) &= p_0, \\ x_E(0) &= p_1 = p_0 + 8. \end{cases}$$

Parameter	Meaning	Experimental Values	Ref.	Primary Value (MDa,nm,ns)
R_C	Radius of the cargo	100-500 nm	[159, 161, 30]	100
R_M	Radius of the AAA+ ring	6.5 nm	[55]	6.5
R_S	Radius of the MTBD	2-4 nm	[59]	3
L_C	Unstressed length between the AAA+ ring and cargo	8-28 nm	[55]	10
K_C	Spring constant between the cargo and the AAA+ ring	Unmeasured	Estimated [146, 162]	1
K_S	Spring constant between the AAA+ ring and the MTBD	Unmeasured	Estimated [146, 162]	7
H	Force produced by the AAA+ ring	1-10 pN	[6]	10
η	Viscosity of the cytoplasm	2-50 cP	[163]	2

Table 3.1: Dimensional parameters, their given ranges and the primary values used in the mathematical model except where it is specified otherwise. Here we also include references for those parameter values we could find in the literature. The rest are estimated using plausible experimental ranges. Modified from Bulletin of Mathematical Biology, *From the Cell Membrane to the Nucleus: Unearthing Transport Mechanisms for Dynein*, v.7, 2012, p.2032, Laurie Crossley, Caroline A. Garrett, Majid Hafezparast and Anotida Madzvamuse, (© Society of Mathematical Biology 2012) with permission of Springer [9].

It is assumed for simplicity that the AAA+ rings start in a symmetrical position between the binding sites and hence $p_0 = L_C - 4$. Applying the non-dimensionalistation to the initial conditions gives:

$$\begin{cases} \chi_C(0) &= 0, \\ \chi_A(0) &= \frac{L_C}{H}(K_C + K_S), \\ \chi_B(0) &= \frac{L_C}{H}(K_C + K_S), \\ \chi_D(0) &= \frac{p_0}{4}, \\ \chi_E(0) &= \frac{p_0+8}{4}. \end{cases}$$

3.4 The model

Therefore the non-dimensional model system is given by:

$$\frac{d\chi_C}{d\tau} + 2\chi_C = b_1(\chi_A + \chi_B) - 2, \tag{3.23}$$

$$a_2\frac{d\chi_A}{d\tau} + \chi_A = \bar{F}_A(\chi,\tau) + b_2\chi_C + c_2\chi_D + b_2, \tag{3.24}$$

$$a_2\frac{d\chi_B}{d\tau} + \chi_B = \bar{F}_B(\chi,\tau) + b_2\chi_C + c_2\chi_E + b_2, \tag{3.25}$$

$$a_4\frac{d\chi_D}{d\tau} + \chi_D = \bar{g}_D(\chi,\tau) + b_4\chi_A, \tag{3.26}$$

$$a_4\frac{d\chi_E}{d\tau} + \chi_E = \bar{g}_E(\chi,\tau) + b_4\chi_B, \tag{3.27}$$

with initial conditions

$$\chi_C(0) = 0, \tag{3.28}$$

$$\chi_A(0) = \frac{L_C}{H}(K_C + K_S), \tag{3.29}$$

$$\chi_B(0) = \frac{L_C}{H}(K_C + K_S), \tag{3.30}$$

$$\chi_D(0) = \frac{p_0}{p_0 + 8 - L_C}, \tag{3.31}$$

$$\chi_E(0) = \frac{p_0 + 8}{p_0 + 8 - L_C}, \tag{3.32}$$

and coefficients

$$a_2 = \frac{\gamma_M K_C}{\gamma_C(K_C + K_S)}, \quad a_4 = \frac{\gamma_S K_C}{\gamma_C K_S}, \quad b_1 = \frac{H}{L_C(K_C + K_S)},$$
$$b_2 = \frac{K_C L_C}{H}, \quad b_4 = \frac{HK_S}{G(K_C + K_S)}, \quad \text{and} \quad c_2 = \frac{G}{H},$$

with model parameters given in Table 3.1. In Chapter 4, the model is solved numerically and plausible force functions are discussed. Two amendments to the model are discussed including the impact of the ATP force acting on the MTBD rather than the AAA+ ring and a multiple motor model.

3.5 Numerical simulations

The model system (3.23) - (3.27) with initial conditions (3.28) - (3.32) is solved numerically using the MATLAB solver *ode45* [164], for the time interval $[0, \tau_{Final}]$ and tolerances as given in Table 3.2. The *ode45* solver uses an explicit Runge-Kutta method with an adaptive time step; the

stopping criteria of each step in the ODE solver is:

$$|e_i| \leq \max\{RelTol|y_i|, AbsTol\},$$

where e_i is the estimated local error and y_i is the solution of the ODE at the ith step [164].

Remark 3.5.1. Smaller values of both the relative and absolute error tolerances were explored and the default values were found to be sufficient.

Parameter	Meaning	Primary Value
$RelTol$	Relative error tolerance	10^{-3}
$AbsTol$	Absolute error tolerance	10^{-6}
$[0, \tau_{Final}]$	Time interval to solve over	$[0, 7260\frac{K_C}{\gamma_C}]$

Table 3.2: Numerical parameters used for the numerical solver unless stated otherwise [164]. Note that the time intervals used for the stochastic models are more complex and are discussed in the relevant sections.

Remark 3.5.2. The derivation of the model formed part of previous work which was published under Bulletin of Mathematical Biology, *From the Cell Membrane to the Nucleus: Unearthing Transport Mechanisms for Dynein*, v.7, 2012, p.2032, Laurie Crossley, Caroline A. Garrett, Majid Hafezparast and Anotida Madzvamuse, (© Society of Mathematical Biology 2012) with permission of Springer [9]. The system was initially reduced to a three equation system, where the results were compared to experimental observations and parameter variations studied [9]. Previous work also explored and compared several types of functions to model the forces for the given five equation model [165].

Chapter 4

Continuous Five Equation Model

To investigate the behaviour of dynein during the transport process we explore plausible functions for both the ATP force and the binding affinity to the microtubule. As derived in the previous chapter, the model system is given by:

$$\frac{d\chi_C}{d\tau} + 2\chi_C = b_1(\chi_A + \chi_B) - 2, \tag{4.1}$$

$$a_2\frac{d\chi_A}{d\tau} + \chi_A = \bar{F}_A(\chi, \tau) + b_2\chi_C + c_2\chi_D + b_2, \tag{4.2}$$

$$a_2\frac{d\chi_B}{d\tau} + \chi_B = \bar{F}_B(\chi, \tau) + b_2\chi_C + c_2\chi_E + b_2, \tag{4.3}$$

$$a_4\frac{d\chi_D}{d\tau} + \chi_D = \bar{g}_D(\chi, \tau) + b_4\chi_A, \tag{4.4}$$

$$a_4\frac{d\chi_E}{d\tau} + \chi_E = \bar{g}_E(\chi, \tau) + b_4\chi_B, \tag{4.5}$$

with initial conditions

$$\begin{aligned}
\chi_C(0) &= 0, \\
\chi_A(0) &= \frac{L_C}{H}(K_C + K_S), \\
\chi_B(0) &= \frac{L_C}{H}(K_C + K_S), \\
\chi_D(0) &= \frac{p_0}{4}, \\
\chi_E(0) &= \frac{p_0 + 8}{4},
\end{aligned}$$

where

$$a_2 = \frac{\gamma_M K_C}{\gamma_C(K_C + K_S)}, \quad a_4 = \frac{\gamma_S K_C}{\gamma_C K_S}, \quad b_1 = \frac{H}{L_C(K_C + K_S)},$$
$$b_2 = \frac{K_C L_C}{H}, \quad b_4 = \frac{H K_S}{G(K_C + K_S)}, \quad \text{and} \quad c_2 = \frac{G}{H},$$

and model parameters are given in Table 3.1. We consider several plausible forcing functions, focusing on trigonometric functions although heavy-side and delta functions are also explored.

4.1 Spatially-dependent trigonometric force functions

In all cases we assume that the ATP cycle occurs continuously and we link the ATP force to the binding of the MTBD to the microtubule. In the first case, the binding affinities are modelled by cosine functions and are assumed to peak at the binding sites:

$$g_D(\mathbf{x}, t) = \frac{G}{2}\Big[\cos\Big(\frac{\pi}{8}(x_D - x_D(0))\Big) + 1\Big], \tag{4.6}$$

and

$$g_E(\mathbf{x}, t) = \frac{G}{2}\Big[\cos\Big(\frac{\pi}{8}(x_E - x_E(0))\Big) + 1\Big]. \tag{4.7}$$

This is plausible as the force acts at the binding site, preventing backward motion in order for dynein to step forwards. We also assume that there is a force near to the binding site that accounts for weakly bound heads and a bias for the MTBD to bind at the specific binding site. We assume that the force produced by the AAA+ ring would have a similar profile and choose that the force peak midway between the binding sites for its corresponding MTBD

$$F_A(\mathbf{x}, t) = \frac{H}{2}\Big[\cos\Big(\frac{\pi}{8}(x_D - x_D(0)) - \pi\Big) + 1\Big], \tag{4.8}$$

and

$$F_B(\mathbf{x}, t) = \frac{H}{2}\Big[\cos\Big(\frac{\pi}{8}(x_E - x_E(0)) - \pi\Big) + 1\Big]. \tag{4.9}$$

This is plausible as the ATP cycle is linked to the binding of the MTBD to the microtubule.

Remark 4.1.1. Variation of the position where the maximum force occurs between the binding sites does not affect our qualitative results; it only changes the step size of the MTBDs. We are only concerned with qualitative results for our initial studies hence the choice of this peak can be considered arbitrary. See Section 4.1.1 below.

Remark 4.1.2. We assume that the ATP cycle occurs continuously and choose periodic functions

in order to model coordinated motion. Stochasticity of the ATP cycle and uncoordinated motion is explored in Part II.

Figure 4.1 shows the transport profiles of the cargo, AAA+ rings A and B, MTBDs D and E, and the velocity profiles of the cargo, AAA+ rings and MTBDs, where $H = 10$ and $L_C = 10$. The profiles of the AAA+ rings and MTBDs show the hand-over-hand profile which persists almost periodically for all time. The cargo is moving progressively along the microtubule with an oscillatory velocity profile, reflecting what is seen in experiments [2, 9].

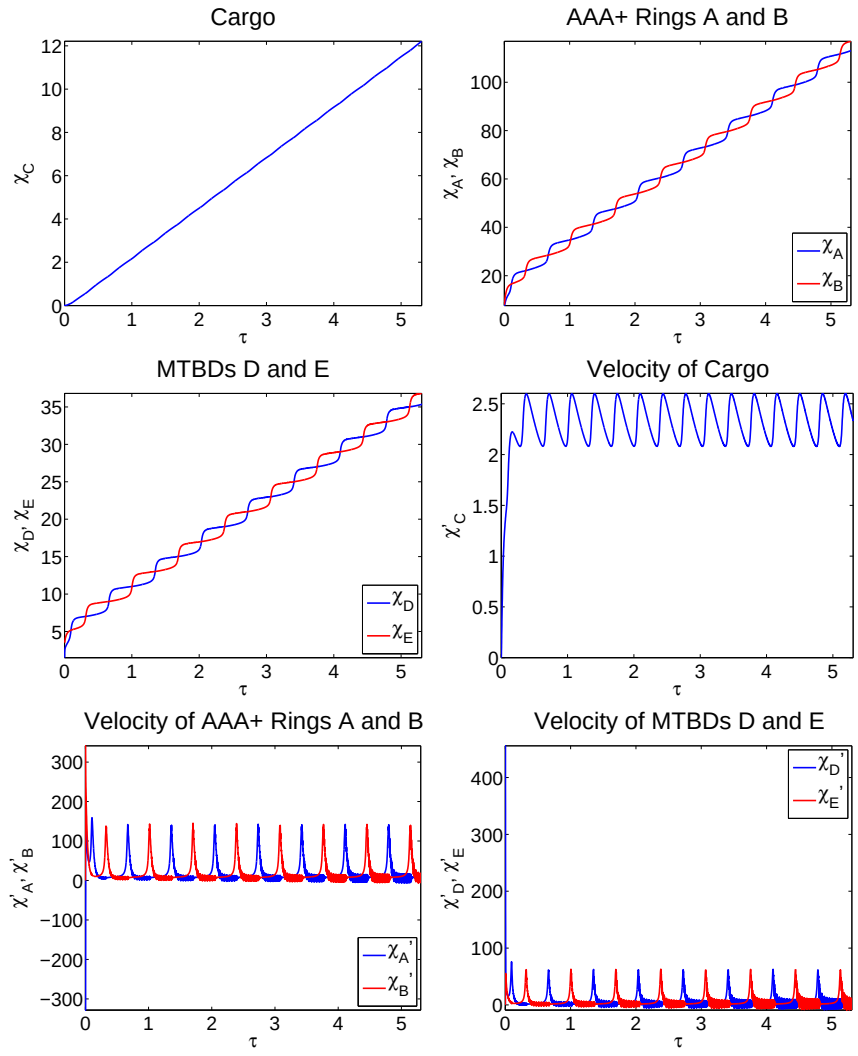

Figure 4.1: Plots of the numerical solutions to the model system (4.1) - (4.5) with functions as defined in equations (4.6) - (4.9) where we take our parameters to be at their primary values as given in Table 3.1, in particular $H = 10$ and $L_C = 10$, giving $\beta = 1$. See Section 3.5 for details of the numerical method. The profiles of the AAA+ rings and MTBDs show the hand-over-hand profile which persists almost periodically for all time. The cargo moves progressively along the microtubule with an oscillatory velocity profile, reflecting experimental observations (see [2, 9]).

4.1.1 Variation in the position of the maximum force on the microtubule

ATP hydrolysis by the motor domain is coordinated with the binding of the MTBD, hence we choose to model these forces using similar functions to those modelling the binding affinities. We model the binding affinities such that the force peaks at the corresponding binding sites, given previously by (4.6) and (4.7):

$$g_D(\mathbf{x},t) = \frac{G}{2}\Big[\cos\Big(\frac{\pi}{8}(x_D - x_D(0))\Big) + 1\Big],$$

and

$$g_E(\mathbf{x},t) = \frac{G}{2}\Big[\cos\Big(\frac{\pi}{8}(x_E - x_E(0))\Big) + 1\Big].$$

We want to use a similar function to model the ATP force, however it is unclear where the maximum of this force would occur with respect to the distance from a binding site. We therefore vary the point between the binding sites that the ATP force peaks by using the parameter w_1:

$$F_A(\mathbf{x},t) = \frac{H}{2}\Big[\cos\Big(\frac{\pi}{8}(x_D - x_D(0)) + w_1\pi\Big) + 1\Big], \tag{4.10}$$

and

$$F_B(\mathbf{x},t) = \frac{H}{2}\Big[\cos\Big(\frac{\pi}{8}(x_E - x_E(0)) + w_1\pi\Big) + 1\Big]. \tag{4.11}$$

The results all gave a walking profile with an oscillatory velocity profile (see Figure 4.2). The resultant change in profile is a change in the period of the steps over time, with the highest frequency of steps for $w_1 = 1$ and the lowest for $w_1 = 0$. Therefore, the choice of the parameter w_1 is arbitrary in order to achieve qualitatively accurate profiles.

4.1.2 Force strength variations

We consider the impact of a weak and strong binding affinity within the model, using the parameters $w_D, w_E \in [0,1]$ such that:

$$g_D(\mathbf{x},t) = w_D\frac{G}{2}\Big[\cos\Big(\frac{\pi}{8}(x_D - x_D(0))\Big) + 1\Big], \tag{4.12}$$

and

$$g_E(\mathbf{x},t) = w_E\frac{G}{2}\Big[\cos\Big(\frac{\pi}{8}(x_E - x_E(0))\Big) + 1\Big]. \tag{4.13}$$

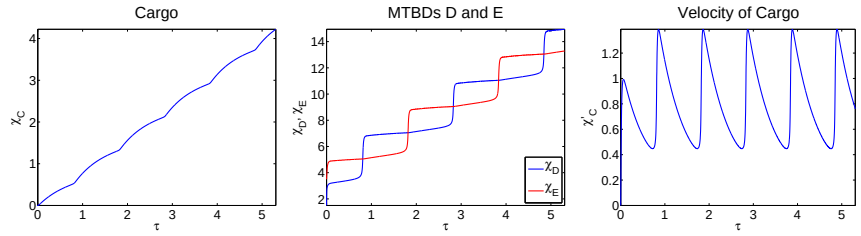

(a) $w_1 = 0$

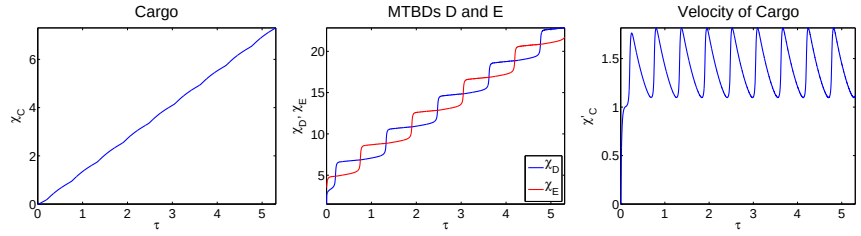

(b) $w_1 = 0.5$

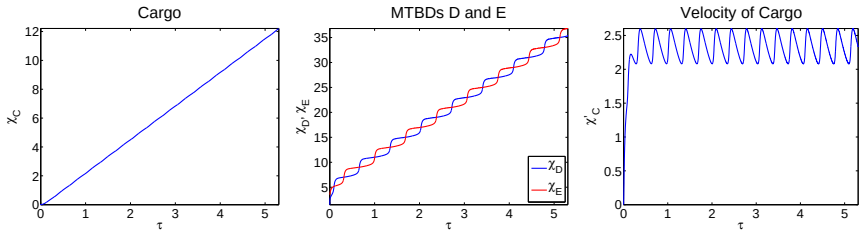

(c) $w_1 = 1$

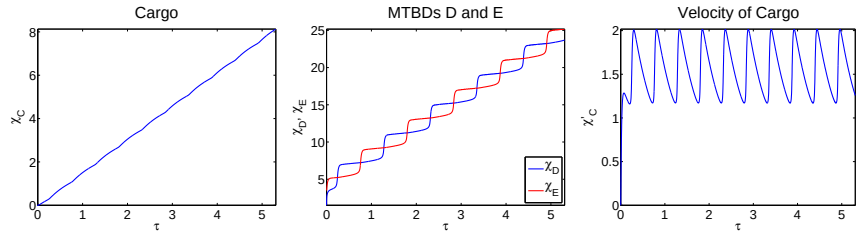

(d) $w_1 = 1.5$

Figure 4.2: Plots of the numerical solutions to the model system (4.1) - (4.5) with functions as defined in equations (4.6), (4.7), (4.10) and (4.11) where we take parameters to be at their primary values as given in Table 3.1, in particular $H = 10$ and $L_C = 10$, giving $\beta = 1$. See Section 3.5 for details of the numerical method. The parameter w_1 determines the point between the binding sites that the ATP force peaks (see equations (4.10) and (4.11)). Here we see that for all cases we have the same qualitative profiles, but that the change in location of the peak of the force on the microtubule leads to a qualitative change for the distance travelled by the cargo, step size of the MTBD and the range in which the velocity of the cargo oscillates. The highest number of steps occurs for $w_1 = 1$ and the lowest for $w_1 = 0$.

Setting $w_D = 1 - w_E$ and varying $w_E \in [0.5, 1]$ shows an increase in w_E, and decrease in w_D, leads to a change from a hand-over-hand walking to a shuffling stepping pattern and a reduction in the frequency of the steps (see Figure 4.3). We also tested the parameters jointly in both sets of functions for the specific values given by Qiu *et al.,* [32], who found that 74% of steps alternated and 83% of steps did not pass in time (see Figure 4.4). These results showed a clear shuffling pattern with one head in front of the other and alternating steps. Although one MTBD had a

more defined stepping profile suggesting that the rearward head was pulled forwards by the leading motor to some extent. The corresponding profiles for the cargo, AAA+ rings and their velocities for $w_D = 0.2$ and $w_E = 0.8$ are given in Figure 4.5. The AAA+ rings also exhibit the shuffling stepping pattern and the velocity of the cargo continues to be oscillatory with a less regular profile.

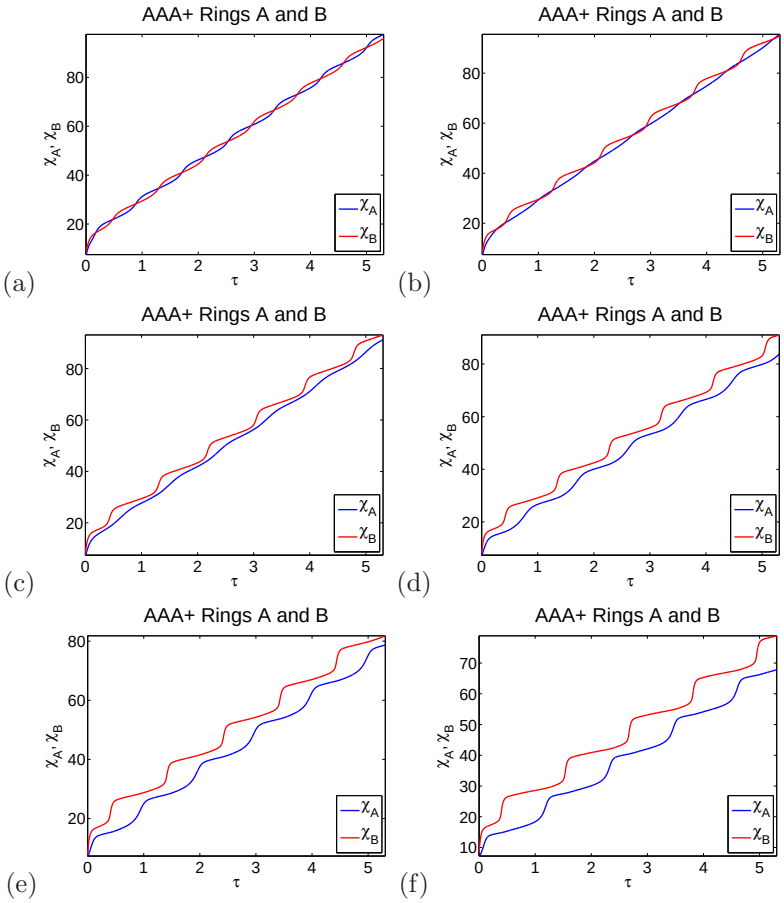

Figure 4.3: Plots of the numerical solutions to the model system (4.1) - (4.5) with functions as defined in equations (4.8), (4.9), (4.12) and (4.13) where we take parameters to be at their primary values as given in Table 3.1, in particular $H = 10$ and $L_C = 10$, giving $\beta = 1$. See Section 3.5 for details of the numerical method. Here we vary the parameters w_D and w_E, where $w_D = w_E - 1$ (a) $w_E = 0.5$, (b) $w_E = 0.6$, (c) $w_E = 0.7$, (d) $w_E = 0.8$, (e) $w_E = 0.9$ and (f) $w_E = 1$. We see that increasing w_E, and decreasing w_D, which increases the difference between the respective sizes of the forces, leads from a hand-over-hand profile to a shuffling profile.

We also consider using the parameters w_A and w_B for the ATP forces:

$$F_A(\mathbf{x}, t) = w_A \frac{H}{2}\Big[\cos\Big(\frac{\pi}{8}(x_D - x_D(0)) - \pi\Big) + 1\Big], \tag{4.14}$$

and

$$F_B(\mathbf{x}, t) = w_B \frac{H}{2}\Big[\cos\Big(\frac{\pi}{8}(x_E - x_E(0)) - \pi\Big) + 1\Big]. \tag{4.15}$$

Again, increasing w_A, and decreasing w_B, leads to a change from a hand-over-hand walking to a shuffling stepping pattern and a reduced frequency of steps (see Figure 4.6). We further tested the

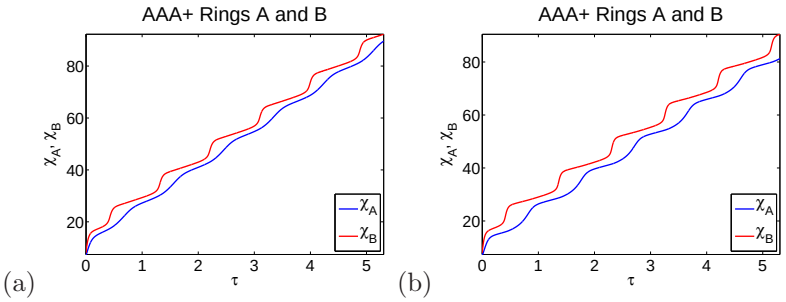

Figure 4.4: Plots of the numerical solutions to the model system (4.1) - (4.5) with functions as defined in equations (4.8), (4.9), (4.12) and (4.13) where we take parameters to be at their primary values as given in Table 3.1, in particular $H = 10$ and $L_C = 10$, giving $\beta = 1$. See Section 3.5 for details of the numerical method. Here we vary the parameters w_D and w_E, where $w_D = w_E - 1$ (a) $w_E = 0.74$ and (b) $w_E = 0.83$. We see that both values give a shuffling profile, with the trailing head having a slightly more pronounced step for the higher value.

parameters jointly in both sets of functions for the specific values given by Qiu *et al.,* [32], who found that 74% of steps alternated and 83% of steps did not pass in time (see Figure 4.7). These results showed a hand-over-hand walking pattern with one MTBD predominantly in the lead. The AAA+ rings also follow this pattern of stepping and whilst the velocity profile of the cargo remains oscillatory the magnitude of the oscillations are greater (see Figure 4.8).

We further study the effects of implementing both modified functions together. We assume that one head produces a stronger force but has a weaker binding affinity ($w_A = 0.8$, $w_D = 0.2$), whilst the other head produces a weaker force but has a stronger binding affinity ($w_B = 0.2$, $w_E = 0.8$). For this, we observe some interesting behaviour, there is a hand-over-hand pattern with one MTBD clearly stepping, whilst there are no discernible steps for the other MTBD (see Figure 4.9). Hence we made a slight change to the binding affinities by swapping the weakly and strongly bound MTBDs such that one head now produced a stronger force and had a stronger binding affinity ($w_A = 0.8$, $w_D = 0.8$), whilst the other head produced a weaker force and had a weaker binding affinity ($w_B = 0.2$, $w_E = 0.2$). Here, we again observe a hand-over-hand stepping pattern, however both heads now display a pronounced stepping profile (see Figure 4.10).

4.2 Bifurcation parameter

Numerical experiments reveal the existence of a bifurcation parameter $\beta = \frac{L_C}{H}$. Let $\delta_\pm \ll 1$, taking $1 - \delta_- < \beta < 1 + \delta_+$ causes the cargo to move forwards over time with a bounded velocity profile for the plausible functions considered. Taking $\beta > 1 + \delta_+$ gives a velocity profile which increases exponentially over time and by taking $\beta < 1 - \delta_-$ the cargo moves backwards tending towards stationary behaviour. Taking $\beta \in [1-\delta_-, 1+\delta_+]$ gives results reflecting experimental observations.

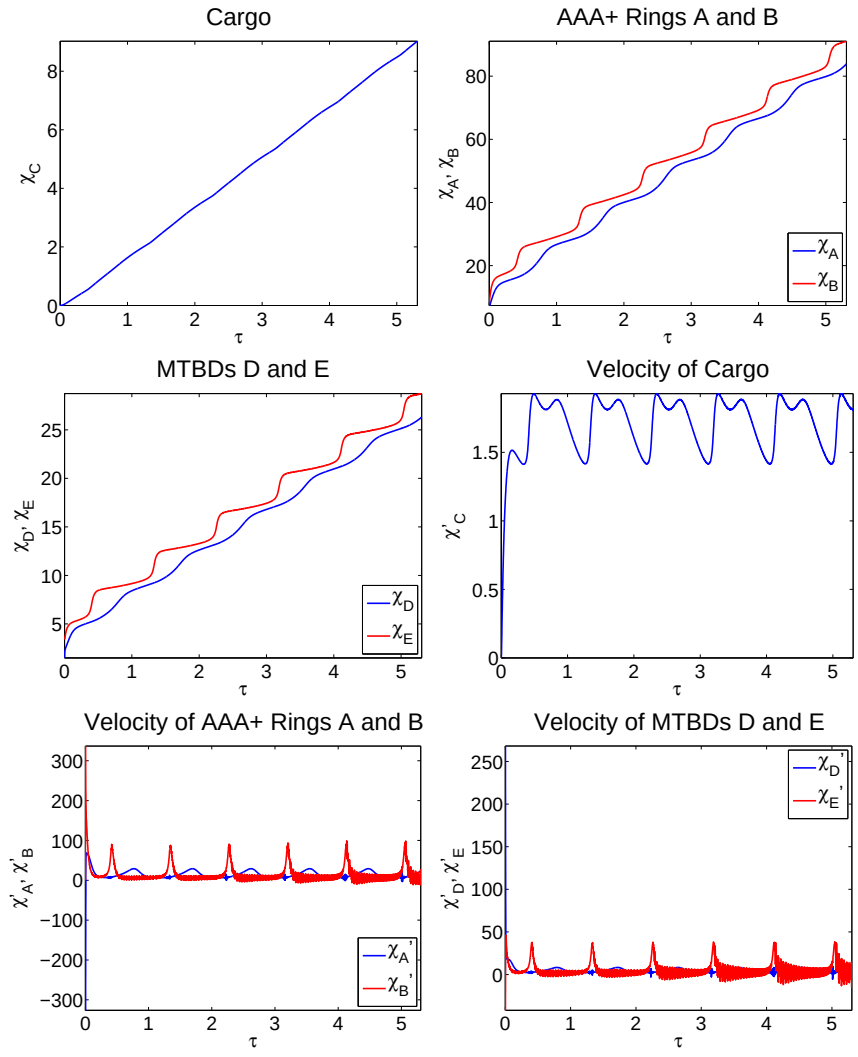

Figure 4.5: Plots of the numerical solutions to the model system (4.1)-(4.5) with functions as defined in equations (4.8), (4.9), (4.12) and (4.13) where $w_D = 0.2$, $w_E = 0.8$ and we take parameters to be at their primary values as given in Table 3.1, in particular $H = 10$ and $L_C = 10$, giving $\beta = 1$. See Section 3.5 for details of the numerical method. The profiles of the AAA+ rings and MTBDs show the shuffling profile which persists almost periodically for all time; one MTBD moves with a more pronounced stepping pattern suggesting that the lagging head is being dragged along the microtubule. The cargo moves progressively along the microtubule with an oscillatory velocity profile, reflecting experimental observations (see [2, 9]).

Other results may be a consequence of restrictions in our model, as dynein is a processive motor we would not expect to see exponential or stationary profiles. However, these profiles may reflect a parameter set for which dynein may fall off the microtubule or detach from the cargo, which is not possible in our current model but can be considered in future studies.

Within our studies on trigonometric functions we also found results that gave stationary behaviour for $\beta = 1$. For all functions resulting in this behaviour, regardless of their type, we also found that the cargo moved backwards for $\beta < 1$. This enables model selection as it limits the available functions to model the normal behaviour of dynein and may reflect the presence of steady

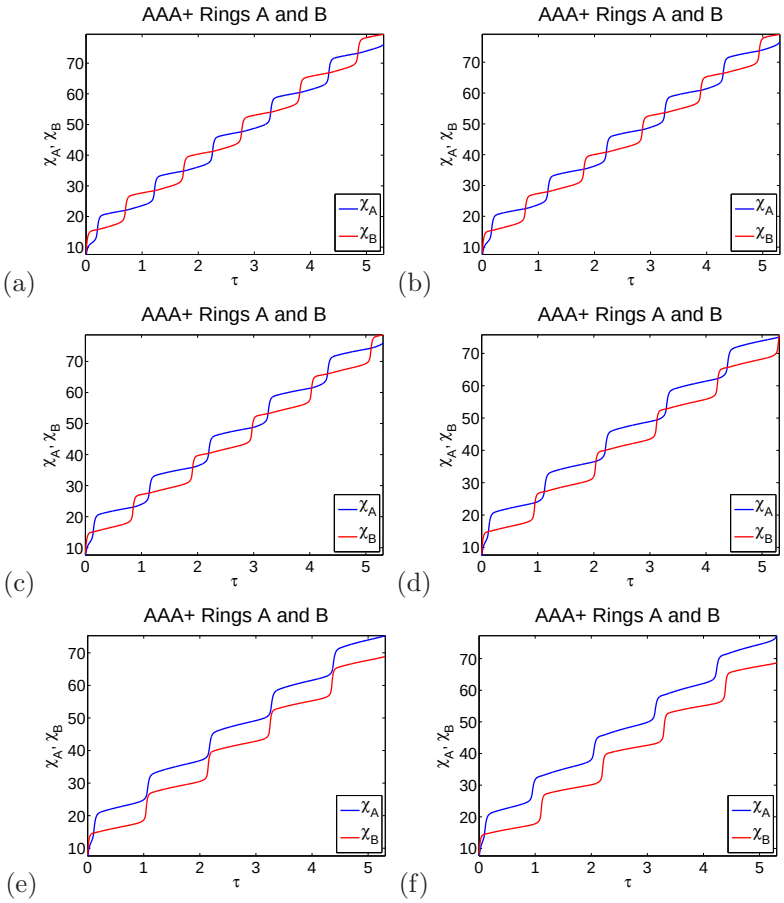

Figure 4.6: Plots of the numerical solutions to the model system (4.1) - (4.5) with functions as defined in equations (4.14), (4.15), (4.6) and (4.7) where we take our parameters to be at their primary values as given in Table 3.1, in particular $H = 10$ and $L_C = 10$, giving $\beta = 1$. See Section 3.5 for details of the numerical method. Here we vary the parameters p_1 and p_2, where $p_2 = 1 - p_1$ (a) $p_1 = 0.5$, (b) $w_A = 0.6$, (c) $w_A = 0.7$, (d) $w_A = 0.8$, (e) $w_A = 0.9$ and (f) $w_A = 1$. We see that increasing w_A, and decreasing w_B, which increases the difference between the respective sizes of the forces, leads from a hand-over-hand profile to a shuffling profile.

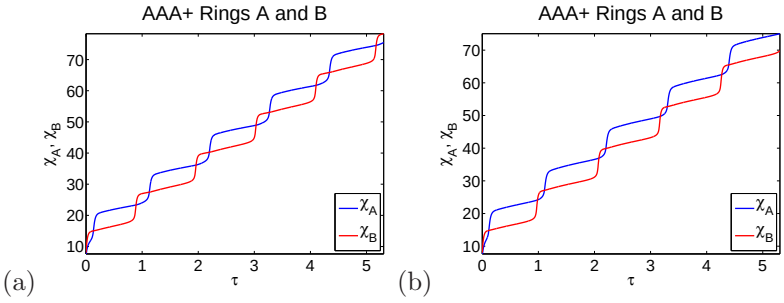

Figure 4.7: Plots of the numerical solutions to the model system (4.1) - (4.5) with functions as defined in equations (4.14), (4.15), (4.6) and (4.7) where we take parameters to be at their primary values as given in Table 3.1, in particular $H = 10$ and $L_C = 10$, giving $\beta = 1$. See Section 3.5 for details of the numerical method. Here we vary the parameters w_A and w_B, where $w_B = w_A - 1$ (a) $w_A = 0.74$ and (b) $w_A = 0.83$. Both profiles show a hand-over-hand profile but for the higher value of w_A the predominantly trailing head is in the lead for a small amount of time at each step.

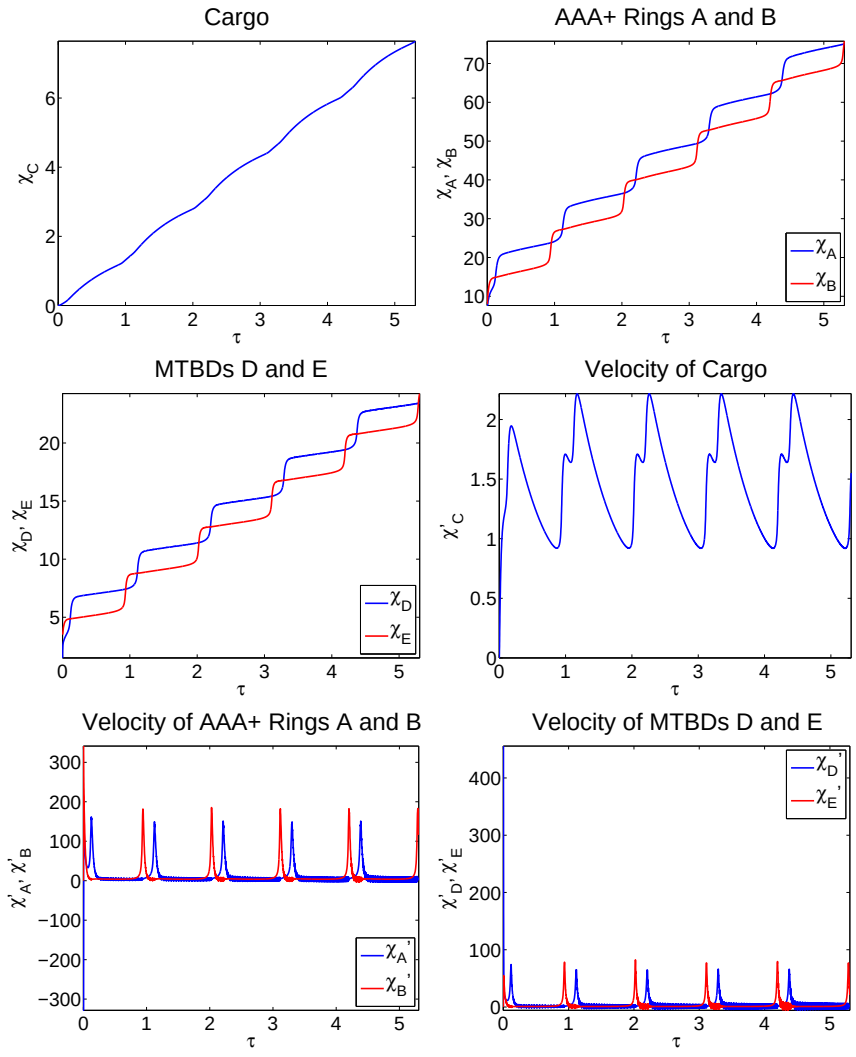

Figure 4.8: Plots of the numerical solutions to the model system (4.1) - (4.5) with functions as defined in equations (4.14), (4.15), (4.6) and (4.7) where $w_A = 0.8$, $w_B = 0.2$ and we take parameters to be at their primary values as given in Table 3.1, in particular $H = 10$ and $L_C = 10$, giving $\beta = 1$. See Section 3.5 for details of the numerical method. The profiles of the AAA+ rings and MTBDs show the hand-over-hand profile which persists almost periodically for all time, with steps relatively close together. The cargo is moving progressively along the microtubule with an oscillatory velocity profile, reflecting what is seen in experiments (see [2, 9]).

states within the model, which would not be suitable to model the processive nature of dynein.

Steady states of the model satisfy:

$$2\chi_C = b_1(\chi_A + \chi_B) - 2, \tag{4.16}$$

$$\chi_A = \bar{F}_A(\chi, \tau) + b_2\chi_C + c_2\chi_D + b_2, \tag{4.17}$$

$$\chi_B = \bar{F}_B(\chi, \tau) + b_2\chi_C + c_2\chi_E + b_2, \tag{4.18}$$

$$\chi_D = \bar{g}_D(\chi, \tau) + b_4\chi_A, \tag{4.19}$$

$$\chi_E = \bar{g}_E(\chi, \tau) + b_4\chi_B. \tag{4.20}$$

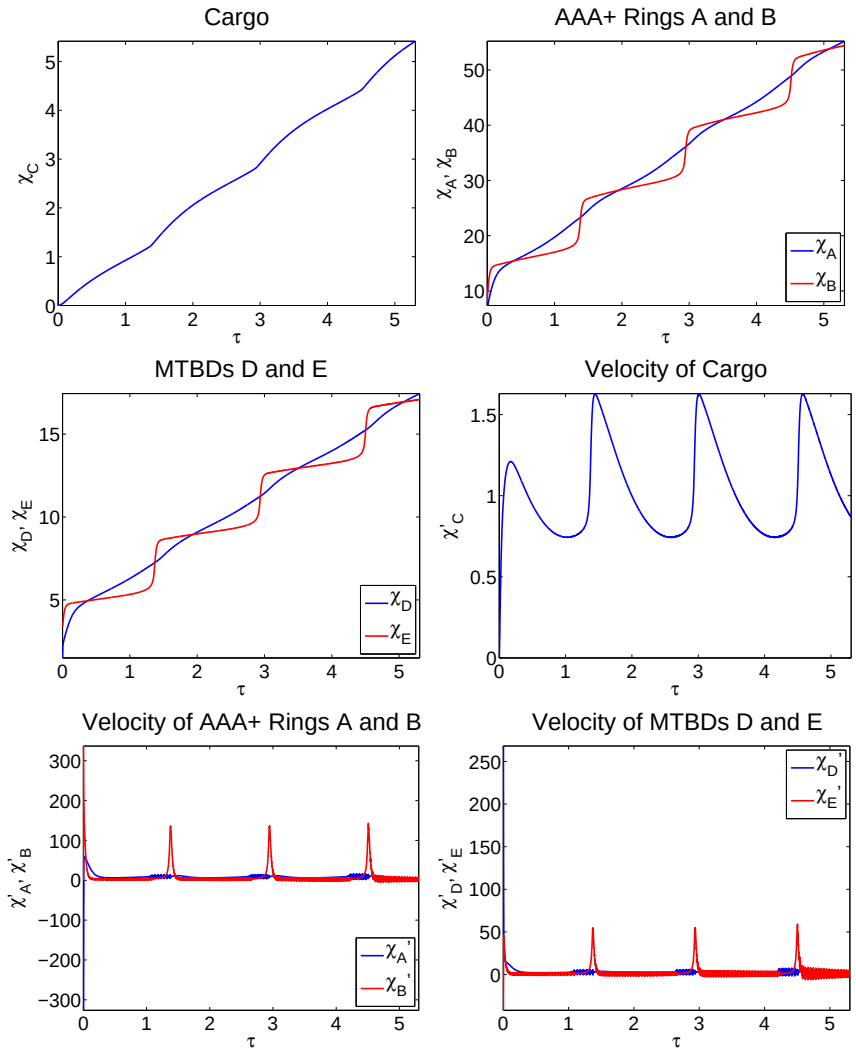

Figure 4.9: Plots of the numerical solutions to the model system (4.1) - (4.5) with functions as defined in equations (4.14), (4.15), (4.12) and (4.13) where $w_A = 0.8$, $w_B = 0.2$, $w_D = 0.2$, $w_E = 0.8$ and we take parameters to be at their primary values as given in Table 3.1, in particular $H = 10$ and $L_C = 10$, giving $\beta = 1$. See Section 3.5 for details of the numerical method. The profiles of the AAA+ rings and MTBDs show the hand-over-hand profile which persists almost periodically for all time; one MTBD has a more pronounced stepping pattern suggesting the other MTBD is being pushed or pulled along the microtubule. The cargo moves progressively along the microtubule with an oscillatory velocity profile, reflecting experimental observations (see [2, 9]).

Substituting for χ_D and χ_E in equations (4.17) and (4.18) gives:

$$\chi_A = \frac{1}{(1 - c_2 b_4)}[\bar{F}_A(\chi, \tau) + b_2\chi_C + c_2\bar{g}_D(\chi, \tau) + b_2], \tag{4.21}$$

$$\chi_B = \frac{1}{(1 - c_2 b_4)}[\bar{F}_B(\chi, \tau) + b_2\chi_C + c_2\bar{g}_E(\chi, \tau) + b_2]. \tag{4.22}$$

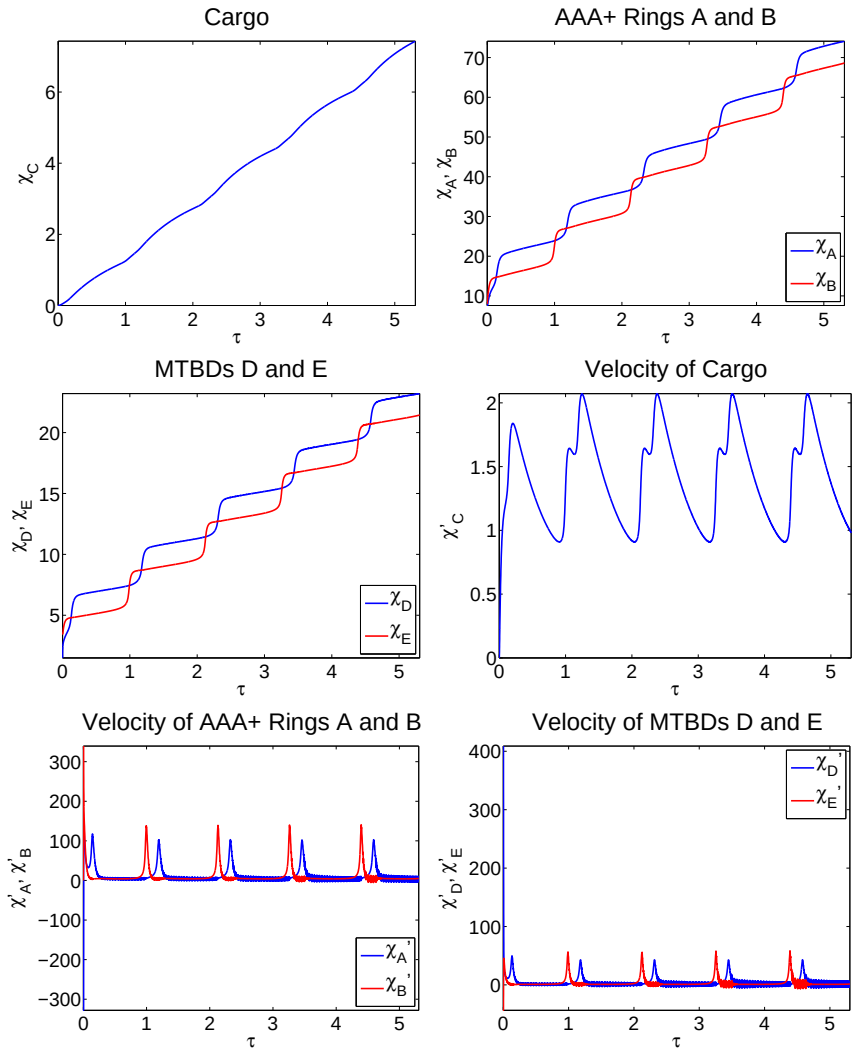

Figure 4.10: Plots of the numerical solutions to the model system (4.1) - (4.5) with functions as defined in equations (4.14), (4.15), (4.12) and (4.13) where $w_A = 0.8$, $w_B = 0.2$, $w_D = 0.8$, $w_E = 0.2$ and we take our parameters to be at their primary values as given in Table 3.1, in particular $H = 10$ and $L_C = 10$, giving $\beta = 1$. See Section 3.5 for details of the numerical method. The profiles of the AAA+ rings and MTBDs show the hand-over-hand profile which persists almost periodically for all time, with steps relatively close together. The cargo moves progressively along the microtubule with an oscillatory velocity profile, reflecting experimental observations (see [2, 9]).

By substituting for χ_A and χ_B in equation (4.16) we obtain:

$$2\chi_C = \frac{b_1}{(1-c_2b_4)}(\bar{F}_A(\chi,\tau) + \bar{F}_B(\chi,\tau) + 2b_2\chi_C + c_2\bar{g}_D(\chi,\tau) + c_2\bar{g}_E(\chi,\tau) + 2b_2) - 2. \tag{4.23}$$

This simplifies to

$$\bar{F}_A(\chi,\tau) + \bar{F}_B(\chi,\tau) + c_2\bar{g}_D(\chi,\tau) + c_2\bar{g}_E(\chi,\tau) = 0. \tag{4.24}$$

Hence, if the functions are defined such that this will never hold, there will be no stationary steady states ensuring processive motion. This is the case in our main choice of functions, with the dimensional forms defined by:

$$F_A(\mathbf{x},t) = \frac{H}{2}\Big[\cos\Big(\frac{\pi}{8}(x_D - x_D(0)) - \pi\Big) + 1\Big], \tag{4.25}$$

$$F_B(\mathbf{x},t) = \frac{H}{2}\Big[\cos\Big(\frac{\pi}{8}(x_E - x_E(0)) - \pi\Big) + 1\Big], \tag{4.26}$$

$$g_D(\mathbf{x},t) = \frac{G}{2}\Big[\cos\Big(\frac{\pi}{8}(x_D - x_D(0))\Big) + 1\Big], \tag{4.27}$$

$$g_E(\mathbf{x},t) = \frac{G}{2}\Big[\cos\Big(\frac{\pi}{8}(x_E - x_E(0))\Big) + 1\Big], \tag{4.28}$$

(and the variations of these given above). For this choice of functions we see that by taking $1 - \delta_- < \beta < 1 + \delta_+$ for some $\delta_{+,-} \ll 1$, the cargo moves forwards over time with a velocity profile that oscillates (See Figures 4.11 and 4.12). Taking $\beta > 1 + \delta_+$ gives a velocity profile which increases exponentially over time and by taking $1 - \delta_- > \beta$ the cargo moves backwards or tends towards stationary behaviour (See Figures 4.11 and 4.12).

Remark 4.2.1. We note that this specific behaviour only occurs for the *plausible* functions considered. Alternative functions give stationary profiles for $1 - \delta_- < \beta < 1 + \delta_+$ and backwards motion for $\beta < 1 - \delta_-$. However, all functions tested give a velocity profile which increases exponentially over time for $\beta > 1 + \delta_+$. (See Section 4.4.)

4.3 Parameter sensitivity analysis

We conducted a full parameter sensitivity analysis on our model and found in particular that for all the functions a decrease in parameters L_C and K_C, representing the spring length and constant of the spring connecting the cargo with the AAA+ ring, gave a reduced distance travelled and lower velocity for all functions (see Figure 4.13). This is significant in terms of the application of the model to mutation. For example mutations in the tail section of cytoplasmic dynein could impact on the model through the associated parameters within this section, that is the natural length L_C and the spring constant K_C. With regards to the *Loa* mutation, which occurs in this particular section of the structure of dynein, experimental evidence has shown that it causes a reduction in velocity and distance travelled which is achieved here through a reduction in L_C or K_C [2, 35, 36].

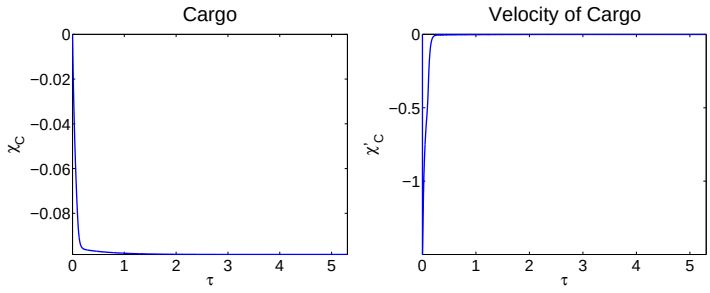

(a) $H = 10$, $L_C = 5$, $\beta = 0.5$

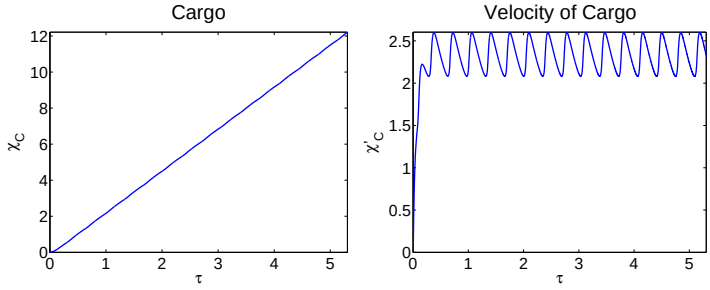

(b) $H = 10$, $L_C = 10$, $\beta = 1$

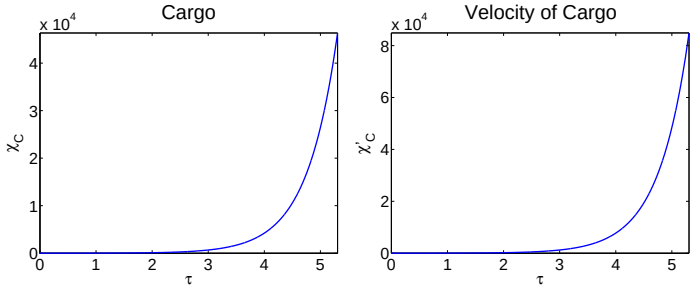

(c) $H = 10$, $L_C = 15$, $\beta = 1.5$

Figure 4.11: Plots of the numerical solutions to the model system (4.1) - (4.5) with functions as defined in equations (4.6) - (4.9) where we take parameters to be at their primary values as given in Table 3.1, and vary H and L_C. See Section 3.5 for details of the numerical method. We see that for $\beta = 1$ the cargo moves forwards over time with a velocity profile that oscillates. Taking $\beta = 1.5$ gives a velocity profile which increases exponentially over time and by taking $\beta = 0.5$ the cargo moves backwards and tends towards stationary behaviour.

4.4 Alternative spatially-dependent functions

Other forms of spatially-dependent functions were also explored including Dirac delta and heavy-side functions. These were considered plausible as they enable the forces to be switched on and off at certain points along the microtubule.

The Dirac delta function can be expressed in the form

$$\delta_a(x) = \frac{1}{a\sqrt{\pi}} e^{\frac{-x^2}{a^2}}$$

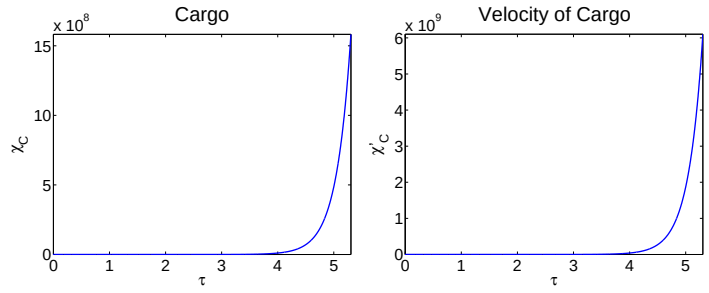

(a) $H = 10$, $L_C = 20$, $\beta = 2$

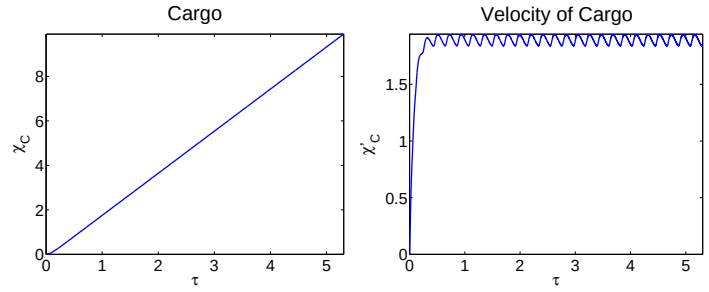

(b) $H = 20$, $L_C = 20$, $\beta = 1$

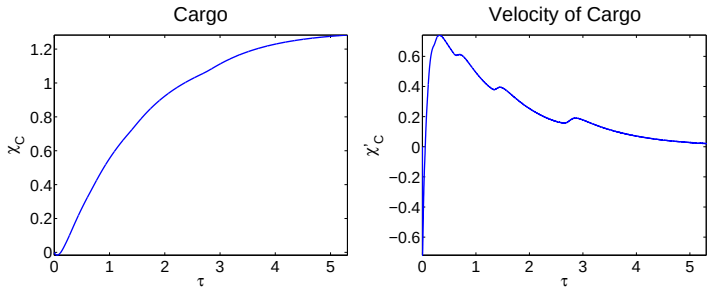

(c) $H = 25$, $L_C = 20$, $\beta = 0.8$

Figure 4.12: Plots of the numerical solutions to the model system (4.1) - (4.5) with functions as defined in equations (4.6) - (4.9) where we take parameters to be at their primary values as given in Table 3.1, and vary H and L_C. See Section 3.5 for details of the numerical method. We see that for $\beta = 1$ the cargo moves forwards over time with a velocity profile that oscillates. Taking $\beta = 2$ gives a velocity profile which increases exponentially over time and by taking $\beta = 0.8$ the cargo tends towards stationary behaviour.

where we let $a \to 0$. The parameter a can be used to control both the maximum value attained by the function $\delta_a(x)$ and the width. We assume that the AAA+ ring produces a force at all points except when its corresponding MTBD is at a binding site, setting:

$$F_A(\mathbf{x}, t) = 1 - \sum_{i=0}^{\infty} He^{-H^2\pi(x_D - p_{2i})^2}, \tag{4.29}$$

and

$$F_B(\mathbf{x}, t) = 1 - \sum_{i=0}^{\infty} He^{-H^2\pi(x_E - p_{2i+1})^2}, \tag{4.30}$$

where p_{2i} and p_{2i+1} are the binding sites for MTBDs D and E respectively. For the binding affinity, we assume that it is present when the MTBD is at, or very close to, a binding site. Additionally,

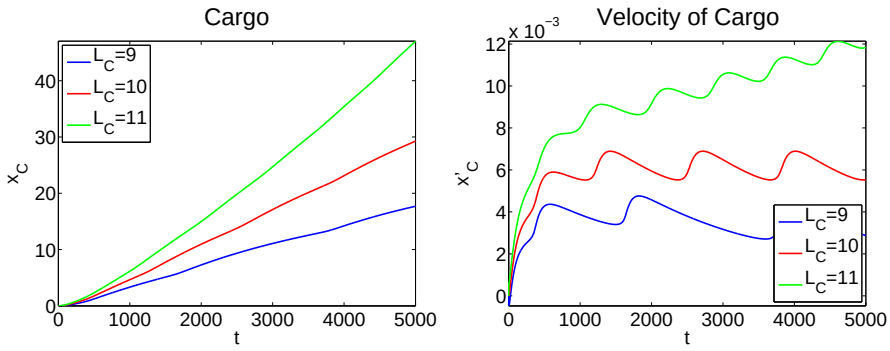

(a) Vary L_C

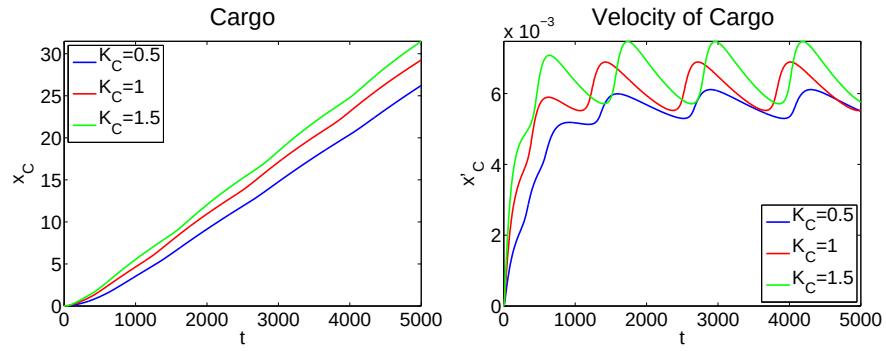

(b) Vary K_C

Figure 4.13: Plots of the dimensional numerical solutions to the model system (4.1) - (4.5) with parameter variations, with $H = 10$, $L_C = 10$, $K_C = 1$, except where specified otherwise, and all the other parameters are taken at their primary value given in Table 3.1. See Section 3.5 for details of the numerical method. We see that a decrease in parameters L_C and K_C, representing the spring length and constant of the spring connecting the cargo with the AAA+ ring, results in a reduced distance travelled and lower velocity.

we assume that it is acting in the positive direction when the corresponding MTBD is ahead of the other one, and in the negative direction when it is behind. That is, the binding affinity prevents the MTBD from moving backwards when it is in front but opposes motion when it is behind:

$$g_D(\mathbf{x}, t) = \frac{x_D - x_E}{|x_D - x_E|} \sum_{i=0}^{\infty} G e^{-G^2 \pi (x_D - p_{2i})^2}, \tag{4.31}$$

and

$$g_E(\mathbf{x}, t) = \frac{x_E - x_D}{|x_E - x_D|} \sum_{i=0}^{\infty} G e^{-G^2 \pi (x_E - p_{2i+1})^2}. \tag{4.32}$$

Note that if $x_D = x_E$ we take the binding affinity to act in the positive direction. Figure 4.14 shows the numerical results of the model system (4.1) - (4.5) with Dirac delta forcing functions. Here we see less oscillatory profiles than for the trigonometric functions. The two MTBDs follow similar trajectories, suggesting that these functions are less appropriate for modelling the behaviour of dynein. In general, similar results were achieved for all functions based on the Dirac delta functions, however for the parameter set $H = 10$ and $L_C = 10$ (i.e. $\beta = \frac{L_C}{H} = 1$) most results gave

stationary profiles.

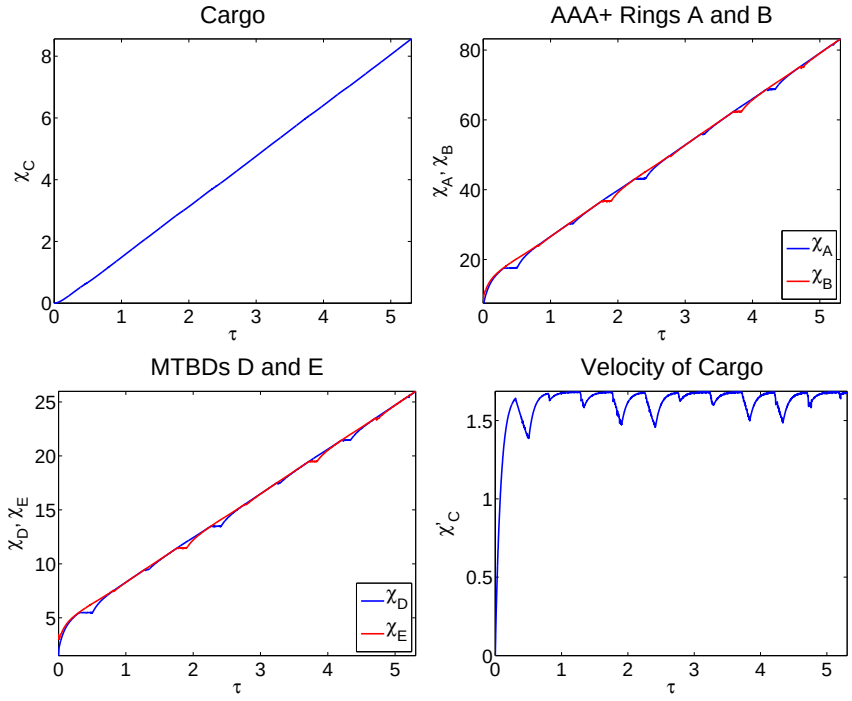

Figure 4.14: Plots of the numerical solutions to the model system with functions as defined in equations (4.29) - (4.32) where we take parameters to be at their primary values as given in Table 3.1, in particular $H = 10$ and $L_C = 10$, giving $\beta = 1$. See Section 3.5 for details of the numerical method. We see that the cargo moves progressively along the microtubule over time with an oscillatory velocity profile. The two MTBDs and two AAA+ rings move along similar trajectories, not in a clearly defined hand-over-hand or shuffling profile.

We also considered heavy-side functions, modelling the force produced by the AAA+ ring such that it produces a force when the distance between its corresponding MTBD and the other MTBD is less than 8nm, or it is behind the other MTBD. We set

$$F_A(\mathbf{x}, t) = \begin{cases} H & \text{if} \quad x_D - x_E < 8, \\ 0 & \text{otherwise}, \end{cases} \tag{4.33}$$

and

$$F_B(\mathbf{x}, t) = \begin{cases} H & \text{if} \quad x_E - x_D < 8, \\ 0 & \text{otherwise}. \end{cases} \tag{4.34}$$

For the binding affinities, we consider using them to impose in the model that the MTBD has zero velocity when it is ahead of the other MTBD and at a binding site i.e. it is not moving. We take

the binding affinity to be zero otherwise. This gives:

$$g_D(\mathbf{x},t) = \begin{cases} K_S(x_A - x_D) & \text{if} \quad x_D > x_E \quad \text{and} \quad x_D = p_{2b} \quad \text{for} \quad b \in \mathbb{N}, \\ 0 \quad \text{otherwise}, \end{cases} \tag{4.35}$$

and

$$g_E(\mathbf{x},t) = \begin{cases} K_S(x_B - x_E) & \text{if} \quad x_E > x_D \quad \text{and} \quad x_E = p_{2b-1} \quad \text{for} \quad b \in \mathbb{N}, \\ 0 \quad \text{otherwise}. \end{cases} \tag{4.36}$$

Figure 4.15 shows the numerical results of the model system (4.1) - (4.5) with heavy-side forcing functions. Here, we see that both MTBDs follow similar trajectories again suggesting that these functions are less appropriate for modelling the forces. We considered several other heavy-side functions, all giving similar results; however, most results again gave stationary profiles for the parameter set $H = 10, L_C = 10, \beta = 1$.

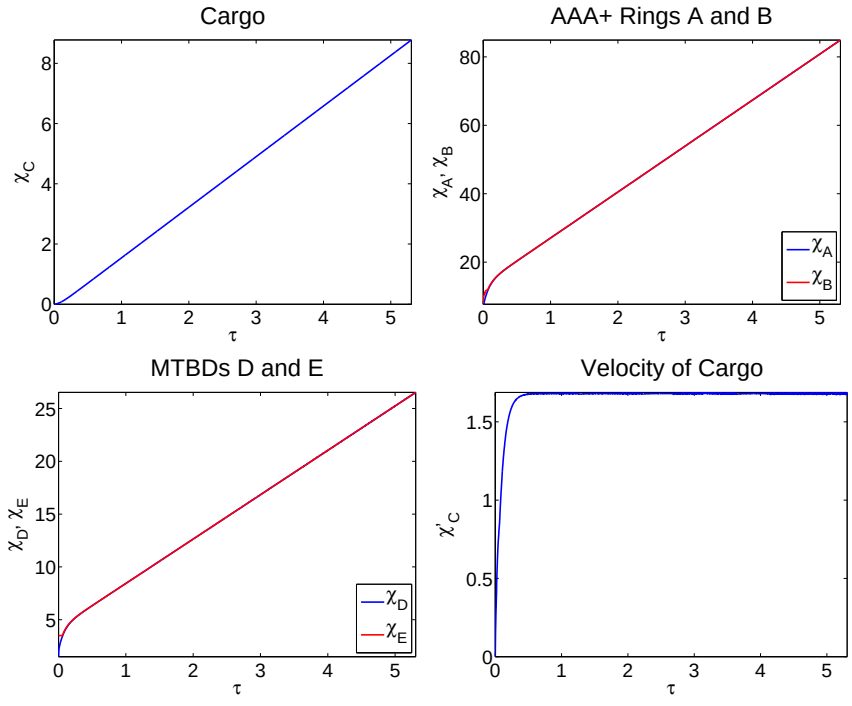

Figure 4.15: Plots of the numerical solutions to the model system with functions as defined in equations (4.33) - (4.36) where we take parameters to be at their primary values as given in Table 3.1, in particular $H = 10$ and $L_C = 10$, giving $\beta = 1$. See Section 3.5 for details of the numerical method. The cargo moves progressively along the microtubule with velocity that tend towards being constant over time. The two AAA+ rings, and the two MTBDs, follow the same trajectory after the initial time period, not exhibiting either a hand-over-hand profile or shuffling profile.

4.5 ATP force location

In the model we have assumed that the ATP force produced by the AAA+ ring acts on the ring itself, however models in the literature suggest that the force could act by swinging the MTBD forward [29]. Therefore, we refine the model by allowing the force associated with ATP to act on the MTBD instead of the AAA+ ring. The model equations are derived as in Chapter 3, however the forces $F_A(\mathbf{x}, t)$ and $F_B(\mathbf{x}, t)$ are now associated with the equations of motion of MTBDs D and E respectively. Therefore, the model system becomes:

$$\frac{d\chi_C}{d\tau} + 2\chi_C = b_1(\chi_A + \chi_B) - 2, \tag{4.37}$$

$$a_2\frac{d\chi_A}{d\tau} + \chi_A = b_2\chi_C + c_2\chi_D + b_2, \tag{4.38}$$

$$a_2\frac{d\chi_B}{d\tau} + \chi_B = b_2\chi_C + c_2\chi_E + b_2, \tag{4.39}$$

$$a_4\frac{d\chi_D}{d\tau} + \chi_D = \bar{F}_A(\chi, \tau) + \bar{g}_D(\chi, \tau) + b_4\chi_A, \tag{4.40}$$

$$a_4\frac{d\chi_E}{d\tau} + \chi_E = \bar{F}_B(\chi, \tau) + \bar{g}_E(\chi, \tau) + b_4\chi_B. \tag{4.41}$$

We study this adapted model using the same functions within our previous analysis, first using the trigonometric functions described by equations (4.6) - (4.9). Despite the change in location of the ATP force, we achieved remarkably similar results to our previous model, with qualitatively the same profiles for all components of the complex (see Figure 4.16). This result would suggest that the specifics of the ATP cycle may not have a significant impact on dynein's stepping ability. For example, an ATP force that acts on the AAA+ ring could reflect a scenario where the MTBD is still bound to the microtubule and hence the conformational change swings the AAA+ ring forwards before the head detaches. Whereas, an ATP force that acts on the MTBD would suggest that it is this component that swings forwards under the conformational change. This might be biologically useful, for example if the MTBD cannot detach immediately.

For the delta functions, as described by equations (4.29) - (4.32), slightly different profiles are achieved when compared to previous results (see Figure 4.17). The MTBDs and AAA+ rings followed clearly separate trajectories, with one head domain consistently behind the other. The velocity profile is also less oscillatory. These profiles vary greatly from experimental observations and so these types of functions are not suitable to model these forces.

We also considered the heavy-side functions as previously described by equations (4.33) - (4.36). The results of these simulations give the same profiles as previous results; the cargo moves forwards with an initially increasing velocity profile which then settles to a constant (see Figure 4.18).

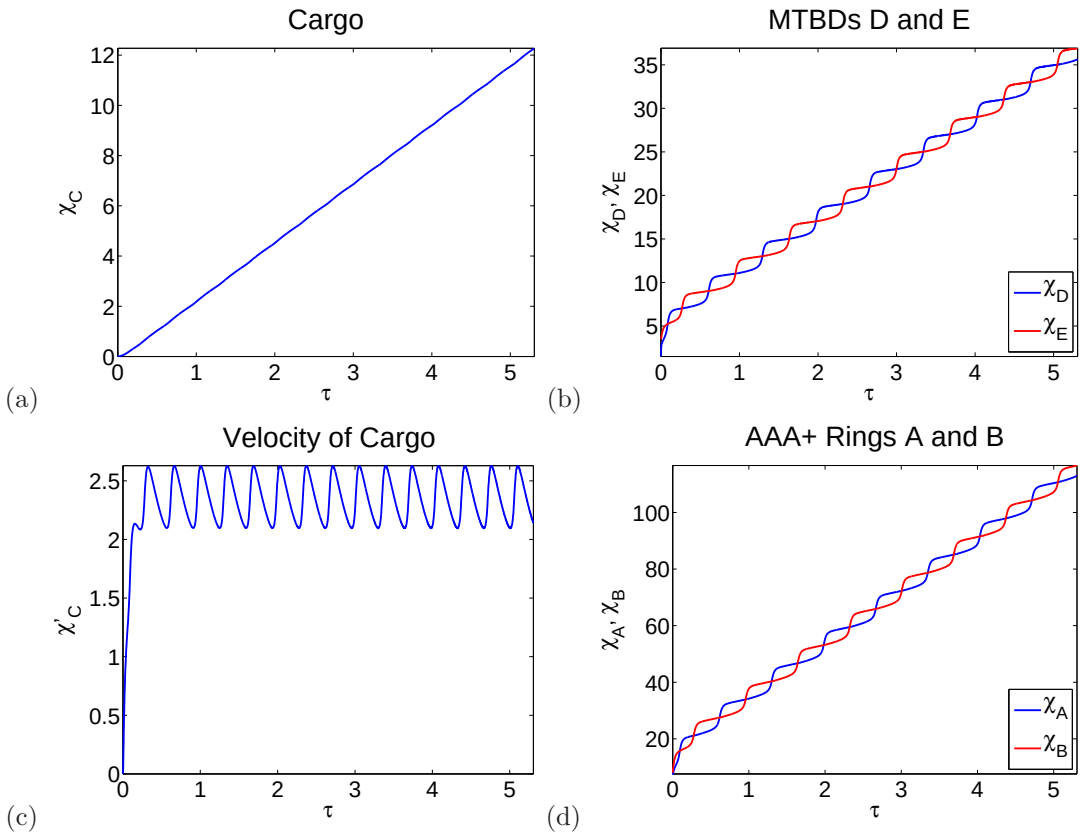

Figure 4.16: Numerical solutions to the model system (4.37) - (4.41) with functions as defined in equations (4.6) - (4.9) where we take our parameters to be at their primary values as given in Table 3.1, in particular $H = 10$ and $L_C = 10$. See Section 3.5 for details of the numerical method. Plots over the whole time corresponding to (a) trajectory of the cargo, (b) velocity profile of the cargo, (c) trajectory of the AAA+ rings, and (d) trajectory of the MTBDs.

The MTBDs follow identical trajectories, as do the AAA+ rings. Again, this does not reflect experimental observations, suggesting that the forces are not suitable to model dynein stepping.

So far we have only considered spatially dependent functions however the ATP force may be better modelled by a time dependent function. We assume that the ATP cycle follows a regular cycle and hence can be modelled by a periodic function over time. For MTBD D we define:

$$F_A(t) = Hcos(\frac{2\pi}{P}t), \tag{4.42}$$

where P is the period of the ATP force. For MTBD E we assume that the timing of it's ATP cycle is highly coordinated with the other MTBD but shifted in time and hence we take:

$$F_B(t) = Hsin(\frac{2\pi}{P}t). \tag{4.43}$$

For the binding affinities we continue to use cosine spatial functions as defined in equations (4.6) and (4.7). The results for these functions were very similar with clear stepping patterns, however

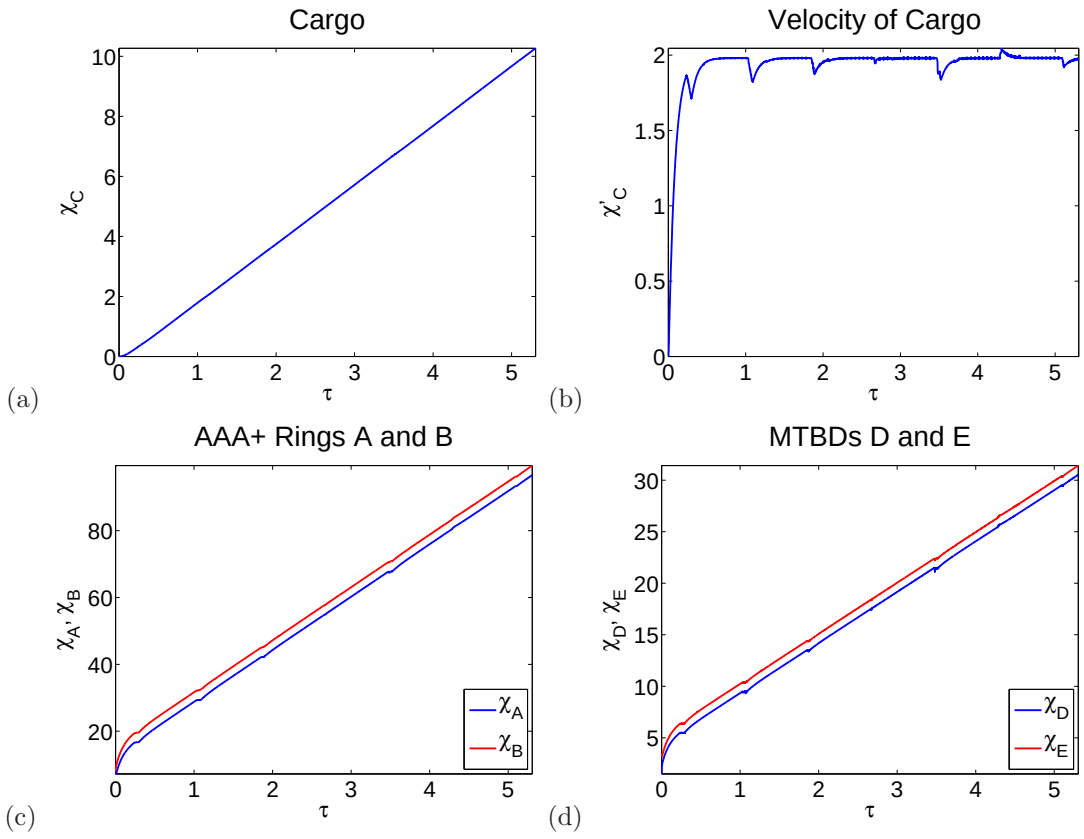

Figure 4.17: Numerical solutions to the model system (4.37) - (4.41) with functions as defined in equations (4.29) - (4.32) where we take our parameters to be at their primary values as given in Table 3.1, in particular $H = 10$ and $L_C = 10$. See Section 3.5 for details of the numerical method. Plots over the whole time corresponding to (a) trajectory of the cargo, (b) velocity profile of the cargo, (c) trajectory of the AAA+ rings, and (d) trajectory of the MTBDs.

they exhibited slightly more noise in each step (see Figure 4.19).

4.6 Multiple motor model

In vivo a cargo will be attached to multiple motors, with experimental observations reporting one to eight dyneins and one to five kinesins in various combinations [14, 21, 23]. To investigate the behaviour of multiple motors on a single cargo, the model is extended to include $N(t)$ dyneins attached to the cargo at time t whilst $F_C(t)$ represents a backward force from kinesin motors. For simplicity, it is assumed that each dynein motor moves identically and is attached to the same point on the cargo. Therefore the equation of motion for the cargo becomes:

$$m_C \frac{d^2x_C}{dt^2} = \underbrace{N(t)\Big[K_C(x_B - x_C - L_C\cos\theta_{BC}) - K_C(x_C - x_A - L_C\cos\theta_{AC})\Big]}_{\text{Force from } N(t) \text{ dynein complexes}} - F_C(t) - \gamma_C\frac{dx_C}{dt}, \tag{4.44}$$

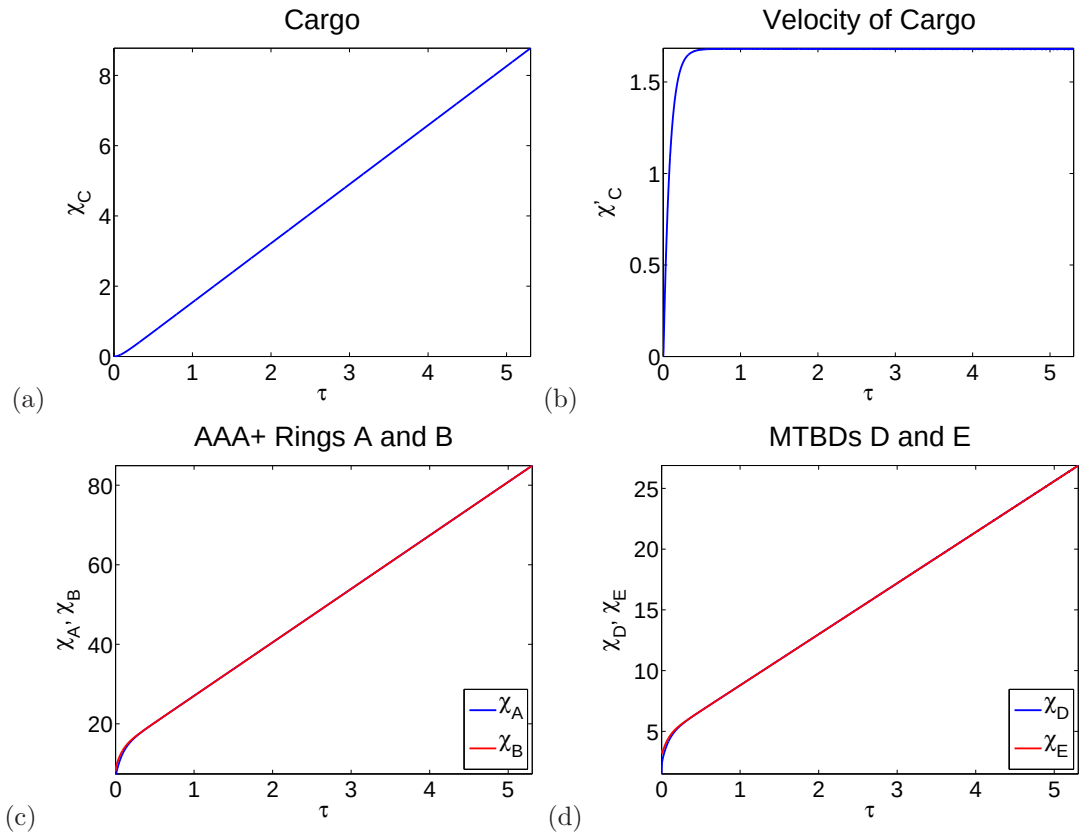

Figure 4.18: Numerical solutions to the model system (4.37) - (4.41) with functions as defined in equations (4.33) - (4.36) where we take our parameters to be at their primary values as given in Table 3.1, in particular $H = 10$ and $L_C = 10$. See Section 3.5 for details of the numerical method. Plots over the whole time corresponding to (a) trajectory of the cargo, (b) velocity profile of the cargo, (c) trajectory of the AAA+ rings, and (d) trajectory of the MTBDs.

where we obtain equation (3.3) when $N(t) = 1$. The AAA+ rings and MTBDs are modelled using the equations (3.4) - (3.7). Possible values for $N(t)$ are $N(t) = d$ where $1 \leq d \leq 8$ is a fixed constant [14, 21, 23], alternatively $N(t)$ corresponds to a function modelling the attachment to the cargo, where dynein motors can both attach and detach from the cargo. We have initially chosen to take $N(t)$ constant, and we see that increases in $N(t)$ lead to an increase in velocity (see Figure 4.20). We further consider a constant value for the external fore $F_C(t) = F_k$, by increasing this parameter we see that the velocity falls and eventually leads to backward motion (see Figure 4.21).

4.7 Discussion

Our results show a remarkable qualitative agreement with experimental observations. We can achieve desirable stepping patterns and specific behaviour through the use of particular functions and parameter values. We have shown that the stepping pattern can move from a hand-over-hand walking profile to a shuffling profile by changing a single parameter describing the relative strength

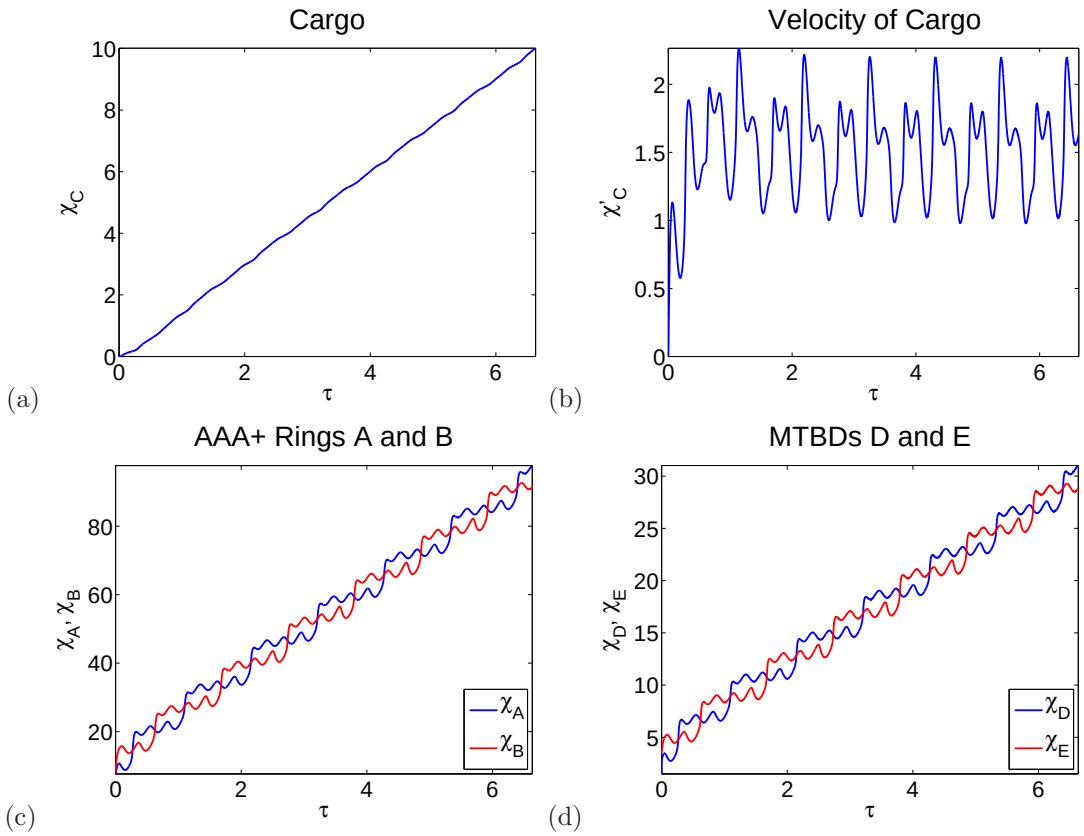

Figure 4.19: Numerical solutions to the model system (4.37) - (4.41) with functions as defined in equations (4.42) - (4.42) and (4.6) - (4.7) where we take $P = 1000$ and our parameters to be at their primary values as given in Table 3.1, in particular $H = 10$ and $L_C = 10$. See Section 3.5 for details of the numerical method. Plots over the whole time corresponding to (a) trajectory of the cargo, (b) velocity profile of the cargo, (c) trajectory of the AAA+ rings, and (d) trajectory of the MTBDs.

of the forces applied to each motor domain. Therefore, experimental observations into the relative ATP force produced by each motor, or the affinity to the microtubule would be beneficial to our model. Our model also makes the prediction that a dynein complex where one AAA+ ring has increased ATP activity or one MTBD has a stronger affinity to the microtubule will move with a shuffling profile, whilst if the ATP activity and affinity to the microtubule is equal within the complex, then it will step with a hand-over-hand profile.

We have seen that we can vary some model parameters to account for the effects of mutation, linking the resultant behaviour seen for cytoplasmic dynein to possible mechanistic causes by the mutation. Decreasing L_C and K_C is associated with a shorter natural length and lower spring constant of the tail section of dynein and lead to a reduced distance travelled by the cargo, through the effect on tension within the model. This reflects results found by Garrett *et al.,* Ori-McKenney *et al.,* and Sivagurunathan *et al.,* [2, 35, 36], who found a decrease in velocity and distance travelled for the *Loa* mutation which occurs in this section of dynein.

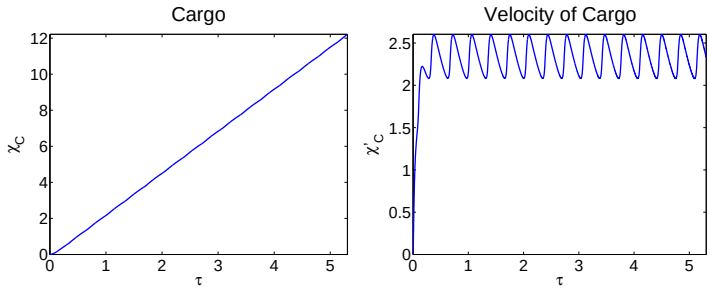

(a) $N(t) = 1$

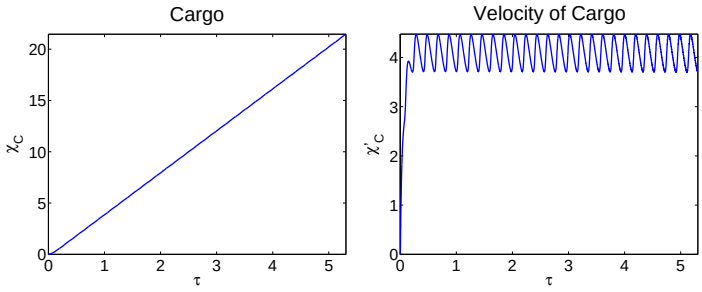

(b) $N(t) = 2$

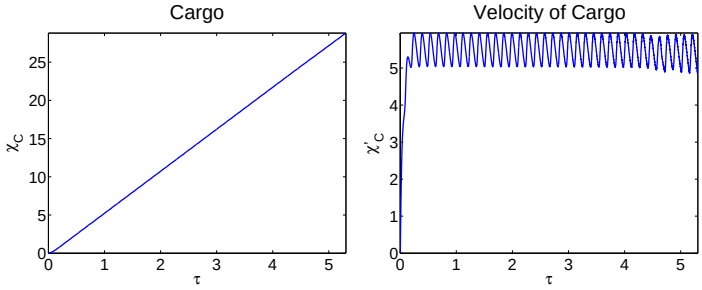

(c) $N(t) = 3$

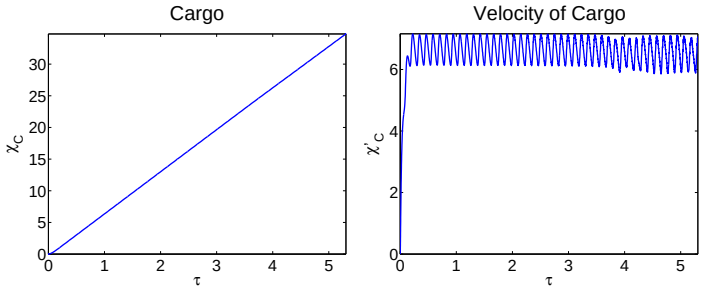

(d) $N(t) = 4$

Figure 4.20: Numerical solutions to the model system (4.44), (3.4) - (3.7) with functions as defined in equations (4.6) - (4.9) where we take our parameters to be at their primary values as given in Table 3.1, in particular $H = 10$ and $L_C = 10$. See Section 3.5 for details of the numerical method. Plots over the whole time corresponding to (a) trajectory of the cargo, and (b) velocity profile of the cargo. We set $F_C(t) = 0$ and vary $N(t)$.

A simple model of multiple motor transport has been studied, showing that an increase in the number of dynein motors leads to an increase in velocity of the cargo. This is to be expected as there are more dyneins to carry a large load. However, this simple model does not consider the implications of crowding or other restrictions which may limit gains in velocity, such as a

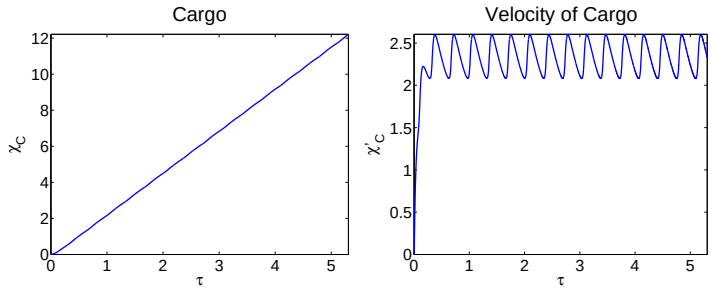

(a) $F_C(t) = 0$

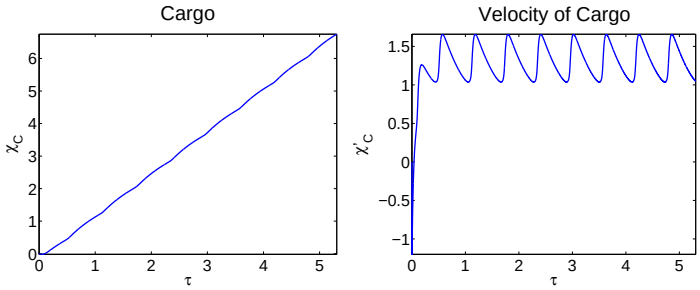

(b) $F_C(t) = 12$

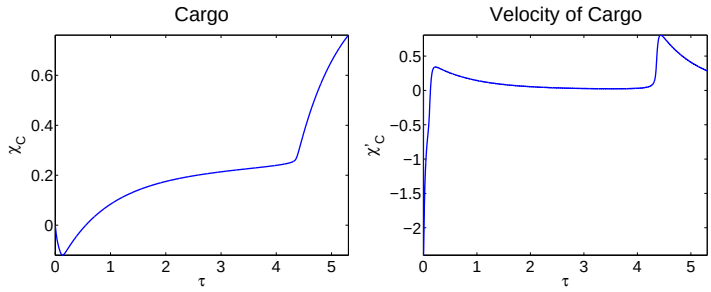

(c) $F_C(t) = 24$

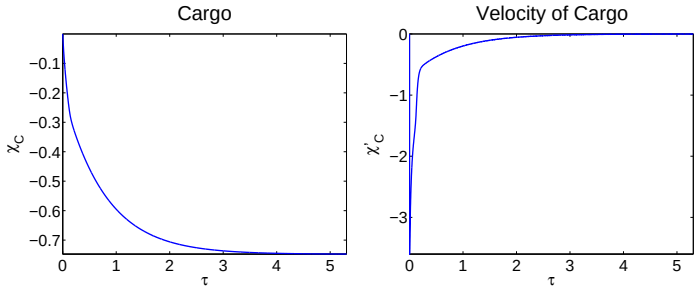

(d) $F_C(t) = 36$

Figure 4.21: Numerical solutions to the model system (4.44), (3.4) - (3.7) with functions as defined in equations (4.6) - (4.9) where we take our parameters to be at their primary values as given in Table 3.1, in particular $H = 10$ and $L_C = 10$. See Section 3.5 for details of the numerical method. Plots over the whole time corresponding to (a) trajectory of the cargo, and (b) velocity profile of the cargo. We set $N(t) = 1$ and vary $F_C(t)$.

lack of available binding sites or ATP which may actually slow the process down. Future work would need to consider how to implement these possibilities in the model, possibly by using a more sophisticated attachment function. Future investigations would also need to consider the evolving shape of the cargo in order to study fission and the effects of a tug of war.

This initial model is a simplification of dynein's stepping process, with limitations including the assumptions of continual stepping, a fixed step size and highly coordinated motion between the two head domains. In reality, the binding of ATP is a stochastic process and hence stochasticity would need to be introduced into the model in order to explore the stepping pattern of dynein further. This is introduced to the model in Part II, where variable step sizes and uncoordinated motion are also considered. The model has so far considered that the tail can be modelled as two springs connecting the AAA+ ring immediately to the cargo, however this may not be the most appropriate model and the tail may be more accurately modelled by introducing a mass and additional spring to model the connection to the cargo from the tail domain. This adaptation is also considered in the next chapter.

Part II

Stochastic Model

Chapter 5

Stochastic Mechanical Model with Fixed Step Size

5.1 Derivation of the stochastic model

So far we have modelled ATP hydrolysis as a continuous process, assuming that dynein steps continually with a fixed step size. However, in reality the binding of ATP to a dynein head domain is a random process. The model is therefore refined to include this stochastic process. The tail domain has been modelled as two springs directly connecting the AAA+ rings to the cargo, however this may not be the most suitable model. Hence, the model is adapted as follows: the tail domain is now modelled as two identical springs, from the AAA+ rings, connected to a sphere with small Reynolds number and constant mass. The flexible section of the linker is modelled as part of these springs. The binding between the tail and the cargo is modelled via another spring connecting the tail domain to the cargo. See Figure 5.1 for a schematic diagram illustrating the whole structure on which the mathematical model is based and Table 5.1 for a list of parameter values. We make four simplifying assumptions:

- The spring between the cargo and tail domain is parallel to the microtubule.
- The springs between the tail domain and AAA+ rings are at a fixed angle to the microtubule.
- The stalks are at a fixed angle to the microtubule.
- There are no external forces acting on the cargo, such as those from other motor proteins or an optical trap.

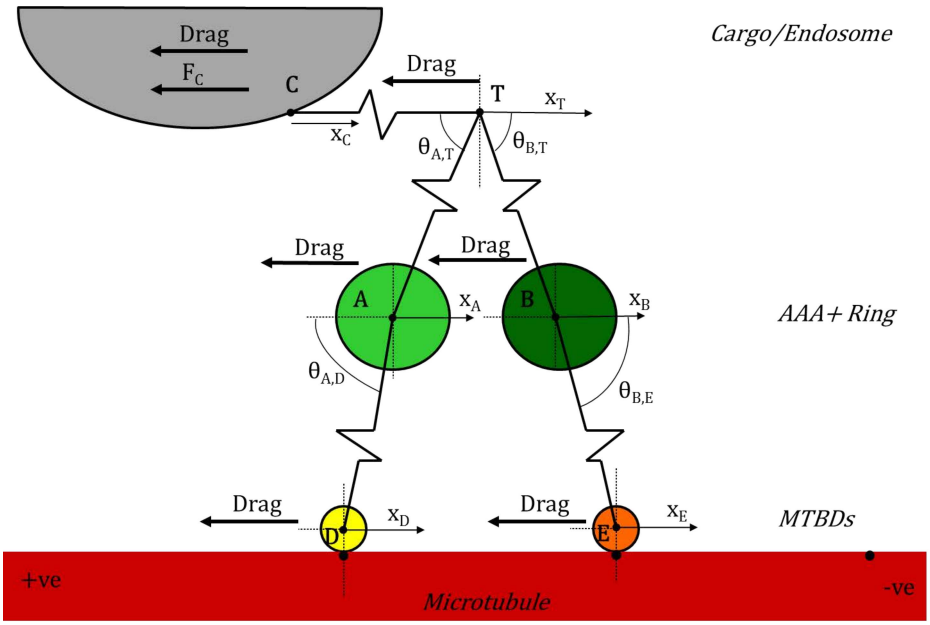

Figure 5.1: A schematic diagram of the mechanical model (adapted from [9]). The cargo is modelled as a sphere (grey) and regulators of binding to dynein are modelled as part of this cargo. The binding of the cargo to the tail domain is modelled by a spring. The tail of dynein is modelled by a sphere connected by two springs to the AAA+ rings. The AAA+ rings, depicted in green, and the MTBDs, depicted in yellow and orange, are modelled as spheres. The stalks are modelled as springs. The microtubule is modelled as a line (red).

Variable angles are briefly explored in Section 5.5.

Remark 5.1.1. We continue to assume that both of the motor domains in the dynein dimer are identical and so can be modelled using the same parameter values, given in Table 5.1. However, this may not be the case, for example leading and lagging heads may have different properties [31, 32], and DeWitt *et al.,* consider a dynein heterodimer in which one head domain is wild type and one is mutated [31]. This is explored in Section 5.6.

We derive from first principles a system of six second order non-linear ordinary differential equations to model the transport mechanisms of a single dynein acting on a cargo. Let $x_C(t)$, $x_T(t)$, $x_A(t)$, $x_B(t)$, $x_D(t)$ and $x_E(t)$ denote the positions of the cargo, tail, AAA+ rings A and B, and the MTBDs D and E, respectively, at time $t \in [0, T_{Final}]$ for some end time $T_{Final} > 0$. The coordinates x_A and x_D represent one head domain of dynein with the coordinates x_B and x_E representing the other (see Figure 5.1). We continue to model the microtubule as a one-dimensional line with binding sites 8nm apart; we only consider motion along this line. Using Newton's second law we study the net forces acting on the system. For the cargo there is a spring force, viscous drag and an external force acting on it. By Hooke's law we take the spring force to be:

$$F_{Spring}(t) = K_C\Big(x_T(t) - x_C(t) - L_C\Big),$$

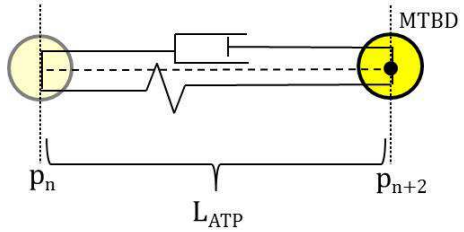

Figure 5.2: A schematic diagram of the dashpot-spring model for the conformational change in dynein resulting from the binding of ATP. For the time interval $[t_i, t_{i+1}]$ the MTBD is at the binding site p_n at time t_i and moves to the binding site p_{n+2} by time t_{i+1} with a step size of L_{ATP}.

where K_C is the spring constant and L_C is the natural length. We obtain the viscous drag by Stokes' law:

$$F_{Drag}(t) = \gamma_C \frac{dx_C}{dt},$$

where the damping coefficient $\gamma_C = 6\pi\eta R_C$ with η the viscosity and R_C the radius of the cargo. For completeness we include an external force F_C that is exerted on the cargo, although throughout the model this is assumed to equal zero. Therefore, the equation of motion for the cargo can be modelled by:

$$m_C \frac{d^2x_C}{dt^2} = K_C\Big(x_T - x_C - L_C\Big) - F_C - \gamma_C \frac{dx_C}{dt}.$$

The equations of motion for the tail domain and AAA+ rings can be derived similarly. Therefore we obtain the following system of ordinary differential equations for the cargo, tail and AAA+ rings respectively:

$$\begin{aligned}
m_C \frac{d^2x_C}{dt^2} &= K_C\Big(x_T - x_C - L_C\Big) - F_C - \gamma_C \frac{dx_C}{dt},\\
m_T \frac{d^2x_T}{dt^2} &= K_T\Big(x_B - x_T - L_T\cos(\theta_{BT})\Big) - K_T\Big(x_T - x_A - L_T\cos(\theta_{AT})\Big)\\
&\quad - K_C\Big(x_T - x_C - L_C\Big) - \gamma_T \frac{dx_T}{dt},\\
m_M \frac{d^2x_A}{dt^2} &= K_T\Big(x_T - x_A - L_T\cos(\theta_{AT})\Big) - K_S\Big(x_A - x_D - L_S\cos(\theta_{AD})\Big) - \gamma_M \frac{dx_A}{dt},\\
m_M \frac{d^2x_B}{dt^2} &= K_S\Big(x_E - x_B - L_S\cos(\theta_{BE})\Big) - K_T\Big(x_B - x_T - L_T\cos(\theta_{BT})\Big) - \gamma_M \frac{dx_B}{dt}.
\end{aligned}$$

We wish to model the mechanics of ATP hydrolysis on the motor domain of dynein. The binding of ATP occurs randomly and is followed by microtubule release of the corresponding MTBD and a recovery stroke towards the next binding site [28, 29]. Hence, we will assume that there are two MTBD states:

- Bound: This is defined to be when the MTBD is bound to the microtubule and hence is

stationary.

- Unbound: Defined to be when the MTBD is unbound from the microtubule and undergoing the recovery stroke towards the next binding site.

It is hypothesized that ATP hydrolysis induces a conformational change in dynein, potentially causing a 37° kink in the stalk and swinging the MTBD forwards [26, 29]. Hence, for the unbound state the conformational change is modelled by a dashpot and spring acting solely on the MTBD (see Figure 5.2) [156]. It is assumed that this force is independent of the particular interval on the microtubule, defined by $x \in [p_j(t), p_{j+1}(t)]$ and it is also assumed to be identical for the two head domains. Binding sites are taken to be 8nm apart on the microtubule with each MTBD binding to distinct binding sites, given a step size of nL_{ATP}. The current model is one dimensional and hence it is assumed that this force acts only in the horizontal direction. The force produced by the dashpot is proportional to the velocity and the spring force is proportional to the displacement, hence

$$F_{ATP}(x(t)) = -\gamma_{ATP}\frac{dx}{dt} + K_{ATP}(nL_{ATP} - (x(t) - x(0))),$$

where γ_{ATP} and K_{ATP} are parameters determining the size of the ATP force, with estimated values given in Table 5.1. The term nL_{ATP} represents the unstressed length of the spring and is taken to be the step size of the head domain, with L_{ATP} the distance between binding sites and n a parameter reflecting the magnitude and direction of the step. If MTBD D is in an unbound state and MTBD E is in a bound state, then the equations of motion can be shown to be given by

$$\begin{aligned} m_S\frac{d^2x_D}{dt^2} &= -\gamma_{ATP}\frac{dx_D}{dt} - K_{ATP}(x_D - p_j - nL_{ATP}) - \gamma_S\frac{dx_D}{dt} - K_S(x_D - x_A + L_S\cos(\theta_{AD})), \\ \frac{dx_E}{dt} &= 0, \end{aligned}$$

for $t \in [t_i, t_{i+1}]$ for $i \in \mathbb{N}$ such that $0 \leq t_i < t_{i+1}$, where p_j with $j \in \mathbb{N}_0$ is the binding site that MTBD D was bound to at time $t = t_i$. The equations are similar for when MTBD E is in an unbound state and MTBD D is in the bound state:

$$\begin{aligned} \frac{dx_D}{dt} &= 0, \\ m_S\frac{d^2x_E}{dt^2} &= -\gamma_{ATP}\frac{dx_E}{dt} - K_{ATP}(x_E - p_{j+1} - nL_{ATP}) - \gamma_S\frac{dx_E}{dt} - K_S(x_E - x_B - L_S\cos(\theta_{BE})), \end{aligned}$$

again for $t \in [t_i, t_{i+1}]$ and where p_{j+1} with $j \in \mathbb{N}_0$ is the binding site that MTBD E was bound to at time $t = t_i$. Here, we are assuming some inherent coordination between the two MTBDs to keep the motor attached to the microtubule as one motor is unable to bind ATP whilst the other is detached. The MTBDs are assumed to become unbound once the corresponding AAA+ ring

Parameter	Description	Value	Ref.
M_C	Mass of the cargo	2MDa	Estimated [159]
M_T	Mass of the tail component	0.14MDa	Estimated [2]
M_M	Mass of the AAA+ ring	0.5MDa	Estimated [37]
M_S	Mass of the MTBD	0.03MDa	Estimated [37]
R_C	Radius of the cargo	460nm	[66]
R_T	Radius of the tail domain	3nm	[55]
R_M	Radius of the AAA+ ring	6.5nm	[55, 59]
R_S	Radius of the MTBD	1.5nm	[59]
L_C	Unstressed length between the cargo and tail	12nm	[55]
L_T	Unstressed length between the AAA+ ring and tail	8nm	[55]
L_S	Unstressed length between the AAA+ ring and MTBD	15nm	[55]
K_C	Spring constant between the cargo and the tail	1MDa ns^{-2}	Estimated
K_T	Spring constant between the tail and the AAA+ ring	1MDa ns^{-2}	Estimated
K_S	Spring constant between the AAA+ ring and the MTBD	10MDa ns^{-2}	Estimated
η	Viscosity of the cytoplasm	1.2MDa nm^{-1} ns^{-1}	[163]
L_{ATP}	Approximated ATP force: unstressed length between the binding sites	8nm	Estimated
K_{ATP}	Approximated ATP force: spring constant	10MDa ns^{-2}	Estimated
γ_{ATP}	Approximated ATP force: drag coefficient	10MDa ns^{-2}	Estimated
$\theta_{A,D}$	Angle of the stalk between AAA+ ring A and MTBD D	53°	[55]
$\theta_{B,E}$	Angle of the stalk between AAA+ ring B and MTBD E	53°	[55]
$\theta_{A,T}$	Angle of the spring between AAA+ ring A and the tail domain	33°	[55]
$\theta_{B,T}$	Angle of the spring between AAA+ ring B and the tail domain	33°	[55]

Table 5.1: Dimensional parameters and the primary values used in the mathematical model system (5.4) - (5.9).

binds ATP. This occurs randomly and the transition between states is explained below in Section 5.2.

We prescribe initial conditions as follows: MTBD D and E are taken to be at binding sites p_0 and $p_1 = p_0 + 8$ respectively. The cargo is taken to be at the origin and the tail component is set to be at its natural length L_C from the cargo. The AAA+ rings are taken to be at the same point midway between the MTBDs, at a distance of the natural length L_T from the tail. Therefore, the initial conditions are set to be

$$x_C(0) = 0,\ x_T(0) = L_C,\ x_A(0) = L_C + L_T,\ x_B(0) = L_C + L_T,$$
$$x_D(0) = p_0 = L_C + L_T - 4,\ x_E(0) = p_1 = L_C + L_T + 4.$$

5.2 Stochastic stepping

First, we study a simple model of continual forward stepping with a fixed step size. The predominant step size given in the literature is 16nm [30], and the displacement of the MTBD under a conformational change during the ATP cycle has been suggested to be close to this step size [55]; hence we fix $n = 2$. Binding sites are taken to be p_{2k} for MTBD D and p_{2k+1} for MTBD E with $k = 0, 1, 2, ...$ and $p_{2k+1} - p_{2k} = 8$, binding sites are 8nm apart on the microtubule, corresponding to the length of the tubulin heterodimers that form the microtubule [160], with each MTBD binding to distinct binding sites that are 16nm apart.

To model the continual stepping by dynein over a microtubule, stochasticity is introduced to the model via the randomness in which an AAA+ ring binds ATP and hence a MTBD becomes unbound. Let the probability that MTBD E steps given that MTBD D stepped previously be given by $\Pr(E_{i+1} \mid D_i) = P_D$ for step $i \in \mathbb{N}$; hence $\Pr(D_{i+1} \mid D_i) = 1 - P_D$ as the complement is given by $E_{i+1}^C = D_{i+1}$. Similarly, let the probability that MTBD E steps given that MTBD E stepped previously be given by $\Pr(E_{i+1} \mid E_i) = P_E$; hence $\Pr(D_{i+1} \mid E_i) = 1 - P_E$. Given that $E_i^C = D_i$ the following equation must be satisfied:

$$\Pr(D_i \mid E_{i+1}) + \Pr(E_i \mid E_{i+1}) = 1.$$

Then by applying Bayes' Theorem we obtain:

$$\frac{\Pr(E_{i+1} \mid D_i)\Pr(D_i)}{\Pr(E_{i+1})} + \frac{\Pr(E_{i+1} \mid E_i)\Pr(E_i)}{\Pr(E_{i+1})} = 1. \tag{5.1}$$

We assume that the probability that a MTBD steps does not change over time, hence $\Pr(E_{i+1}) = \Pr(E_i)\ \forall i \in \mathbb{N}$, and similarly $\Pr(D_{i+1}) = \Pr(D_i)\ \forall i \in \mathbb{N}$. We also make the further assumption that, given no information about the previous step, both MTBDs are equally likely to step, hence $\Pr(E_i) = \Pr(D_i) = 0.5$ for $i \in \mathbb{N}$. Thus equation (5.1) simplifies to:

$$\Pr(E_{i+1} \mid D_i) + \Pr(E_{i+1} \mid E_i) = 1.$$

Therefore, our parameters P_D and P_E satisfy $P_D + P_E = 1$.

Consider $t \in [0, T_{Final}]$ with $T_{Final} > 0$ and $t_i = t_{i-1} + \frac{T_{Final}}{N}$ for $i = 1, 2, ..., N$. Let $\mathbf{q} = \{q_i\}_{i=1:N}$ be a random vector where q_i is from the uniform distribution on $(0, 1)$. We assign the value d to be the maximum separation distance that can occur between the MTBDs. If the maximum separation between the MTBDs has been exceeded then it is assumed that the rearward

head steps; else, given that MTBD j stepped previously, if $q_i < P_j$ then MTBD E is set to be in the unbound state (i.e. unbound from the microtubule and undergoing the recovery stroke) and MTBD D is set to be in the bound state (i.e. bound to the microtubule). Otherwise we assume that the MTBD D is in the unbound state and MTBD E in the bound state. Hence, we can define a step-function h_E given by

$$h_E(t, x_D, x_E, d) = \begin{cases} 1 & \text{if} \quad x_D - x_E > d \quad \text{or if} \quad (q_i < P_j \quad \text{and} \quad x_E - x_D \leq d), \\ 0 & \text{otherwise;} \end{cases} \tag{5.2}$$

where MTBD j stepped previously and similarly

$$h_D(t, x_D, x_E, d) = 1 - h_E(t, x_D, x_E, d), \tag{5.3}$$

for $t \in [t_i, t_{i+1}]$ with $i = 1, 2, ..., N$. This does assume some coordination between the two head domains of dynein as only one head will step during each time interval, but it does not enforce coordination of the stepping pattern itself if the head domains are allowed to separate past consecutive binding sites. The rearward head always steps if the two head domains become too far apart. This is used in order to ensure that the two head domains cannot diverge away from each other which would be biologically unrealistic. The system of ODEs is therefore given by:

$$m_C \frac{d^2 x_C}{dt^2} = K_C\Big(x_T - x_C - L_C\Big) - F_C - \gamma_C \frac{dx_C}{dt}, \tag{5.4}$$

$$\begin{aligned} m_T \frac{d^2 x_T}{dt^2} = {} & K_T\Big(x_B - x_T - L_T \cos(\theta_{BT})\Big) - K_T\Big(x_T - x_A - L_T \cos(\theta_{AT})\Big) \\ & - K_C\Big(x_T - x_C - L_C\Big) - \gamma_T \frac{dx_T}{dt}, \end{aligned} \tag{5.5}$$

$$m_M \frac{d^2 x_A}{dt^2} = K_T\Big(x_T - x_A - L_T \cos(\theta_{AT})\Big) - K_S\Big(x_A - x_D - L_S \cos(\theta_{AD})\Big) - \gamma_M \frac{dx_A}{dt}, \tag{5.6}$$

$$m_M \frac{d^2 x_B}{dt^2} = K_S\Big(x_E - x_B - L_S \cos(\theta_{BE})\Big) - K_T\Big(x_B - x_T - L_T \cos(\theta_{BT})\Big) - \gamma_M \frac{dx_B}{dt}, \tag{5.7}$$

$$\begin{aligned} m_S h_D(t, x_D, x_E, d) \frac{d^2 x_D}{dt^2} = {} & h_D(t, x_D, x_E, d)\Big[- \gamma_{ATP} \frac{dx_D}{dt} - K_{ATP}(x_D - p_i - 2L_{ATP}) \\ & - K_S(x_D - x_A + L_S \cos(\theta_{AD}))\Big] - \gamma_S \frac{dx_D}{dt}, \end{aligned} \tag{5.8}$$

$$\begin{aligned} m_S h_E(t, x_D, x_E, d) \frac{d^2 x_E}{dt^2} = {} & h_E(t, x_D, x_E, d)\Big[- \gamma_{ATP} \frac{dx_E}{dt} - K_{ATP}(x_E - p_{i+1} - 2L_{ATP}) \\ & - K_S(x_E - x_B - L_S \cos(\theta_{BE}))\Big] - \gamma_S \frac{dx_E}{dt}, \end{aligned} \tag{5.9}$$

for $t \in [0, T_{Final}]$.

Remark 5.2.1. In this refined model we only consider continual stepping therefore we fix the size of the time interval for each step $T_{Step} = t_{i+1} - t_i$ and hence T_{Final} will depend on the time interval T_{Step} and the number of steps N. Therefore, the stepping rate of the motors is predetermined.

Variable dwell times between steps will be considered in Chapters 6 and 7.

Remark 5.2.2. The binding sites are predetermined. The initial binding site p_0 is assigned a value and all binding sites are taken to be 8nm away from the previous binding site. For each time step, the binding site is updated by taking the next binding site of the unbound MTBD. For example, if a MTBD is unbound on $[t_i, t_{i+1}]$ and bound to p_j at time $t = t_i$, then the binding site will be updated to $p_{j+2} = p_j + nL_{ATP}$ for $t = t_{i+1}$.

5.2.1 Non-dimensionalisation

To nondimensionalise the model let $x_C = L_C\chi_C$, $x_T = L_T\chi_T$, $x_A = L_S\chi_A$, $x_B = L_S\chi_B$, $x_D = L_S\chi_D$, $x_E = L_S\chi_E$ and $t = \frac{m_C}{\gamma_C}\tau$. We assume that the acceleration terms are small and that the dynamics are dominated by the viscous drag. Hence, the second derivatives are neglected to obtain the following non-dimensional system:

$$\alpha_C\frac{d\chi_C}{d\tau} = \Big(\frac{1}{\rho_1}\chi_T - 1\Big) - \lambda - \chi_C, \tag{5.10}$$

$$\alpha_T\frac{d\chi_T}{d\tau} = \Big(\frac{1}{\rho_2}(\chi_B + \chi_A) - \cos(\theta_{BT}) + \cos(\theta_{AT})\Big) + \rho_1\kappa_1(\chi_C + 1) - (2 + \kappa_1)\chi_T, \tag{5.11}$$

$$\alpha_M\frac{d\chi_A}{d\tau} = \rho_2\kappa_2\Big(\chi_T - \cos(\theta_{AT})\Big) + \Big(\chi_D + \cos(\theta_{AD})\Big) - (\kappa_2 + 1)\chi_A, \tag{5.12}$$

$$\alpha_M\frac{d\chi_B}{d\tau} = \Big(\chi_E - \cos(\theta_{BE})\Big) + \rho_2\kappa_2\Big(\chi_B + \cos(\theta_{BT})\Big) - (\kappa_2 + 1)\chi_B, \tag{5.13}$$

$$\begin{aligned}\Big(\alpha_S + \alpha_{ATP}h_D(\tau, \chi_D, \chi_E, \delta)\Big)\frac{d\chi_D}{d\tau} = h_D(\tau, \chi_D, \chi_E, \delta)\Big[\kappa_3(\beta_i + 2\rho_3) \\ + \Big(\chi_A - \cos(\theta_{AD})\Big) - (1 + \kappa_3)\chi_D\Big],\end{aligned} \tag{5.14}$$

$$\begin{aligned}\Big(\alpha_S + \alpha_{ATP}h_E(\tau, \chi_D, \chi_E, \delta)\Big)\frac{d\chi_E}{d\tau} = h_E(\tau, \chi_D, \chi_E, \delta)\Big[\kappa_3(\beta_{i+1} + 2\rho_3) \\ + \Big(\chi_B + \cos(\theta_{BE})\Big) - (1 + \kappa_3)\chi_E\Big].\end{aligned} \tag{5.15}$$

The nondimensional parameters are given by

$$\begin{aligned}&\alpha_C = \frac{\gamma_C\gamma_C}{m_CK_C}, \quad \alpha_T = \frac{\gamma_T\gamma_C}{m_CK_T}, \quad \alpha_M = \frac{\gamma_M\gamma_C}{m_CK_S}, \quad \alpha_S = \frac{\gamma_S\gamma_C}{m_CK_S}, \quad \alpha_{ATP} = \frac{\gamma_{ATP}\gamma_C}{m_CK_S},\\
&\rho_1 = \frac{L_C}{L_T}, \quad \rho_2 = \frac{L_T}{L_S}, \quad \rho_3 = \frac{L_{ATP}}{L_S},\\
&\kappa_1 = \frac{K_C}{K_T}, \quad \kappa_2 = \frac{K_T}{K_S}, \quad \kappa_3 = \frac{K_{ATP}}{K_S},\\
&\beta_i = \frac{p_i}{L_S}, \quad \lambda = \frac{F_C}{K_CL_C}, \quad \delta = \frac{d}{L_S}.\end{aligned}$$

See Table 5.1 for dimensional parameter values. The nondimensional initial conditions are given by:

$$\chi_C(0) = 0, \quad \chi_T(0) = \rho_1, \quad \chi_A(0) = \rho_2 + \rho_1\rho_2, \quad \chi_B(0) = \rho_2 + \rho_1\rho_2,$$
$$\chi_D(0) = \beta_0, \quad \text{and} \quad \chi_E(0) = \beta_1. \tag{5.16}$$

5.3 Numerical experiments

The scheme is implemented in MATLAB for N intervals of $[0, \tau_{Final}]$ with $\tau_{Final} = 10^8$ and $N = 100$ using the solver *ode45* [164]. The initial conditions are given by equations (5.16). For the initial step it is assumed that MTBD D is in an unbound state and MTBD E is in a bound state. For each following step a random number q_i is generated from the uniform distribution on $(0, 1)$ to determine which head steps (see equation (5.2)) and the initial conditions are given by the values from the previous simulation: $\chi_C(\tau_i)$, $\chi_T(\tau_i)$, $\chi_A(\tau_i)$, $\chi_B(\tau_i)$, $\chi_D(\tau_i)$ and $\chi_E(\tau_i)$.

5.3.1 Stochastic stepping with limited coordination

Initially we assume that the motor domains bind ATP at random when they are both attached to the microtubule, therefore we take $P_D = P_E = 50\%$. The primary value of the maximum separation distance is taken to be $d = 48$nm. The results show a mixed stepping pattern for both the MTBDs and AAA+ rings with both shuffling and hand-over-hand patterns present (Figure 5.3(e) and (f)). This matches experimental observations on yeast cytoplasmic dynein, labelled at the AAA+ rings [31, 32]. Here, we are able to compare the trajectories of AAA+ ring and MTBDs which is not yet achievable in experiments as tagging functional MTBDs is technically challenging. The tail domain also moves with a stepping profile, as seen in experiments on dynein labelled at the tail domain (Figure 5.3(c) and (d)). The cargo moves along the microtubule with increasing velocity and oscillatory profile (Figure 5.3(a) and (b)). By computing the simulations over a larger interval, with end time $\tau_{Final} = 10^9$ and $N = 1000$, the velocity of the cargo reaches a relative plateau, where it stops increasing over time and oscillates within a small band (see Figure 5.4 (a) and (b)) matching observations by Garrett *et. al* [2].

In order to make statistical comparisons with experimental observations, we compiled data from 100 simulations of the model, extending this to 1000 simulations for optimum parameter values. Observations by Qiu *et al.* [32] show that approximately 83% of steps did not pass each other and

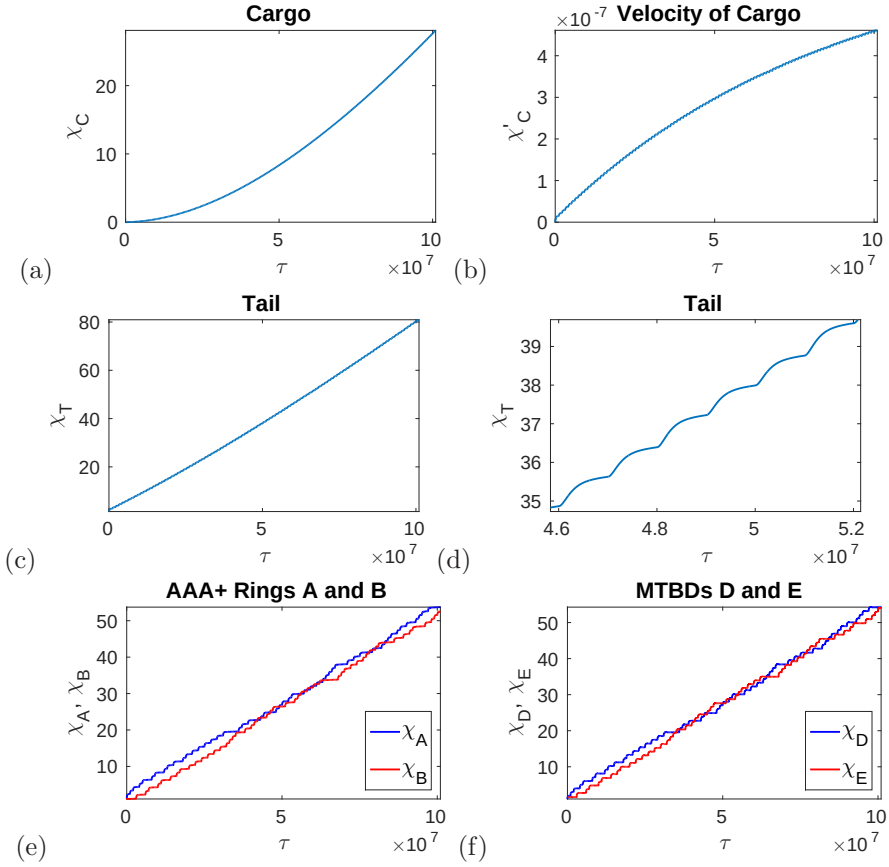

Figure 5.3: Numerical solutions to the model equations (5.10) - (5.15) with maximum separation distance between MTBDs at 48nm and the probability that MTBD E steps at 50%. Plots over the whole time corresponding to (a) trajectory of the cargo, (b) velocity profile of the cargo, (c) trajectory of the tail domain, (d) trajectory of the tail domain for a representative subinterval, (e) trajectory of the AAA+ rings, and (f) trajectory of the MTBDs.

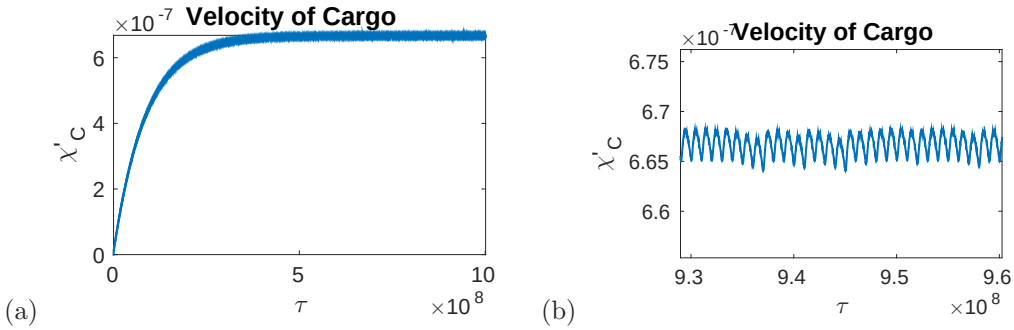

Figure 5.4: Numerical solutions to the model equations (5.10) - (5.15) with maximum separation distance between MTBDs at 48nm and the probability that MTBD E steps at 50%, with end time $\tau_{Final} = 10^9$ and $N = 1000$. (a) Velocity profile of the cargo for $\tau \in [0, 10^9]$. (b) Velocity profile of the cargo for a representative subinterval illustrating the long-time dynamics of the cargo.

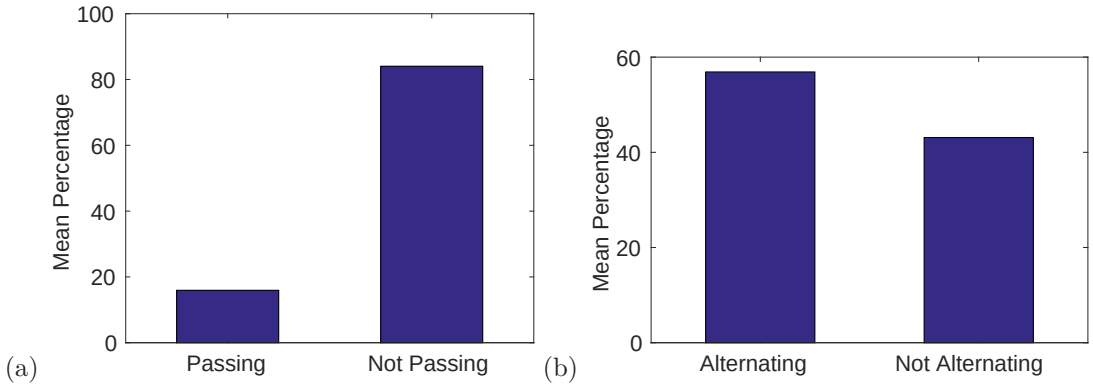

Figure 5.5: Bar charts showing the mean percentage of steps: (a) passing vs not passing and (b) alternating vs not alternating. The data represents the results of 1000 simulations with the probability that MTBD E steps set at 50% and the maximum separation distance set to be 48nm.

d	% Not Passing Steps	% Alternating Steps
8	49.45	75.36
16	65.68	66.24
24	73.08	61.65
32	79.17	60.43
40	83.66	57.25
48	84.70	57.20
56	86.21	55.38
64	87.13	54.68

Table 5.2: Mean percentage of not passing steps and alternating steps given a range of values for the maximum separation distance d. The data represents the results of 100 simulations with the probability that MTBD E steps set at 50%. If x% of steps are not passing then $1-x$% of steps are passing. Similarly, if x% of steps are alternating then $1-x$% of steps are not alternating.

in our simulations we have an average of 84.05% steps not passing (see Figure 5.5(a)). However, experimental results also show that dynein moves with predominately an alternating stepping pattern with approximately 74% of steps alternating in time [32], whereas our simulations show only 56.89% of steps alternating in time (see Figure 5.5(b)). This may be due to the randomness in the model where the probability of stepping is independent of which head stepped previously.

Remark 5.3.1. The choice of 48nm for the maximum separation distance gives the optimum proportion of non-passing steps. Lower values increase the prevalence of passing steps and higher values allow the components of the complex to diverge which may not be physically realistic, see Table 5.2.

Remark 5.3.2. Many experiments on cytoplasmic dynein, including the experiments by DeWitt *et al.,* and Qiu *et al.,* [31, 32], use dimerized yeast dynein. We have therefore also looked at a reduced version of the model for a dimerized dynein motor with no cargo and we get similar results for the stepping pattern and trajectories (see Section 5.4 for results).

P_D	P_E	% Not Passing Steps	% Alternating Steps
0	100	85.15	14.00
10	90	85.25	22.52
20	80	85.14	31.43
30	70	85.21	40.19
40	60	84.45	49.65
50	50	83.51	55.98
60	40	83.94	65.93
70	30	81.45	74.15
80	20	81.85	82.16
90	10	75.76	91.25
100	0	100	100

Table 5.3: Mean percentage of not passing steps and alternating steps given a range of values for the stepping probabilities of MTBD E. The data represents the results of 100 simulations with the maximum separation distance set to be 48nm. If x% of steps are not passing then $1-x$% of steps are passing. Similarly, if x% of steps are alternating then $1-x$% of steps are not alternating.

5.3.2 Interhead coordination

If dynein uses a more extensive form of interhead coordination, the probability that each MTBD steps will depend on the previous step. Therefore, the impact of dependent stepping probabilities on the model is investigated by taking $P_D \neq P_E$, whilst we continue to take the maximum separation distance to be $d = 48$nm. It is assumed that the probability that MTBD E steps increases if MTBD D stepped previously and decreases if MTBD E stepped previously. By taking $P_D = 70\%$ and $P_E = 30\%$ the results show the same mode of stepping to previous results, with a mixed stepping pattern of 82.60% not passing steps reflecting experimental observations of 83% (see Figures 5.6 and 5.7(a)). However, in comparison to our previous results, these results also resemble experimental observations with 73.82% of steps alternating in our simulations and 74% in experiments (see Figure 5.7(b)). This suggests that some form of coordination, in relation to the ATP cycles of each head domain, occurs between the motor domains of dynein, with one domain being more likely to step if the previous step was taken by the other motor domain. The proportion of alternating steps increases with an increase in the probability that MTBD E steps given that MTBD D stepped previously, with a completely hand-over-hand stepping profile associated with a probability of 100% (see Table 5.3 for results).

5.4 Artificially dimerized model in the absence of cargo

Many stepping experiments studying dynein are conducted using an artificially dimerized form. To study a dimerized form of dynein a shorter form of dynein's tail is modelled by using two identical springs connecting the tail to each of the AAA+ rings, this tail can be shortened according to the

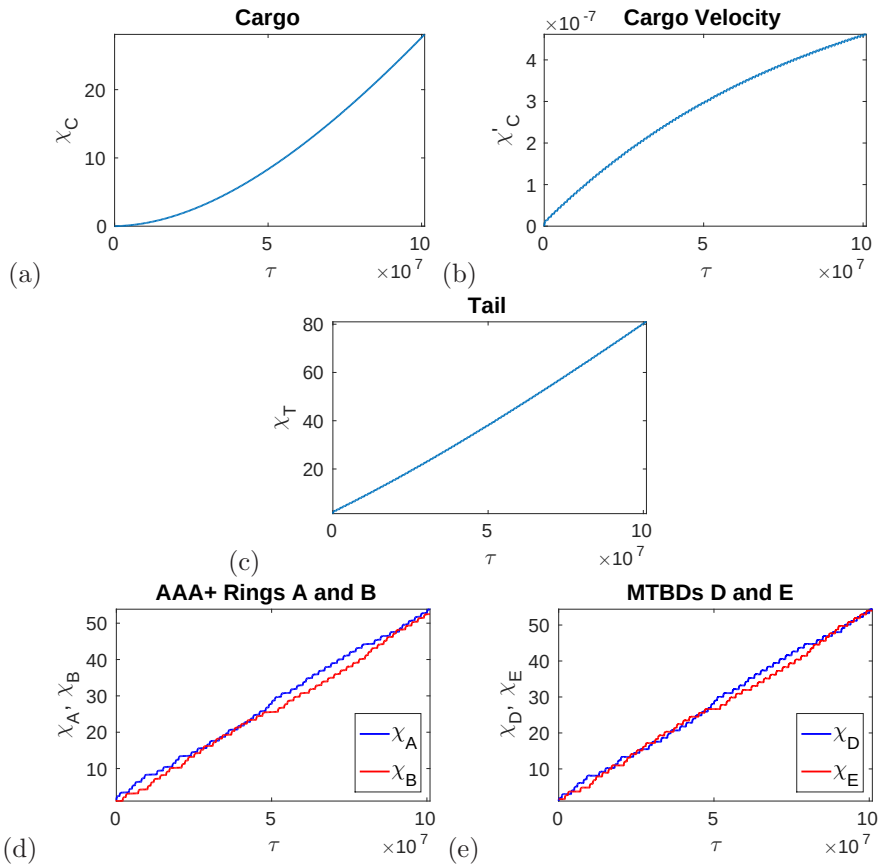

Figure 5.6: Numerical solutions to the model equations (5.10) - (5.15) with maximum separation distance between MTBDs at 48nm and the probability that MTBD E steps set at 70% if the previous step was taken by MTBD D, and 30% otherwise. Plots over the whole time corresponding to (a) trajectory of the cargo, (b) velocity profile of the cargo, (c) trajectory of the tail domain, (d) trajectory of the AAA+ rings, and (e) trajectory of the MTBDs.

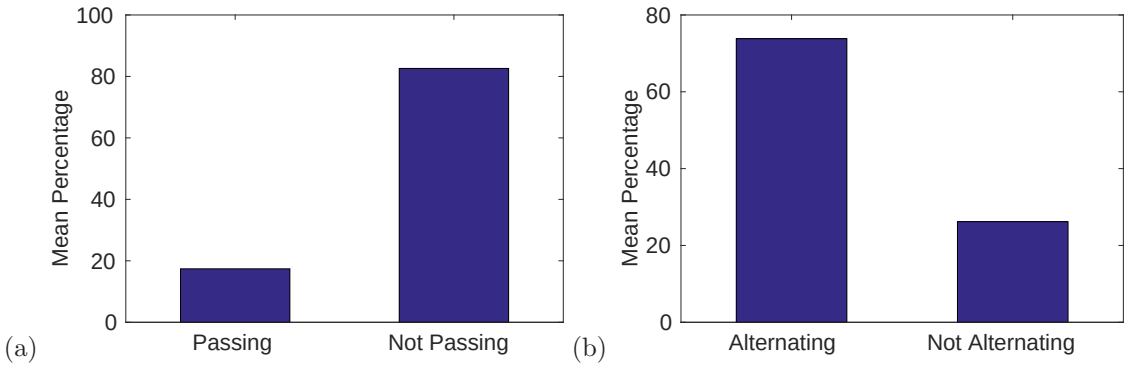

Figure 5.7: Bar charts showing the mean percentage of steps: (a) passing vs not passing and (b) alternating vs non-alternating. The data represents the results of 1000 simulations with the probability that MTBD E steps set at 70% if MTBD D stepped previously and 30% otherwise. The maximum separation distance is set to be 48nm.

specific dimerization by the use of the parameter L_T. It is also assumed that there is no cargo. The Qdots in these experiments tend to be attached to the AAA+ rings themselves and it is assumed that the effect of these Qdots on the dynamics can be ignored. The model equations (5.4)-(5.9) can be modified to:

$$m_T\frac{d^2x_T}{dt^2} = K_T\Big(x_B - x_T - L_T\cos(\theta_{BT})\Big) - K_T\Big(x_T - x_A - L_T\cos(\theta_{AT})\Big) - \gamma_T\frac{dx_T}{dt}, \tag{5.17}$$

$$m_M\frac{d^2x_A}{dt^2} = K_T\Big(x_T - x_A - L_T\cos(\theta_{AT})\Big) - K_S\Big(x_A - x_D - L_S\cos(\theta_{AD})\Big) - \gamma_M\frac{dx_A}{dt}, \tag{5.18}$$

$$m_M\frac{d^2x_B}{dt^2} = K_S\Big(x_E - x_B - L_S\cos(\theta_{BE})\Big) - K_T\Big(x_B - x_T - L_T\cos(\theta_{BT})\Big) - \gamma_M\frac{dx_B}{dt}, \tag{5.19}$$

$$\begin{aligned} m_S h_D(t,x_D,x_E,d)\frac{d^2x_D}{dt^2} = h_D(t,x_D,x_E,d)\Big[&-\gamma_{ATP}\frac{dx_D}{dt} - K_{ATP}(x_D - p_i - 2L_{ATP}) \\ &- K_S(x_D - x_A + L_S\cos(\theta_{AD}))\Big] - \gamma_S\frac{dx_D}{dt}, \end{aligned} \tag{5.20}$$

$$\begin{aligned} m_S h_E(t,x_D,x_E,d)\frac{d^2x_E}{dt^2} = h_E(t,x_D,x_E,d)\Big[&-\gamma_{ATP}\frac{dx_E}{dt} - K_{ATP}(x_E - p_{i+1} - 2L_{ATP}) \\ &- K_S(x_E - x_B - L_S\cos(\theta_{BE}))\Big] - \gamma_S\frac{dx_E}{dt}, \end{aligned} \tag{5.21}$$

for $t \in [0, T_{Final}]$ with initial conditions:

$$x_T(0) = 0,\ x_A(0) = L_T,\ x_B(0) = L_T,\ x_D(0) = p_0 = L_T - 4, \quad \text{and} \quad x_E(0) = p_1 = L_T + 4.$$

The non-dimensionalistation is implemented similarly with a notable change for the time characteristic:

$$x_T = L_T\chi_T,\ x_A = L_S\chi_A,\ x_B = L_S\chi_B,\ x_D = L_S\chi_D,\ x_E = L_S\chi_E, \quad \text{and} \quad t = \frac{m_T}{\gamma_T}\tau.$$

Hence, the non-dimensional model system is given by the following ODEs:

$$\alpha_T\frac{d\chi_T}{d\tau} = \Big(\frac{1}{\rho_2}(\chi_B + \chi_A) - \cos(\theta_{BT}) + \cos(\theta_{AT})\Big) - 2\chi_T, \tag{5.22}$$

$$\alpha_M\frac{d\chi_A}{d\tau} = \rho_2\kappa_2\Big(\chi_T - \cos(\theta_{AT})\Big) + \Big(\chi_D + \cos(\theta_{AD})\Big) - (\kappa_2 + 1)\chi_A, \tag{5.23}$$

$$\alpha_M\frac{d\chi_B}{d\tau} = \Big(\chi_E - \cos(\theta_{BE})\Big) + \rho_2\kappa_2\Big(\chi_B + \cos(\theta_{BT})\Big) - (\kappa_2 + 1)\chi_B, \tag{5.24}$$

$$\begin{aligned} \Big(\alpha_S + \alpha_{ATP}h_D(\tau,\chi_D,\chi_E,\delta)\Big)\frac{d\chi_D}{d\tau} = h_D(\tau,\chi_D,\chi_E,\delta)\Big[&\kappa_3(\beta_i + 2\rho_3) \\ &+ \Big(\chi_A - \cos(\theta_{AD})\Big) - (1 + \kappa_3)\chi_D\Big], \end{aligned} \tag{5.25}$$

$$\begin{aligned} \Big(\alpha_S + \alpha_{ATP}h_E(\tau,\chi_D,\chi_E,\delta)\Big)\frac{d\chi_E}{d\tau} = h_E(\tau,\chi_D,\chi_E,\delta)\Big[&\kappa_3(\beta_{i+1} + 2\rho_3) \\ &+ \Big(\chi_B + \cos(\theta_{BE})\Big) - (1 + \kappa_3)\chi_E\Big]. \end{aligned} \tag{5.26}$$

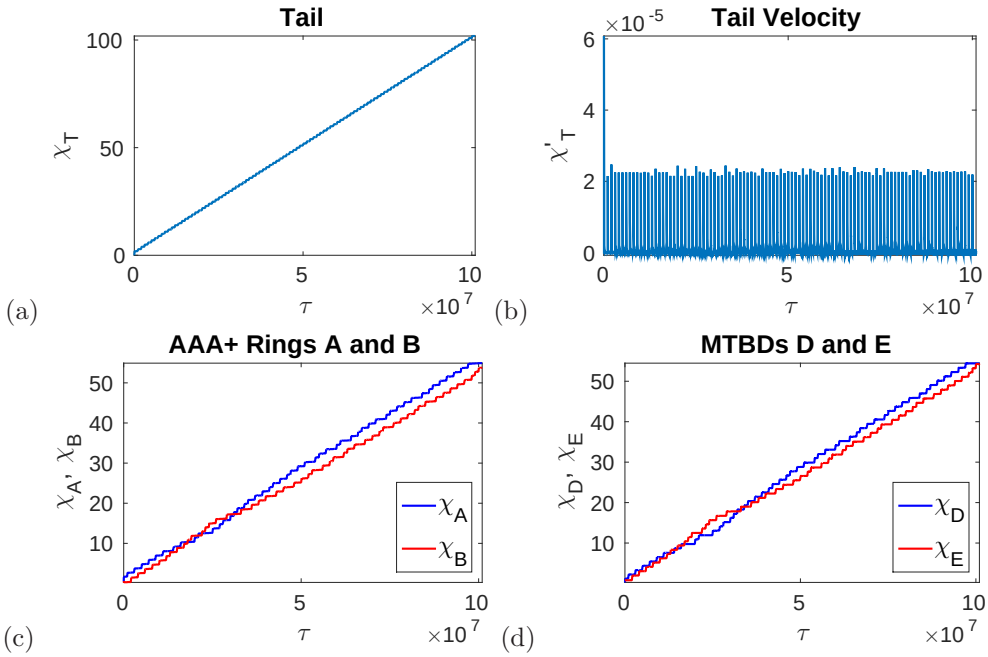

Figure 5.8: Numerical solutions to the model equations (5.22) - (5.26) with maximum separation distance between MTBDs at 48nm and the probability that MTBD E steps at 70% if the previous step was taken by MTBD D, and 30% otherwise. Plots over the whole time corresponding to (a) trajectory of the tail, (b) velocity profile of the tail, (c) trajectories of the AAA+ rings, and (d) trajectories of the MTBDs.

The nondimensional parameters are given by

$$\alpha_T = \frac{\gamma_T^2}{m_T K_T}, \quad \alpha_M = \frac{\gamma_M \gamma_T}{m_T K_S}, \quad \alpha_S = \frac{\gamma_S \gamma_T}{m_T K_S}, \quad \alpha_{ATP} = \frac{\gamma_{ATP} \gamma_T}{m_T K_S}, \quad \rho_2 = \frac{L_T}{L_S}, \quad \rho_3 = \frac{L_{ATP}}{L_S},$$
$$\kappa_2 = \frac{K_T}{K_S}, \quad \kappa_3 = \frac{K_{ATP}}{K_S}, \quad \beta_i = \frac{p_i}{L_S}, \quad \text{and} \quad \delta = \frac{d}{L_S}.$$

See Table 5.1 for dimensional parameter values. The trajectories for the tail, AAA+ rings and MTBDs are similar to results from the full model (see Figure 5.8). The statistics for the stepping patterns are also similar with 82.80% not-passing steps and 73.86% alternating steps (see Figure 5.9). This is to be expected as these statistics reflect the stochastic parameters controlling the stepping of the complex which are unchanged in this variant of the model.

5.5 Variable angles

If the assumption that the angles in the model are fixed is relaxed then we must solve a two-dimensional system. Let y_C, y_T, y_A, y_B, y_D and y_E represent the height of the cargo, tail, AAA+ rings A and B, and MTBDs D and E respectively. The only forces applied vertically are the spring forces and drag, by using Hooke's Law to model the spring force and equating the mass multiplied

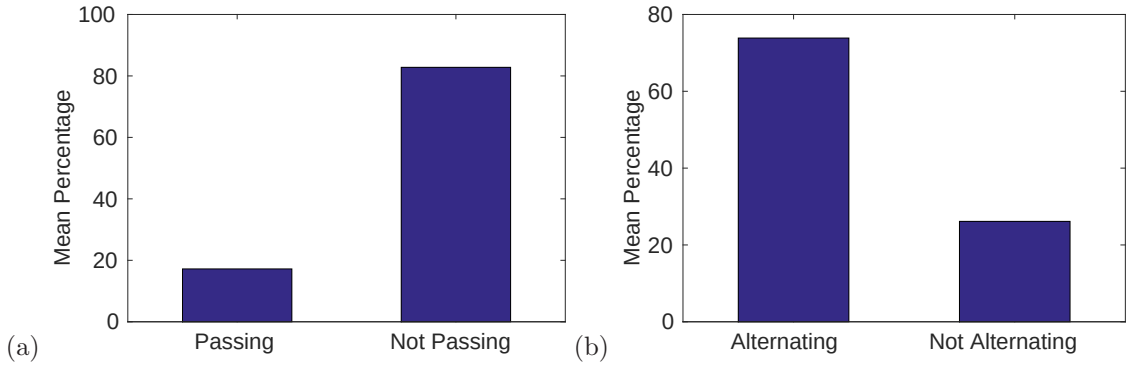

Figure 5.9: Bar charts showing the mean percentage of steps: (a) passing vs not passing and (b) alternating vs non-alternating. The data represents the results of 1000 simulations with the probability that MTBD E steps set at 70% if the previous step was taken by MTBD D, and 30% otherwise. The maximum separation distance is set to be 48nm.

by the acceleration to the net force we derive the following system of equations for the cargo, tail and AAA+ rings:

$$m_C\frac{d^2y_C}{dt^2} = -K_C(y_C - y_T - L_C\sin(\theta_{CT})) - \gamma_C\frac{dy_C}{dt}, \tag{5.27}$$

$$m_T\frac{d^2y_T}{dt^2} = K_C(y_C - y_T - L_C\sin(\theta_{CT})) - K_T(y_T - y_B - L_T\sin(\theta_{BT})) - K_T(y_T - y_A - L_T\sin(\theta_{AT})) - \gamma_T\frac{dy_T}{dt}, \tag{5.28}$$

$$m_A\frac{d^2y_A}{dt^2} = K_T(y_T - y_A - L_T\sin(\theta_{AT})) - K_S(y_A - y_D - L_S\sin(\theta_{AD})) - \gamma_A\frac{dy_A}{dt}, \tag{5.29}$$

$$m_B\frac{d^2y_B}{dt^2} = K_T(y_T - y_B - L_T\sin(\theta_{BT})) - K_S(y_B - y_E - L_S\sin(\theta_{BE})) - \gamma_B\frac{dy_B}{dt}, \tag{5.30}$$

with the angles defined by:

$$\theta_{CT} = \arctan\Big(\frac{y_C - y_T}{x_T - x_C}\Big),\ \theta_{AT} = \arctan\Big(\frac{y_T - y_A}{x_T - x_A}\Big),\ \theta_{BT} = \arctan\Big(\frac{y_T - y_B}{x_B - x_T}\Big),$$
$$\theta_{AD} = \arctan\Big(\frac{y_A - y_D}{x_D - x_A}\Big), \quad \text{and} \quad \theta_{BE} = \arctan\Big(\frac{y_B - y_E}{x_E - x_B}\Big).$$

For the MTBDs it is assumed that they do not move away from the microtubule. This is a valid assumption while they are attached and biophysical models have predicted that the movement of the MTBDs under the action of ATP hydrolysis is one-dimensional along the microtubule [153]. Therefore $y_D = 0$ and $y_E = 0$. The vertical components are non-dimensionalised as follows: $y_C = L_C\psi_C$, $y_T = L_T\psi_T$, $y_A = L_S\psi_A$, $y_B = L_S\psi_B$, $y_D = L_S\psi_D$, $y_E = L_S\psi_E$ and $t = \frac{m_C}{\gamma_C}\tau$ and acceleration is assumed to be small. Therefore, the following system of nondimensional ODEs is

obtained:

$$\alpha_C \frac{d\psi_C}{d\tau} = -(\psi_C - \frac{1}{\rho_1}\psi_T - \sin(\phi_{CT})), \tag{5.31}$$

$$\alpha_T \frac{d\psi_T}{d\tau} = \kappa_1(\rho_1\psi_C - \psi_T - \rho_1 \sin(\phi_{CT})) - (\psi_T - \frac{1}{\rho_2}\psi_B - \sin(\phi_{BT})) - (\psi_T - \frac{1}{\rho_2}\psi_A - \sin(\phi_{AT})), \tag{5.32}$$

$$\alpha_M \frac{d\psi_A}{d\tau} = \kappa_2(\rho_2\psi_T - \psi_A - \rho_2 \sin(\phi_{AT})) - (\psi_A - \psi_D - \sin(\phi_{AD})), \tag{5.33}$$

$$\alpha_M \frac{d\psi_B}{d\tau} = \kappa_2(\rho_2\psi_T - \psi_B - \rho_2 \sin(\phi_{BT})) - (\psi_B - \psi_E - \sin(\phi_{BE})), \tag{5.34}$$

$$\frac{d\psi_D}{d\tau} = 0, \tag{5.35}$$

$$\frac{d\psi_E}{d\tau} = 0; \tag{5.36}$$

where

$$\alpha_C = \frac{\gamma_C\gamma_C}{m_C K_C}, \quad \alpha_T = \frac{\gamma_T\gamma_C}{m_C K_T}, \quad \alpha_M = \frac{\gamma_M\gamma_C}{m_C K_S},$$
$$\rho_1 = \frac{L_C}{L_T}, \quad \rho_2 = \frac{L_T}{L_S},$$
$$\kappa_1 = \frac{K_C}{K_T}, \quad \kappa_2 = \frac{K_T}{K_S},$$

with the angles are given by:

$$\phi_{CT} = \arctan\Big(\frac{\rho_1\psi_C - \psi_T}{\chi_T - \rho_1\chi_C}\Big),\ \phi_{AT} = \arctan\Big(\frac{\rho_2\psi_T - \psi_A}{\rho_2\chi_T - \chi_A}\Big),\ \phi_{BT} = \arctan\Big(\frac{\rho_2\psi_T - \psi_B}{\chi_B - \rho_2\chi_T}\Big),$$
$$\phi_{AD} = \arctan\Big(\frac{\psi_A - \psi_D}{\chi_D - \chi_A}\Big), \quad \text{and} \quad \phi_{BE} = \arctan\Big(\frac{\psi_B - \psi_E}{\chi_E - \chi_B}\Big).$$

Initial conditions are given by

$$\psi_C(0) = \frac{1}{\rho_1}sin(\phi_{BT}(0)) + \frac{1}{\rho_1\rho_2}sin(\phi_{BE}(0)),\ \psi_T(0) = sin(\phi_{BT}(0)) + \frac{1}{\rho_2}sin(\phi_{BE}(0)),$$
$$\psi_A(0) = sin(\phi_{AD}(0)),\ \psi_B(0) = sin(\phi_{BE}(0)),\ \psi_D(0) = 0,\ \psi_E(0) = 0,$$

with angles defined by:

$$\phi_{CT}(0) = \pi,\ \phi_{AT}(0) = \frac{33\pi}{180},\ \phi_{BT}(0) = \frac{33\pi}{180},\ \phi_{AD}(0) = \frac{53\pi}{180}, \quad \text{and} \quad \phi_{BE}(0) = \frac{53\pi}{180},$$

given our previous assumption on the position of the spring connecting the cargo to the tail domain and using experimental results by Burgess *et al.,* for all other angles [55]. These results show very similar trajectories for the cargo, tail, AAA+ rings and MTBDs for the horizontal motion (see Figure 5.10). The statistics for the stepping pattern are also very similar with 82.60%

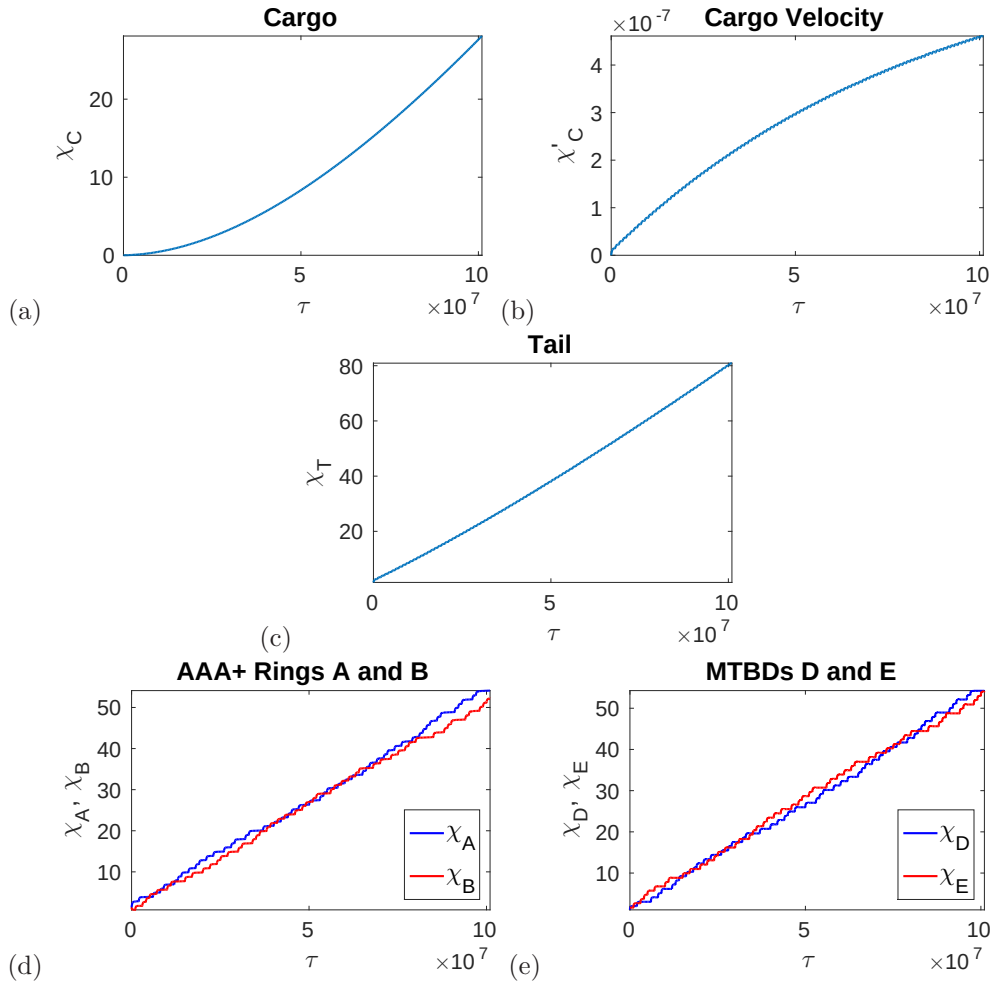

Figure 5.10: Numerical solutions to the model equations (5.10) - (5.15), (5.31) - (5.36) with maximum separation distance between MTBDs at 48nm and the probability that MTBD E steps at 70% if the previous step was taken by MTBD D, and 30% otherwise. Plots over the whole time corresponding to (a) trajectory of the cargo, (b) velocity profile of the cargo, (c) trajectory of the tail domain, (d) trajectories of the AAA+ rings, and (e) trajectories of the MTBDs; in the horizontal direction.

non-passing steps and 73.77% alternating steps (see Figure 5.12). This is to be expected as the stochastic parameters modelling the stepping behaviour are unchanged in this model. The vertical trajectories do not appear to reflect experimental observations (see Figure 5.11) [55]. Allowing the angles to vary freely may not be biologically realistic and so further work needs to be carried out in order to model the changes in these angles appropriately. Furthermore, these preliminary results do suggest that the assumption on fixed angles in the current model is unlikely to affect our results negatively and is therefore a reasonable assumption.

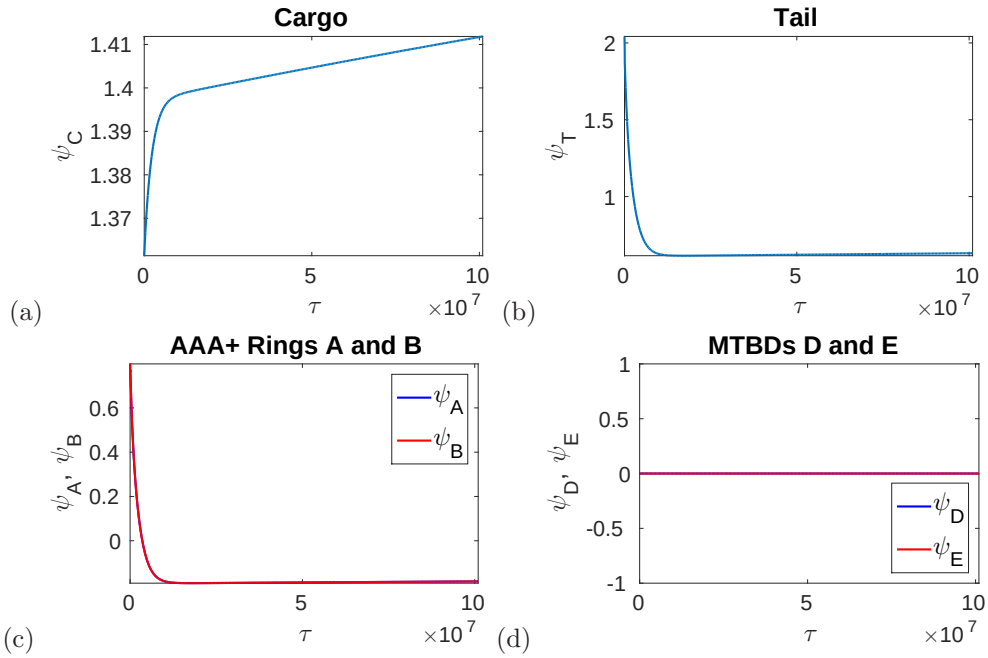

Figure 5.11: Numerical solutions to the model equations (5.10) - (5.15), (5.31) - (5.36) with maximum separation distance between MTBDs at 48nm and the probability that MTBD E steps at 70% if the previous step was taken by MTBD D, and 30% otherwise. Plots over the whole time corresponding to (a) trajectory of the cargo, (b) trajectory of the tail domain, (c) trajectories of the AAA+ rings, and (d) trajectories of the MTBDs; in the vertical direction.

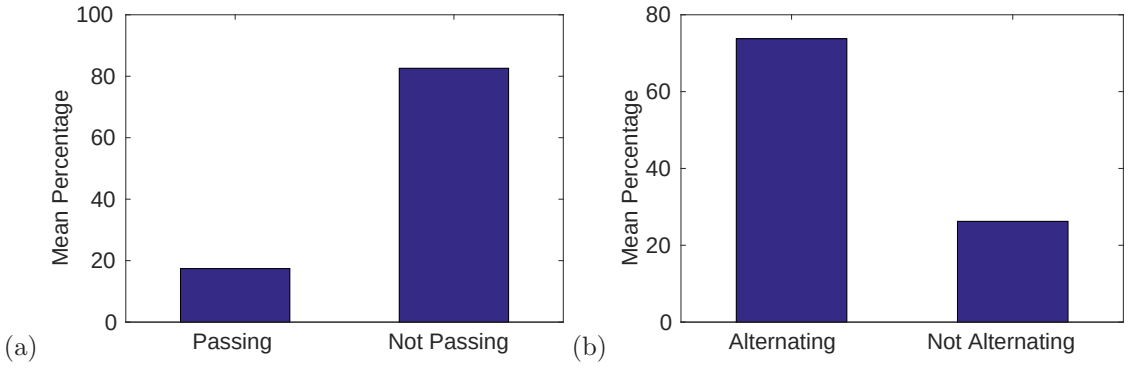

Figure 5.12: Bar charts showing the mean percentage of steps: (a) passing vs not passing and (b) alternating vs non-alternating. The data represents the results of 1000 simulations with the probability that MTBD E steps set at 70% if the previous step was taken by MTBD D, and 30% otherwise. The maximum separation distance is set to be 48nm.

5.6 Non-identical head domains

Dynein uses both motor domains to step processively, however it is unclear if both motor domains need to produce force using ATP hydrolysis or if the microtubule binding ability is sufficient. Hence we relax our assumption that the ATP force is the same for both MTBDs and use different parameters for each MTBD: $\gamma_{ATP,i}$, $K_{ATP,i}$ and $L_{ATP,i}$ for MTBD i in equations (5.8) and (5.9). The equations of motion for the cargo, tail and AAA+ rings A and B continue to be modelled in the same way by equations (5.4) - (5.7). However, rather than solving over a fixed time interval $t_{i+1} - t_i = \frac{1}{N} T_{Final}$ for each step, we end our time interval once the MTBD has reached the next binding site; taking the interval $[t_i, t_{i+1}] \subset [t_i, t_i + t_{max}]$ with

$$t_{i+1} = \min \left\{ t \in [t_i, t_i + t_{max}] : x_i(t) \geq p_{j+2} \right\}$$

where p_{j+2} is the next binding site for the unbound MTBD i. This allows the two MTBDs to take different lengths of time to reach the next binding site.

We consider a model in which one of the motor domains is the wild type and the other is mutated. We assume that the mutated domain cannot bind ATP and hence produces no ATP force. Therefore, we set the probability that MTBD E, the mutated domain, steps at 0% and the parameters $\gamma_{ATP,E}$ and $K_{ATP,E}$ equal to zero. All other parameters are modelled using their primary values in Table 5.1 with $\gamma_{ATP,D} = \gamma_{ATP}$, $K_{ATP,D} = K_{ATP}$ and $L_{ATP,D} = L_{ATP,E} = L_{ATP}$. The results show that in this case the wild type domain steps ahead of the mutant domain, with the mutant domain unbinding from the microtubule when the maximum separation distance is reached and moving solely due to the tension within the complex (see Figure 5.13 (e)). The velocity of the cargo is significantly lower than in the wild type models (see Figure 5.13 (b)). The stepping profile also differs from the wild type model with a primarily non-alternating pattern and a solely shuffling stepping profile (see Figure 5.14). This is to be expected as the mutant head can only move through tension. We note that the velocity of the cargo falls back to zero during the early stage of transport (see Figure 5.13 (b)), this is likely to be caused by the slow movement of the mutant head domain compared to the faster stepping of the wild type head.

DeWitt *et al.,* consider a similar mutation where ATP can bind but cannot be hydrolysed at the AAA1 domain [31]. Their results showed that in a heterodimeric dynein, composed of one wild type and one mutant head lacking the ability to hydrolyse ATP, only one wild type force generating head was needed for processive movement. The mutant domain was weakly associated with the microtubule and usually stepped towards the wild type domain with occasional stepping in front of

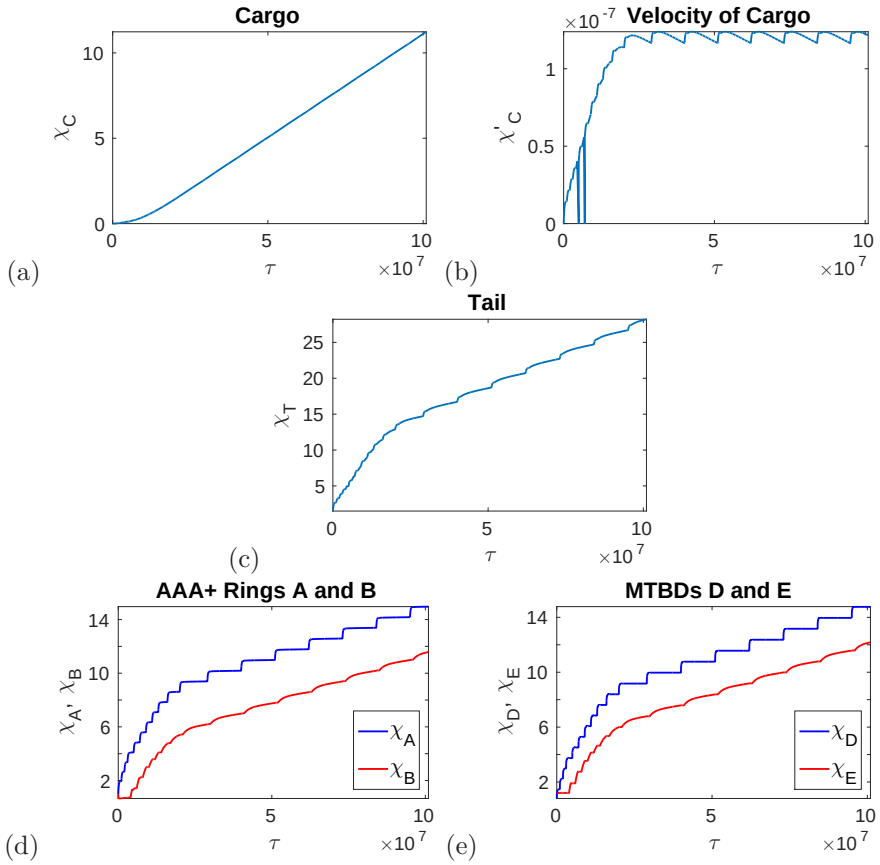

Figure 5.13: Numerical solutions to the mutated model equations (5.10) - (5.15) as described in Section 5.6 with maximum separation distance between MTBDs at 48nm and the probability that MTBD E steps set to be 0%, $\gamma_{ATP,E} = 0$ and $K_{ATP,E} = 0$. Plots over whole time corresponding to (a) trajectory of the cargo, (b) velocity profile of the cargo, (c) trajectory of the tail domain, (d) trajectory of the AAA+ rings, and (e) trajectory of the MTBDs.

the wild type domain or taking backward steps. Our results reflect the general profiles of forward stepping by the complex however there are some behaviours that they do not account for such as backward stepping and a variable step size. The limitations in our model of allowing the wild type domain to only step forwards and fixing the step size are likely to be the causes of this. For example, the model only considers continuous forward stepping by the wild type domain and so we do not see it stepping back from the lead. The presence of ATP in the AAA1 site may prevent rebinding to the microtubule which is not considered in our model. The mutation modelled does not allow ATP to bind and hence we are only modelling detachment through tension, whereas the other types of motion seen experimentally could be accounted for by ATP binding causing detachment from the microtubule prematurely.

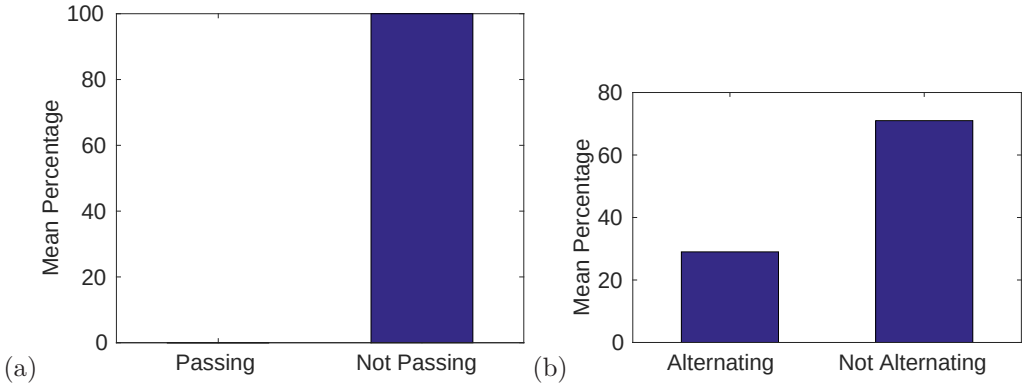

Figure 5.14: Bar charts showing the mean percentage of steps: (a) passing vs not passing, and (b) alternating vs non-alternating. The data represents the results of 1000 simulations with the probability that MTBD E steps set to be 0%, $\gamma_{ATP,E} = 0$ and $K_{ATP,E} = 0$. The maximum separation distance is set to be 48nm.

5.7 Discussion

In this chapter, we have derived a general stochastic mechanistic model that describes the transport mechanism of cytoplasmic dynein under continual forward stepping with a fixed step size. Our results give a mixed stepping pattern with a predominantly shuffling stepping profile matching experimental observations. We have shown that there is likely to be some form of interhead coordination between the timing of the ATP cycles of the two AAA+ rings in order to account for the alternating pattern seen in experiments. In comparison to results for limited coordination, through attachment to the microtubule only, we see that the velocity is the same. Hence, this form of coordination has no direct effect on the velocity.

We have also been able to model some form of mutation where one motor domain is unable to perform ATP hydrolysis leading to a decrease in velocity. This model needs to be validated experimentally so that the effect of this mutation can be analysed directly through tension based detachment and movement only. Further development of the model to allow for backward stepping, variable step size and random detachment of the mutated domain would be beneficial to make comparisons to experimental work.

Experimental observations also show pausing, backward motion and a variable step size; this is not achieved here due to restrictions within the model, however the model can be easily extended to include these characteristics and this is explored in Chapter 6.

Chapter 6

Stochastic Model with Backwards Stepping, Variable Step Size and Dwelling

Experimental observations have shown that dynein exhibits backward stepping for both the tail domain ($20-23\%$ of steps) and the motor domain ($13-20\%$ of steps) [30, 31, 32]. Dynein also exhibits a variable step size with Reck-Peterson *et al.,* reporting a predominant step size of 16nm for the motor domain but with a large number of longer steps sizes including step sizes greater than 56nm (not exceeding 64nm) [30]. Therefore, we aim to introduce these characteristics into the model. Dynein has been shown to dwell between steps, with measured dwell times for the tail domain averaging 2s and is well described by an exponential distribution [30]. In order to incorporate this into the model we include a variable time interval between steps when both MTBDs are bound, i.e. $\frac{dx_D}{dt} = 0$ and $\frac{dx_E}{dt} = 0$. A dwell time of 2s is of a significantly larger scale than the current time scale, i.e. 2×10^9 ns, which reflects reasonably sized parameters (see Sections 3.1 and 5.2.1). Hence, we shall take two approaches for modelling dwelling processes. In the first instance, we will model minimal dwelling within the same scales as our other parameters (see Sections 3.1 and 5.2.1), whilst introducing backward stepping and a variable step size. Next, we will look at a multi-scale framework, using a different scaling of time for stepping and dwelling intervals.

6.1 Stochastic stepping with minimal dwelling

Stochasticity is modelled in the following ways: randomness in which AAA+ ring binds ATP: AAA+ ring A or B, randomness in when an AAA+ ring binds ATP: time t_{bind}, randomness in the direction of motion of the unbound MTBD, and step size. We therefore define the following parameters for use in the numerical simulations: the value of P_D (similarly P_E) is assigned to the probability that MTBD E steps given that MTBD D (similarly E) stepped previously. The maximum separation distance d that can occur between the MTBDs and the mean dwell time between steps μ are predefined. Let n be a parameter modulating the step size, i.e. the step size is given by nL_{ATP}, and the probability that random backward stepping occurs, P_{Back}, is also predefined. Consider $t \in [0, T_F + Q_F]$ with $T_F > 0$ and $Q_F = \sum_{k=1}^{N} q_{1,k}$. Here, N represents the total number of steps, T_F the total time spent stepping and Q_F the total time spent dwelling with $q_{1,k}$ the length of individual intervals of dwelling. Let $\mathbf{q_1} = \{q_{1,k}\}_{k=1:N}$ be a random vector where $q_{1,k}$ is from the exponential distribution with mean μ. Furthermore, let $\mathbf{q_2} = \{q_{2,k}\}_{k=1:N}$ and $\mathbf{q_3} = \{q_{3,k}\}_{k=1:N}$ be random vectors where $q_{2,k}$ and $q_{3,k}$ are from the uniform distribution on $(0, 1)$; these will determine the choice of AAA+ ring and the direction of stepping respectively. We continue to use a fixed time interval for stepping, T_{Step}, giving $T_F = NT_{Step}$.

For $t \in [t_i, t_{i+1}]$, where $t_{i+1} = t_i + \frac{T_F}{N}$, given that MTBD j stepped previously if $q_{2,i} < P_j$ then MTBD E is set to be in the unbound state and MTBD D is set to be in the bound state. Otherwise we assume that the MTBD D is in the unbound state and MTBD E in the bound state. This is described by the step functions $h_{2,D}$ and $h_{2,E}$:

$$h_{2,E}(t) = \begin{cases} 1 & \text{if} \quad q_{2,i} < P_j, \\ 0 & \text{otherwise;} \end{cases} \tag{6.1}$$

and similarly

$$h_{2,D}(t) = 1 - h_{2,E}(t). \tag{6.2}$$

Note that these step functions differ from Chapter 5 equations (5.3) - (5.2) as they do not depend on the maximum separation distance, which is used to determine the *direction of a step* rather than *which head steps* as in the previous chapter. If the unbound MTBD is ahead of the other and the maximum separation distance has been reached or if $q_{3,i} < P_{Back}$ then the unbound MTBD is

set to move backwards; otherwise it steps forwards. This can be defined by the step function:

$$g_D(x_D, x_E, t, d, n) = \begin{cases} -n & \text{if} \quad x_D - x_E > d \quad \text{or} \quad q_{3,i} < P_{Back}, \\ n & \text{otherwise}, \end{cases} \tag{6.3}$$

where n is a parameter modulating the step size. The equivalent function for MTBD E can be defined similarly with

$$g_E(x_D, x_E, t, d, n) = \begin{cases} -n & \text{if} \quad x_E - x_D > d \quad \text{or} \quad q_{3,i} < P_{Back}, \\ n & \text{otherwise}. \end{cases} \tag{6.4}$$

Then, given $q_{1,i}$ the system is set to dwell for $t \in [t_{i+1}, t_{i+1} + q_{1,i}]$, i.e. both MTBDs are set to be in the bound state. Here, we can define a step function $h_q(t, t_{i+1})$ given by:

$$h_q(t, t_{i+1}) = \begin{cases} 1 & \text{if} \quad t \leq t_{i+1} \\ 0 & \text{otherwise}; \end{cases} \tag{6.5}$$

for $t \in [t_i, t_{i+1} + q_{1,i}]$ with $i = 1, 2, ..., N$. Define $h_{3,j}(t) = h_q(t, t_{i+1}) h_{2,j}(t)$ for $j = D, E$. The equations (5.8) -(5.9) are therefore amended to obtain the following ODEs for MTBDs D and E:

$$\begin{aligned} m_S h_{3,D}(t) \frac{d^2 x_D}{dt^2} = h_{3,D}(t) \Big[&- \gamma_{ATP} \frac{dx_D}{dt} - K_{ATP} \Big(x_D - p_i - g_D(x_D, x_E, t, d, n) L_{ATP} \Big) \\ &- K_S \Big(x_D - x_A + L_S \cos(\theta_{AD}) \Big) \Big] - \gamma_S \frac{dx_D}{dt}, \end{aligned} \tag{6.6}$$

$$\begin{aligned} m_S h_{3,E}(t) \frac{d^2 x_E}{dt^2} = h_{3,E}(t) \Big[&- \gamma_{ATP} \frac{dx_E}{dt} - K_{ATP} \Big(x_E - p_{i+1} - g_E(x_D, x_E, t, d, n) L_{ATP} \Big) \\ &- K_S \Big(x_E - x_B - L_S \cos(\theta_{BE}) \Big) \Big] - \gamma_S \frac{dx_E}{dt}, \end{aligned} \tag{6.7}$$

for $t \in [0, T_F + Q_F]$. The motion of the cargo, tail and AAA+ rings continues to be modelled by equations (5.4) - (5.7). The model is non-dimensionalised as in Section 5.2.1 and the second order derivatives are neglected; the motion of the cargo, tail and AAA+ rings continue to be described by equations (5.10) - (5.13), whilst the MTBDs are described by the following equations:

$$\begin{aligned} \Big(\alpha_S + \alpha_{ATP} \hat{h}_D(\tau) \Big) \frac{d\chi_D}{d\tau} = \hat{h}_D(\tau) \Big[&\kappa_3 \Big(\beta_i + \hat{g}_D(\chi_D, \chi_E, \tau) \rho_3 \Big) \\ &+ \Big(\chi_A - \cos(\theta_{AD}) \Big) - (1 + \kappa_3) \chi_D \Big], \end{aligned} \tag{6.8}$$

$$\begin{aligned} \Big(\alpha_S + \alpha_{ATP} \hat{h}_E(\tau) \Big) \frac{d\chi_E}{d\tau} = \hat{h}_E(\tau) \Big[&\kappa_3 \Big(\beta_{i+1} + \hat{g}_E(\chi_D, \chi_E, \tau) \rho_3 \Big) \\ &+ \Big(\chi_B + \cos(\theta_{BE}) \Big) - (1 + \kappa_3) \chi_E \Big], \end{aligned} \tag{6.9}$$

for $\tau \in [0, \tau_{Final}]$ where $\tau_{Final} = \frac{\gamma_C}{m_C}(T_F + Q_F)$. We take $\hat{g}_j(\chi_D, \chi_E, \tau) = g_j(\chi_D, \chi_E, \tau, \delta, n)$ and $\hat{h}_j(\tau) = h_q(\tau, \tau_{i+1})h_{2,j}(\tau)$ for $j = D, E$. The initial conditions continue to be given by equations (5.16).

6.2 Backwards stepping with fixed step size

First, we consider backward stepping with a fixed step size. We allow $n \in \{2, -2\}$, where $n = 2$ represents a forward step of size 16nm, the predominant forward step size [30], and $n = -2$ represents a backward step of size 16nm (see equations (6.3) and (6.4)). The scheme is implemented in MATLAB for N intervals of $[0, \tau_{Final}]$ with the non-dimensional time for each stepping interval taken to be $\tau_{step} = 10^6$ and using the solver *ode45* and tolerances given in Table 3.2 [164]. We consider $N = 100$ steps with minimal mean dwell time $\mu = 2$ns. In order to explore the effect of random backward stepping within the complex we take $P_{Back} = 10\%$. The primary value for the probability that MTBD E steps given that MTBD D (E) stepped previously is taken to be $P_D = 74\%$ ($P_E = 26\%$), reflecting experimental observations by Qiu *et al.,* [32], and the primary value of the maximum separation distance between the two MTBDs is taken to be 56nm. Variations in these values are explored below. For the initial step MTBD D is assumed to be in the unbound state and MTBD E is in an bound state and the system is solved for the initial conditions given by equations (5.16).

For each subsequent step a random number $q_{1,i}$ is generated from the exponential distribution with mean μ and the system of ODEs is solved for $\tau \in [\tau_{i+1}, \tau_{i+2}]$ in the dwelling state where $\tau_{i+2} = \tau_{i+1} + \frac{\gamma_C}{m_C} q_{1,i}$ (see equation (6.5)). Initial conditions are given by the values from the previous simulation:

$$\chi_C(\tau_{i+1}), \quad \chi_T(\tau_{i+1}), \quad \chi_A(\tau_{i+1}), \quad \chi_B(\tau_{i+1}), \quad \chi_D(\tau_{i+1}) \quad \text{and} \quad \chi_E(\tau_{i+1}).$$

Random numbers $q_{2,i}$ and $q_{3,i}$ are then generated from the uniform distribution on $(0, 1)$ to determine which head domain steps and in which direction (see equations (6.1) - (6.4)). The resulting ODE system is solved for $\tau \in [\tau_{i+2}, \tau_{i+3}]$, where $\tau_{i+3} = \tau_{i+2} + \tau_{step}$, with the initial conditions taken from the end values of the dwelling simulation:

$$\chi_C(\tau_{i+2}), \quad \chi_T(\tau_{i+2}), \quad \chi_A(\tau_{i+2}), \quad \chi_B(\tau_{i+2}), \quad \chi_D(\tau_{i+2}) \quad \text{and} \quad \chi_E(\tau_{i+2}).$$

The results show a trajectory for the cargo moving forwards with a more varied velocity profile

than in previous results, with some instances of decreasing velocity as opposed to a profile that increases over an initial transitory period and then oscillates within a band (see Figure 6.1). This is likely to be a result of the backward steps being predominant enough to slow motion, but not present enough to move the cargo backwards. In comparison the tail domain does not move solely in the forward direction, but does itself exhibit some backward motion. As implemented in the model, there are now backward steps taken by the MTBDs, whilst both passing and non-passing steps remain present (see Figure 6.1). In comparison to experimental observations on yeast stepping patterns we are able to achieve similar patterns with 74.03% alternating steps, as prescribed in the model, and more significantly 82.45% non-passing steps, which is not prescribed but arises from the model (see Figure 6.2). We can also achieve a range of backward steps in the model, in particular taking the probability of backward stepping to be 20% and the maximum separation distance to be 48nm results in 24.91% backward steps by the MTBDs to achieve similar levels to the experimental observations of Qiu *et. al.,* (23%) (see Figure 6.2), while to match the observations of Reck-Peterson *et. al.,* of 13% we can take the probability of backward stepping to be 10% and the maximum separation distance to be 56nm [32, 30] (see Table 6.1).

We explored variations in the maximum separation distance on the stepping patterns (see Table 6.2). We see that the percentage of alternating steps is not effected by the change in maximum separation distance, as this is prescribed by the model, however there is an effect on non-passing steps and backward steps. The reduction in maximum separation distance, below 56nm, increases the likelihood of backward stepping, this is to be expected as backward stepping is directly related to the separation distance in the model, with an unbound head stepping backwards if it is too far in front of the other MTBD. We also see that reducing the maximum separation distance increases the likelihood of passing steps, which is plausible as closer MTBDs are more likely to cross over one another during stepping.

Increasing the stepping probability of MTBD E after MTBD D has stepped, decreases the percentage of not passing steps slightly and also decreases the percentage of backward steps (see Table 6.3). This is likely to occur as the increased coordination would create a more efficient stepping pattern reducing the prevalence of wasteful backward steps by keeping the motor domains closer together and hence passing steps would also be more likely to occur.

Variations in backward stepping were explored with different maximum separation distances (see Table 6.1). A probability of backward stepping of 0% does not mean that there will be no backward stepping in the model since we use this parameter to represent random backward stepping, which we differentiate from tension related backward stepping. If we assume that there is no random

d	P_{Back}	% Not Passing Steps	% Alternating Steps	% Backward Steps
48	0	80.28	74.52	2.57
	10	81.68	73.53	13.19
	20	82.25	74.49	24.58
56	0	84.05	74.71	1.75
	5	84.19	74.07	7.33
	10	84.50	74.35	12.90
	15	85.97	74.18	17.78
	20	85.80	73.80	22.87
	25	84.90	74.36	28.24
	50	86.45	73.37	53.43
64	0	83.87	73.71	1.59
	10	85.72	73.43	12.96
	20	85.41	74.49	23.19

Table 6.1: Mean percentage of not passing, alternating and backward steps given a range of values for the probability of random backward stepping P_{Back}. The data represents the results of 100 simulations with the probability that MTBD E steps set at 74% if MTBD D stepped previously and 26% otherwise. The mean dwell time is taken to be 2ns and the maximum separation distance is d as given. If x% of steps are not passing then $1 - x$% of steps are passing. Similarly, if x% of steps are alternating then $1 - x$% of steps are not alternating.

backward stepping, then the only backward stepping present in the model is through the corrective backward steps taken when the MTBDs are too far apart. We see from the results that this gives a very low presence of backward stepping, much lower than in experimental results. Hence, this suggests that the MTBDs might randomly step backwards or that something external/excluded from the model may be causing it. Studies have shown that dynactin plays an important role in the directionality of dynein and hence we may need to explore these effects in greater detail [78]. The effects of two dimensional steps along the microtubule may also play a role in backward stepping if the motor domain rotates due to the off-axis components of the steps. We are currently setting external forces to be zero but these forces may play a role in the directionality of the head domain for *in vivo* studies. Increases in the probability of backward stepping only cause a slight increase in non passing steps once random backward stepping reaches 50% (see Table 6.1). This is an interesting result as the existence of random backward steps would be expected to allow the MTBDs to remain closer together compared to simulations without these steps, and hence lead to an increase in passing steps. However, this effect may in fact not be occurring and the random backward steps may be exacerbating the separation of the MTBDs or may not be prevalent enough to pull a forward MTBD back to the rearward MTBD.

d	% Not Passing Steps	% Alternating Steps	% Backward Steps
8	49.36	73.90	26.63
16	53.57	74.39	20.88
24	68.05	73.73	17.14
32	75.45	74.31	15.80
40	80.85	74.73	14.47
48	81.68	73.53	13.19
56	84.50	74.35	12.90
64	85.72	73.43	12.96
72	85.89	74.30	12.08
80	87.29	73.67	12.70

Table 6.2: Mean percentage of not passing, alternating and backward steps given a range of values for the maximum separation distance d. The data represents the results of 100 simulations with the probability that MTBD E steps set at 74% if MTBD D stepped previously and 26% otherwise. The probability of random backward stepping is set to be 10% and the mean dwell time is taken to be 2ns. If x% of steps are not passing then $1-x$% of steps are passing. Similarly, if x% of steps are alternating then $1-x$% of steps are not alternating.

d	P_D	P_E	% Not Passing Steps	% Alternating Steps	% Backward Steps
56	20	80	88.00	19.93	23.01
	30	70	87.13	29.90	17.87
	40	60	87.29	39.74	16.49
	50	50	86.23	50.06	15.41
	60	40	85.87	60.51	13.44
	70	30	84.17	70.82	13.28
	80	20	84.81	80.18	12.90

Table 6.3: Mean percentage of not passing, alternating and backward steps given a range of values for the stepping probabilities of MTBD E. The data represents the results of 100 simulations with the maximum separation distance set to be $d$nm as given. The probability of random backward stepping is set to be 10% and the mean dwell time is taken to be 2ns. If x% of steps are not passing then $1-x$% of steps are passing. Similarly, if x% of steps are alternating then $1-x$% of steps are not alternating.

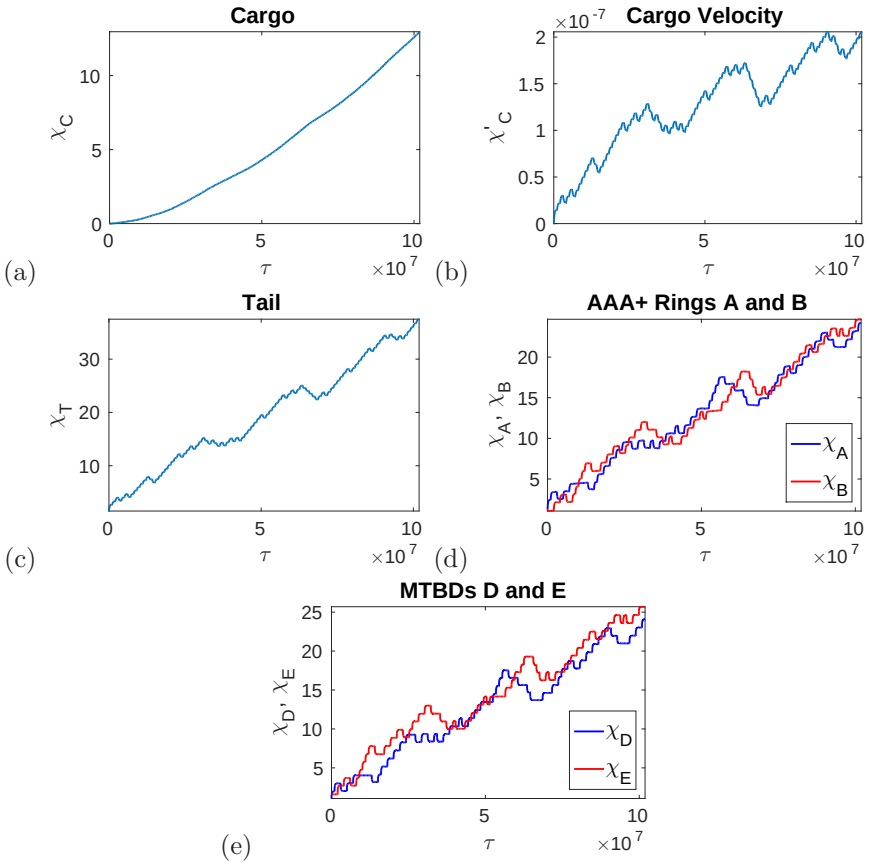

Figure 6.1: Numerical solutions to the model equations (5.10) - (5.13), (6.8) - (6.9) with $n = 2$ fixed, maximum separation distance between MTBDs at 48nm and the probability that MTBD E steps set at 74% if the previous step was taken by MTBD D, and 26% otherwise. The mean dwell time is taken to be 2ns and the probability of random backward stepping is taken to be 20%. Plots over the whole time corresponding to (a) trajectory of the cargo, (b) velocity profile of the cargo, (c) trajectory of the tail domain, (d) trajectories of the AAA+ rings, and (e) trajectories of the MTBDs.

6.3 Variable step size

Dynein exhibits a variable step size in experiments, with a predominant step of 16nm, with both smaller and larger step sizes present [30]. We therefore extend the model to incorporate this variability in step sizes by allowing the parameter n in the above model to vary (see equations (6.3) and (6.4)). The numerical results are run as in the backward stepping model above, however before each step we generate the step size randomly. We take n from the Poisson distribution about 2 to give the step size nL_{ATP} nm for the forward step sizes and n from the Poisson distribution about 1 for the backward steps to give the step size $-nL_{ATP}$ nm. Experimental results show backward steps to be smaller than forward steps, with a predominant step size of 8nm [30]. The use of a Poisson distribution allows the possibility of the MTBD to take a step size of 0. This would represent the possibility of the MTBD detaching from the microtubule but then rebinding in the same place which is biologically realistic. However, experimental data may not include these

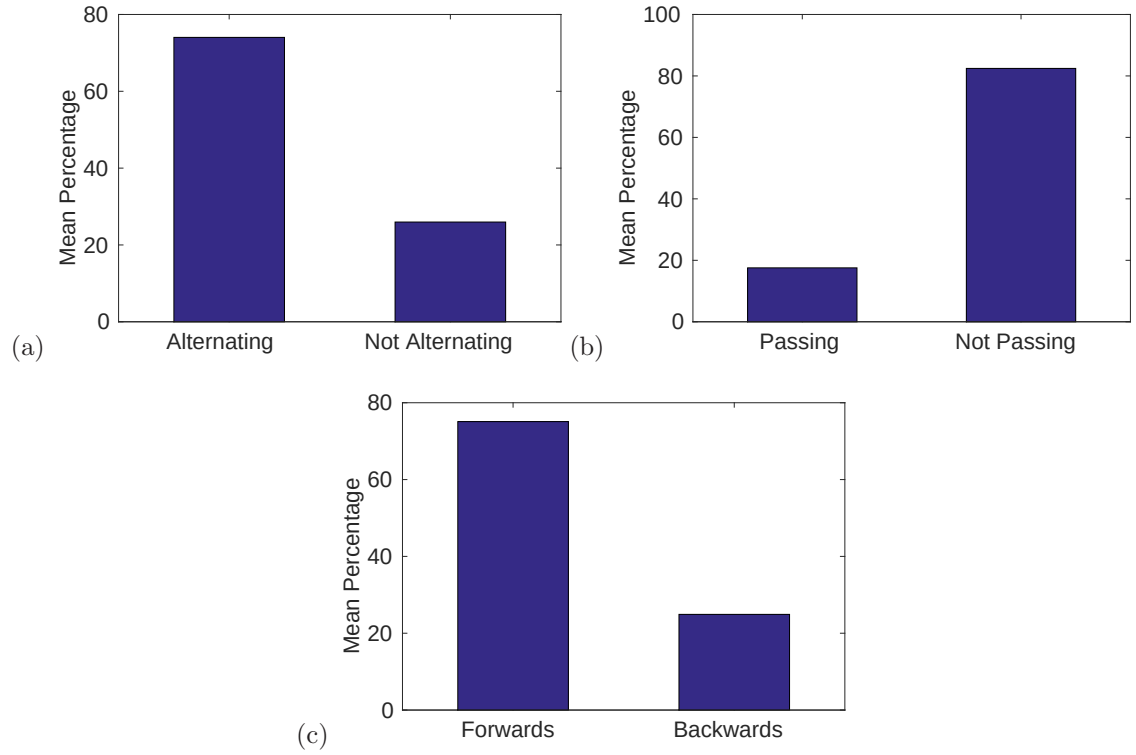

Figure 6.2: Bar charts showing the mean percentage of steps: (a) passing vs not passing, (b) alternating vs non-alternating, and (c) forward vs backward. The data represents the results of 1000 simulations for $n = 2$ fixed with the probability that MTBD E steps set at 74% if MTBD D stepped previously and 26% otherwise. The maximum separation distance is set to be 48nm, the mean dwell time is 2ns and the probability of random backward stepping is taken to be 20%.

incidents as steps and so this must be taken into account when making statistical comparisons. The simulations are therefore run using three scenarios:

- Option 1: Zero steps are included in the model but not counted as part of the alternating stepping pattern.
- Option 2: Zero steps are not included. (An alternative n will be computed if $n = 0$ is generated.)
- Option 3: Zero steps are included in the model and counted in the alternating stepping pattern.

Our numerical results show similar trajectories to the previous model with a clear varied step size for the MTBDs (see Figure 6.3). Due to the presence of zero sized steps (option 1), in order to achieve similar results to experiments we needed to take the probability that MTBD E steps set at 84% if the previous step was taken by MTBD D, and 16% otherwise; this results in 82.72% non-passing steps, 74.68% alternating steps and 20.91% backward steps (see Figure 6.4). Approximately 10% of steps by the MTBDs were of a zero step size, the majority of steps were of $8 - 16$nm and

histograms of both forward and backward step distributions (not including zero steps) are given in Figure 6.5.

We explored variations in the probability of backward stepping alongside variations in the maximum separation distance for all three stepping options (see Table 6.4). We see similar results to the previous model (for backward stepping) with a reduction in maximum separation distance reducing the prevalence of non-passing steps and increasing the proportion of backward steps. However, we do see differences in the percentage of alternating steps for the three different options, this count is lower in the case where zero steps exist but are not counted. It is likely that dynein does experience step sizes of 'zero' length, i.e. detaches but rebinds to the same point on the microtubule, but that these would not be picked up by step finding algorithms used in experimental data analysis. This suggests that the coordination between head domains is actually higher in reality than recorded in experiments. It should also be noted that in the case where zero steps are excluded from the model, there is a higher prevalence of backward steps. This is likely to be due to the larger step sizes causing the leading head to move too far ahead of the other head domain and hence more backward steps would be required to keep the complex together. There is no significant difference in the proportion of non-passing steps.

We also explored variations in the probabilities that MTBD E stepped for all three options (with MTBD E more likely to step if MTBD D stepped previously ($P_D \geq 50\%$)), this had a limited effect on the proportion of not passing steps when zero steps were included in the model but no noticeable effect when they were not (see Table 6.5). In all cases backward stepping increased as the likelihood that MTBD E stepped after MTBD D (P_D) fell, as with the previous model. The percentage of alternating steps coincided with the probability that MTBD E stepped after MTBD D as expected when zero steps were either not included or counted. However, they did not coincide when zero steps were not counted and this discrepancy increased as P_D increased. Again, this suggests that if zero steps are present in reality then coordination may be higher than measured experimentally.

6.4 A multi-scale approach for large scale dwelling

Previously, we used a fixed time interval $\frac{T_F}{N}$ for the stepping of a single MTBD, however the unbound stepping of the MTBD should end when the MTBD binds to the microtubule. Consider the interval $[t_i, t_{i+1}] \subset [t_i, t_i + t_{max}]$ where

$$t_{i+1} = \min \left\{ t \in [t_i, t_i + t_{max}] : x_i(t) \geq p_{j+2} \right\}$$

d	P_{Back}	% Not Passing Steps			% Alternating Steps			% Backward Steps		
		1	2	3	1	2	3	1	2	3
40	0	80.40	77.55	80.00	70.01	74.79	74.36	6.16	6.82	6.02
	10	80.64	79.96	78.13	69.60	74.62	73.92	14.00	17.28	14.12
	20	80.09	79.83	79.60	68.47	74.41	73.99	22.24	28.51	22.77
48	0	82.47	81.40	82.89	70.66	74.01	74.18	5.08	5.09	5.17
	5	82.69	82.55	83.06	69.64	73.75	73.88	9.15	10.94	9.11
	10	83.36	81.59	83.01	68.83	73.66	74.13	13.33	15.91	13.48
	15	81.77	81.50	83.07	70.22	73.93	74.66	17.18	21.74	17.57
	20	82.23	81.75	81.84	69.08	74.57	74.16	20.95	27.00	21.15
	25	81.68	82.42	83.83	68.30	74.11	73.79	25.85	33.37	25.48
56	0	84.29	84.27	84.28	69.60	74.52	73.76	4.20	4.54	4.32
	10	84.90	84.29	83.50	68.34	74.06	72.89	12.73	15.21	12.37
	20	85.14	84.01	84.13	68.23	73.64	73.95	20.69	25.19	21.11
64	0	86.95	85.07	86.00	70.72	73.91	74.42	3.48	3.90	3.64
	10	85.16	86.20	85.64	68.77	74.00	74.46	11.29	14.69	11.35
	20	85.10	85.21	85.51	68.98	74.56	73.70	19.74	25.05	19.47
72	0	85.60	85.97	85.47	69.48	73.57	74.36	3.50	3.51	3.13
	10	86.72	86.44	87.27	69.18	74.01	74.18	11.56	14.30	11.79
	20	87.74	87.01	84.42	68.30	74.20	74.14	19.40	24.34	19.21

Table 6.4: Mean percentage of not passing, alternating and backward steps given a range of values for the maximum separation distance d and the probability of random backwards stepping P_{Back}%. The data represents the results of 100 simulations with the probability that MTBD E steps set at 74% if MTBD D stepped previously and 26% otherwise. The mean dwell time is taken to be 2ns. The three options represent the following assumptions: (1) zero steps are included in the model but not counted as part of the alternating stepping pattern; (2) zero steps are not included; (3) zero steps are included in the model and counted in the alternating stepping pattern. If x% of steps are not passing then $1-x$% of steps are passing. Similarly, if x% of steps are alternating then $1-x$% of steps are not alternating.

P_D	P_E	% Not Passing Steps			% Alternating Steps			% Backward Steps		
		1	2	3	1	2	3	1	2	3
50	50	83.85	82.99	83.08	50.81	49.80	50.53	22.90	28.31	23.73
60	40	82.12	83.86	83.04	59.35	60.27	60.44	22.74	27.93	21.94
70	30	82.72	82.08	82.19	65.81	69.99	70.45	21.95	26.53	21.55
80	20	81.69	82.69	81.73	71.57	80.39	79.68	21.96	26.35	21.17
90	10	83.32	82.89	81.96	78.19	90.20	90.05	20.25	26.35	20.11
100	0	82.34	82.26	81.69	84.36	100.00	100.00	19.95	26.75	19.54

Table 6.5: Mean percentage of not passing, alternating and backward steps given a range of values for the stepping probabilities of MTBD E. The data represents the results of 100 simulations with the maximum separation distance set to be 48nm. The probability of random backwards stepping is set to be 12.5% and the mean dwell time is taken to be 2ns. The three options represent the following assumptions: (1) zero steps are included in the model but not counted as part of the alternating stepping pattern; (2) zero steps are not included; (3) zero steps are included in the model and counted in the alternating stepping pattern. If x% of steps are not passing then $1-x$% of steps are passing. Similarly, if x% of steps are alternating then $1-x$% of steps are not alternating.

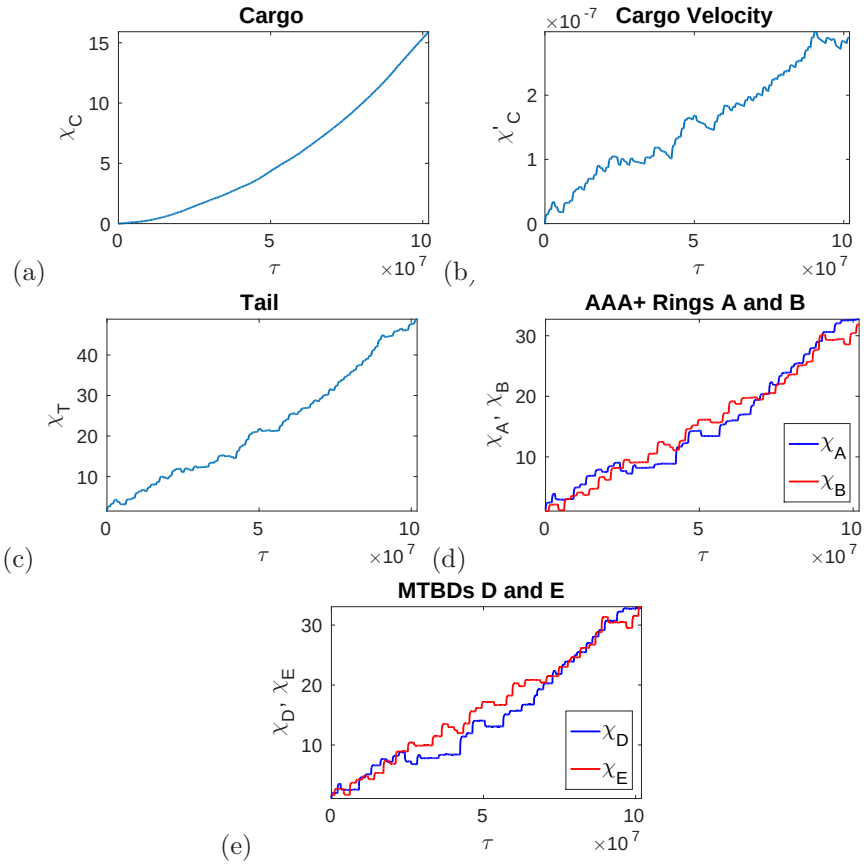

Figure 6.3: Numerical solutions to the model equations (5.10) - (5.13), (6.8) - (6.9) with maximum separation distance between MTBDs at 48nm and the probability that MTBD E steps set at 84% if the previous step was taken by MTBD D, and 16% otherwise. The mean dwell time is taken to be 2ns and the probability of random backward stepping is taken to be 20%. Zero steps were included in the model. Plots over the whole time corresponding to (a) trajectory of the cargo, (b) velocity profile of the cargo, (c) trajectory of the tail domain, (d) trajectories of the AAA+ rings, and (e) trajectories of the MTBDs.

where p_{j+2} is the next binding site for the unbound MTBD i. Hence, the total time spent stepping is given by $T_F = \sum_{i=1}^{N}(t_{i+1} - t_i)$.

6.4.1 Multi-scale non-dimensionalisation

In order to model dwelling over large time scales we take a multi-scale approach by using one time scale for stepping and one for dwelling. We continue to model stepping by the non-dimensional

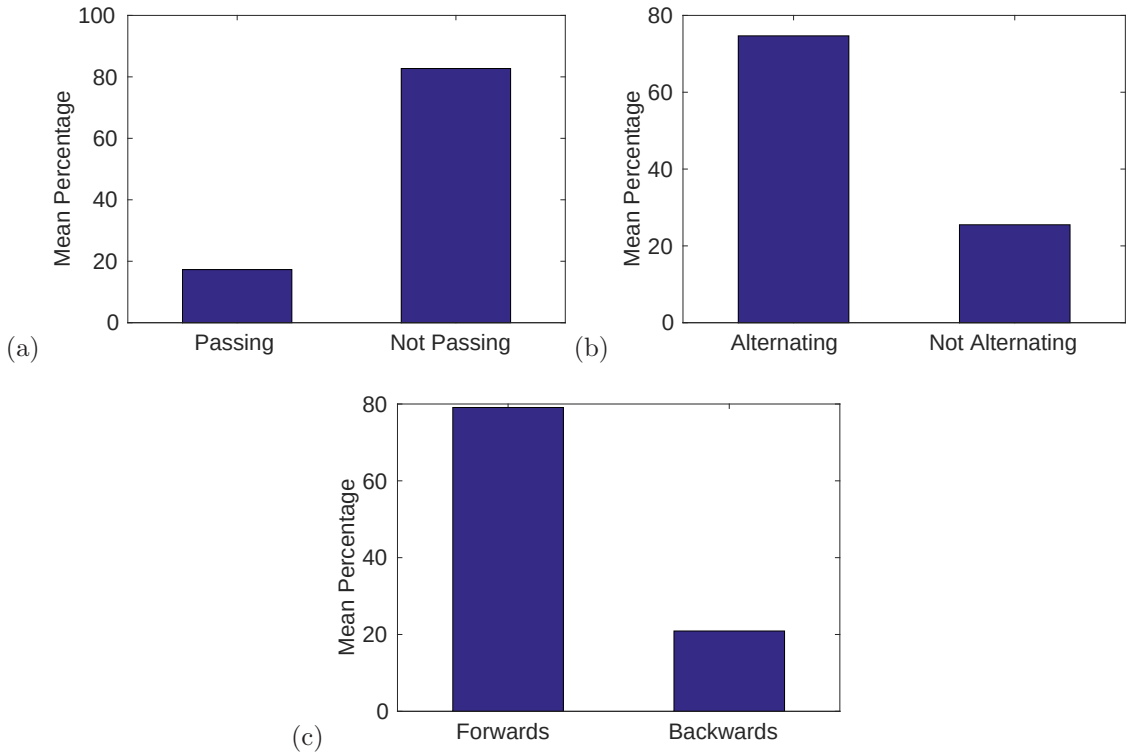

Figure 6.4: Bar charts showing the mean percentage of steps: (a) passing vs not passing, (b) alternating vs not alternating, and (c) forward vs backward. The data represents the results of 1000 simulations with the probability that MTBD E steps set at 84% if MTBD D stepped previously and 16% otherwise. Zero steps were included in the model but not counted as part of the alternating stepping pattern. The maximum separation distance is set to be 48nm, the mean dwell time is 2ns and the probability of random backward stepping is taken to be 20%.

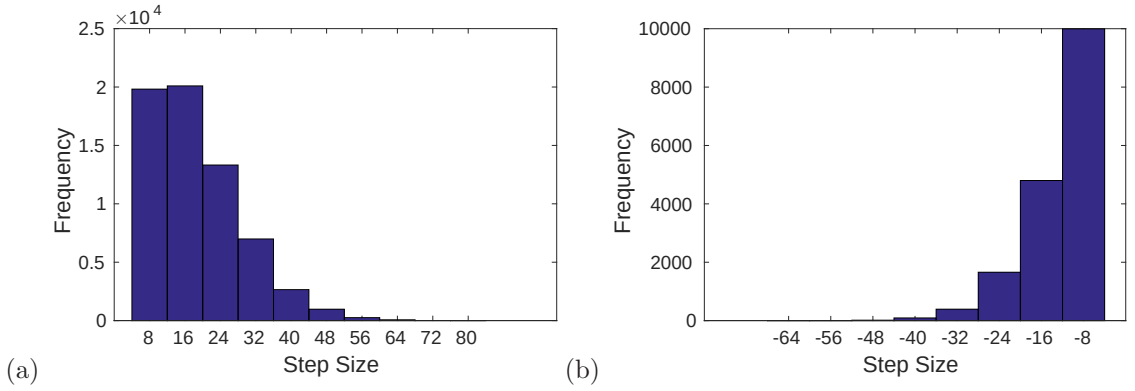

Figure 6.5: Histograms showing the distribution of step sizes: (a) forward steps and (b) backward steps. The data represents the results of 1000 simulations with the probability that MTBD E steps set at 84% if MTBD D stepped previously and 16% otherwise. The maximum separation distance is set to be 48nm, the mean dwell time is 2ns and the probability of random backward stepping is taken to be 20%.

model system as given in Section 6.1 with $h_q = 1$:

$$\alpha_C \frac{d\chi_C}{d\tau_1} = \Big(\frac{1}{\rho_1}\chi_T - 1\Big) - \lambda_1 - \chi_C, \tag{6.10}$$

$$\alpha_T \frac{d\chi_T}{d\tau_1} = \Big(\frac{1}{\rho_2}(\chi_B + \chi_A) - \cos(\theta_{BT}) + \cos(\theta_{AT})\Big) + \rho_1\kappa_1(\chi_C + 1) - (2 + \kappa_1)\chi_T, \tag{6.11}$$

$$\alpha_M \frac{d\chi_A}{d\tau_1} = \rho_2\kappa_2\Big(\chi_T - \cos(\theta_{AT})\Big) + \Big(\chi_D + \cos(\theta_{AD})\Big) - (\kappa_2 + 1)\chi_A, \tag{6.12}$$

$$\alpha_M \frac{d\chi_B}{d\tau_1} = \Big(\chi_E - \cos(\theta_{BE})\Big) + \rho_2\kappa_2\Big(\chi_B + \cos(\theta_{BT})\Big) - (\kappa_2 + 1)\chi_B, \tag{6.13}$$

$$\Big(\alpha_S + \alpha_{ATP}h_{2,D}(\tau_1)\Big)\frac{d\chi_D}{d\tau_1} = h_{2,D}(\tau_1)\Big[\kappa_3\Big(\beta_i + \hat{g}_D(\chi_D, \chi_E, \tau_1)\rho_3\Big) + \Big(\chi_A - \cos(\theta_{AD})\Big) - (1 + \kappa_3)\chi_D\Big], \tag{6.14}$$

$$\Big(\alpha_S + \alpha_{ATP}h_{2,E}(\tau_1)\Big)\frac{d\chi_E}{d\tau_1} = h_{2,E}(\tau_1)\Big[\kappa_3\Big(\beta_{i+1} + \hat{g}_E(\chi_D, \chi_E, \tau_1)\rho_3\Big) + \Big(\chi_B + \cos(\theta_{BE})\Big) - (1 + \kappa_3)\chi_E\Big], \tag{6.15}$$

for the stepping intervals $\tau_1 \in [\tau_{1,i}, \tau_{1,i+1}]$ and with non-dimensional parameter values:

$$\begin{aligned}
&\alpha_C = \frac{\gamma_C\gamma_C}{m_C K_C}, \quad \alpha_T = \frac{\gamma_T\gamma_C}{m_C K_T}, \quad \alpha_M = \frac{\gamma_M\gamma_C}{m_C K_S}, \quad \alpha_S = \frac{\gamma_S\gamma_C}{m_C K_S}, \quad \alpha_{ATP} = \frac{\gamma_{ATP}\gamma_C}{m_C K_S},\\
&\rho_1 = \frac{L_C}{L_T}, \quad \rho_2 = \frac{L_T}{L_S}, \quad \rho_3 = \frac{L_{ATP}}{L_S},\\
&\kappa_1 = \frac{K_C}{K_T}, \quad \kappa_2 = \frac{K_T}{K_S}, \quad \kappa_3 = \frac{K_{ATP}}{K_S},\\
&\beta_i = \frac{p_i}{L_S}, \quad \lambda_1 = \frac{F_C}{K_C L_C}, \quad \delta = \frac{d}{L_S}.
\end{aligned}$$

For the dwelling intervals, the dimensional model is given by:

$$m_C \frac{d^2x_C}{dt^2} = K_C\Big(x_T - x_C - L_C\Big) - F_C - \gamma_C\frac{dx_C}{dt}, \tag{6.16}$$

$$m_T \frac{d^2x_T}{dt^2} = K_T\Big(x_B - x_T - L_T\cos(\theta_{BT})\Big) - K_T\Big(x_T - x_A - L_T\cos(\theta_{AT})\Big) - K_C\Big(x_T - x_C - L_C\Big) - \gamma_T\frac{dx_T}{dt}, \tag{6.17}$$

$$m_M \frac{d^2x_A}{dt^2} = K_T\Big(x_T - x_A - L_T\cos(\theta_{AT})\Big) - K_S\Big(x_A - x_D - L_S\cos(\theta_{AD})\Big) - \gamma_M\frac{dx_A}{dt}, \tag{6.18}$$

$$m_M \frac{d^2x_B}{dt^2} = K_S\Big(x_E - x_B - L_S\cos(\theta_{BE})\Big) - K_T\Big(x_B - x_T - L_T\cos(\theta_{BT})\Big) - \gamma_M\frac{dx_B}{dt}, \tag{6.19}$$

$$\frac{dx_D}{dt} = 0, \tag{6.20}$$

$$\frac{dx_E}{dt} = 0, \tag{6.21}$$

for $t \in [t_{i+1}, t_{i+1} + q_{1,i}]$ where we continue to take $q_{1,i}$ from the exponential distribution with mean μ. Here, $t_{i+1} = \frac{m_C}{\gamma_C}\tau_{1,i+1}$ with $\frac{m_C}{\gamma_C}$ the non-dimensional stepping time characteristic. To non-dimensionalise the dwelling model we continue to use the same spatial characteristics, taking

$x_C = L_C\chi_C$, $x_T = L_T\chi_T$, $x_A = L_S\chi_A$, $x_B = L_S\chi_B$, $x_D = L_S\chi_D$ and $x_E = L_S\chi_E$. For the time characteristic, we scale by the mean dwell time μ, hence $t = \mu\tau_2$. Again, we assume that the acceleration is small and that the dynamics are dominated by the viscous drag, hence the acceleration terms can be neglected and we obtain the following non-dimensional system:

$$\frac{d\chi_C}{d\tau_2} = \mu\Big[\alpha_1\Big(\frac{1}{\rho_1}\chi_T - 1\Big) - \lambda_2 - \alpha_1\chi_C\Big], \tag{6.22}$$

$$\frac{d\chi_T}{d\tau_2} = \mu\Big[\alpha_2\Big(\frac{1}{\rho_2}(\chi_A + \chi_B) + \cos(\theta_{AT}) - \cos(\theta_{BT})\Big) + \alpha_3\rho_1(\chi_C + 1) - (2\alpha_2 + \alpha_3)\chi_T\Big], \tag{6.23}$$

$$\frac{d\chi_A}{d\tau_2} = \mu\Big[\alpha_4\rho_2(\chi_T - \cos(\theta_{AT})) + \alpha_5(\chi_D + \cos(\theta_{AD})) - (\alpha_4 + \alpha_5)\chi_A\Big], \tag{6.24}$$

$$\frac{d\chi_B}{d\tau_2} = \mu\Big[\alpha_5(\chi_E - \cos(\theta_{BE})) + \alpha_4\rho_2(\chi_T + \cos(\theta_{BT})) - (\alpha_4 + \alpha_5)\Big], \tag{6.25}$$

$$\frac{d\chi_D}{d\tau_2} = 0, \tag{6.26}$$

$$\frac{d\chi_E}{d\tau_2} = 0, \tag{6.27}$$

for $\tau_2 \in [\tau_{2,i}, \tau_{2,i+1}]$ with dimensional parameters:

$$\alpha_1 = \frac{K_C}{\gamma_C}, \quad \alpha_2 = \frac{K_T}{\gamma_T}, \quad \alpha_3 = \frac{K_C}{\gamma_T}, \quad \alpha_4 = \frac{K_T}{\gamma_M}, \quad \alpha_5 = \frac{K_S}{\gamma_M},$$
$$\rho_1 = \frac{L_C}{L_T}, \quad \rho_2 = \frac{L_T}{L_S}, \quad \text{and} \quad \lambda_2 = \frac{F_C}{\gamma_C L_C}.$$

As we have used the same spatial non-dimensionalisation, the initial conditions are given by:

$$\begin{cases} \chi_C(\tau_{2,i}) = \chi_C(\tau_{1,i+1}), & \chi_T(\tau_{2,i}) = \chi_T(\tau_{1,i+1}), \quad \chi_A(\tau_{2,i}) = \chi_A(\tau_{1,i+1}), \\ \chi_B(\tau_{2,i}) = \chi_B(\tau_{1,i+1}), & \chi_D(\tau_{2,i}) = \chi_D(\tau_{1,i+1}), \quad \chi_E(\tau_{2,i}) = \chi_E(\tau_{1,i+1}). \end{cases}$$

Similarly the ODE system modelling MTBD stepping following the dwell time will have initial conditions:

$$\begin{cases} \chi_C(\tau_{1,i+1}) = \chi_C(\tau_{2,i+1}), & \chi_T(\tau_{1,i+1}) = \chi_T(\tau_{2,i+1}), \quad \chi_A(\tau_{1,i+1}) = \chi_A(\tau_{2,i+1}), \\ \chi_B(\tau_{1,i+1}) = \chi_B(\tau_{2,i+1}), & \chi_D(\tau_{1,i+1}) = \chi_D(\tau_{2,i+1}), \quad \chi_E(\tau_{1,i+1}) = \chi_E(\tau_{2,i+1}). \end{cases}$$

6.4.2 Multi-scale numerical experiments

The model is solved numerically in MATLAB for $N = 100$ steps using *ode45* for the stepping model and the stiff solver *ode15s* for the dwelling model with the tolerances given in Table 3.2 [164]. The nondimensional systems are solved and then converted back to dimensional results so that they can be presented together on the same time scale. The maximum length of the stepping time

interval is taken to be $\tau_{max} = 10^6$. The primary values are taken as follows: the probability that MTBD E steps given that MTBD D (E) stepped previously is taken to be $P_D = 84\%$ ($P_E = 16\%$), the maximum separation distance is taken to be 48nm and the probability of backward stepping is set to be 20%. The mean dwell time is taken to be $\mu = 2 \times 10^9$ as experimental results have shown the average dwell time for dynein to be 2s [30]. For each step, we take n from the Poisson distribution about 2 to give the step size nL_{ATP} nm for the forward step sizes and n from the Poisson distribution about 1 for the backward steps to give the step size $-nL_{ATP}$ nm. We now assume that zero steps are possible but they are not counted towards alternating or non-alternating steps.

The results show similar profiles for the tail, AAA+ rings and MTBDs, with the increased dwell times between steps, however we see a significant difference for the velocity of the cargo (see Figure 6.6). The cargo now dwells between steps, with an oscillatory velocity profile that returns to zero between steps which is similar to the *in vivo* results by Garrett *et al.,* [2]. Using the primary values for the parameters results in a maximum velocity of the cargo of $15 \times 10^5 nms^{-1}$ and a velocity of up to $2 \times 10^8 nms^{-1}$ for the tail domain. This is much higher than velocities measured experimentally with dynein typically moving at speeds of $600nms^{-1}$ at saturating ATP levels and at room temperature with *in vivo* velocities reaching up to $3\mu ms^{-1}$ in mammalian neurons, although yeast dynein moves at slower speeds of around 50 to $80nms^{-1}$ [84]. A full parameter analysis of all unknown model parameters needs to be conducted in order to establish the parameter set which gives quantitatively accurate values for the velocity for each species and context, and we challenge experimentalists to measure these parameters.

Remark 6.4.1. The statistics for the stepping patterns are similar to the previous model in Section 6.3, with 82.30% not passing steps, 74.74% alternating steps, and 20.64% backward steps (see Figure 6.7). This is to be expected as these statistics reflect the stochastic parameters controlling the stepping of the complex which are unchanged when extending the model to a multi-scale framework.

6.5 Discussion

In this chapter we have extended the mechanical stochastic stepping model to incorporate backward stepping, a variable step size and dwelling over large time scales. The results give trajectories for the complex and cargo that qualitatively match experimental observations.

We have also shown that backward stepping that is directly related to the separation within

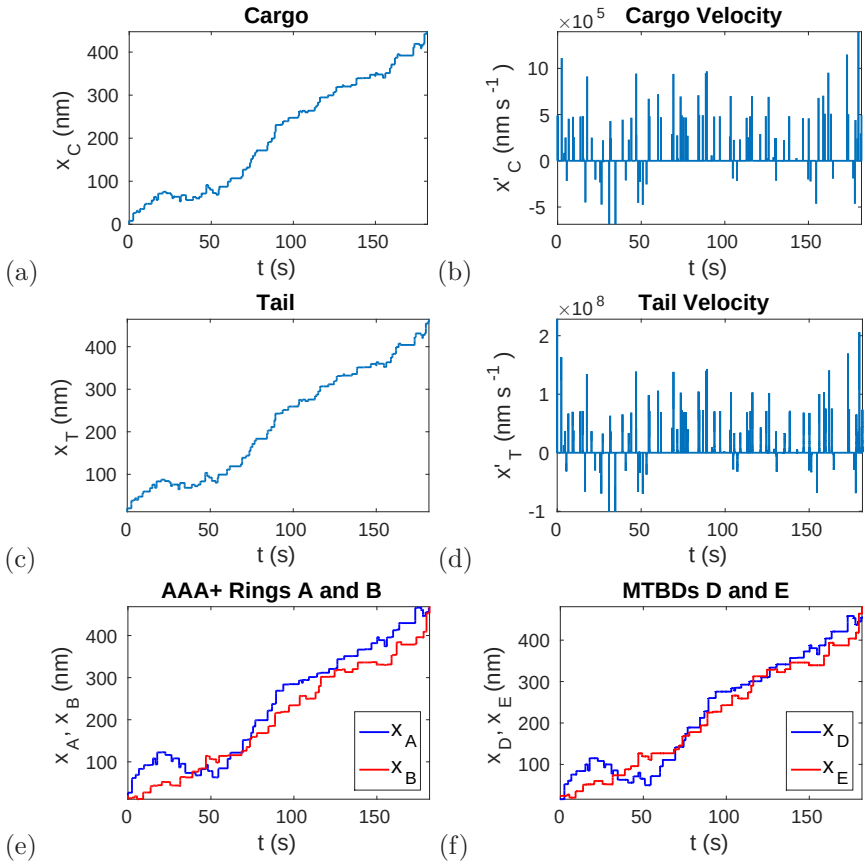

Figure 6.6: Dimensional numerical solutions to the model equations (6.10) - (6.15) and (6.22) - (6.27) with maximum separation distance between MTBDs at 48nm and the probability that MTBD E steps set at 84% if the previous step was taken by MTBD D, and 16% otherwise. Zero steps were included in the model. The mean dwell time is taken to be 2 seconds and the probability of backward stepping is 20%. Plots over the whole time corresponding to (a) trajectory of the cargo, (b) velocity profile of the cargo, (c) trajectory of the tail domain, (d) velocity profile of the tail domain, (e) trajectories of the AAA+ rings, and (f) trajectories of the MTBDs.

the complex cannot account for the high percentages of backward stepping seen experimentally, and hence there must be something else external to this model causing these characteristics. We suggest that the impact of dynactin on the transport mechanisms and the two dimensional nature of dynein need to be explored further with regards to their impact on backward stepping.

By prescribing the levels of coordination within the model we can match experimental observations of the alternating stepping pattern, but when considering the possibility of 'zero' step sizes the model predicts that this coordination must be higher than that seen in experimental observations, as zero steps are not identified in tracking experiments and hence not counted. The model predicts the preference of dynein to the shuffling stepping pattern when the motor is allowed to separate (which is realistic due to the large step sizes seen in experiments), and this matches experimental observations [31, 32]. The model also predicts that species of dynein which prefer a tighter conformation may be more likely to experience backward steps and have a higher prevalence of

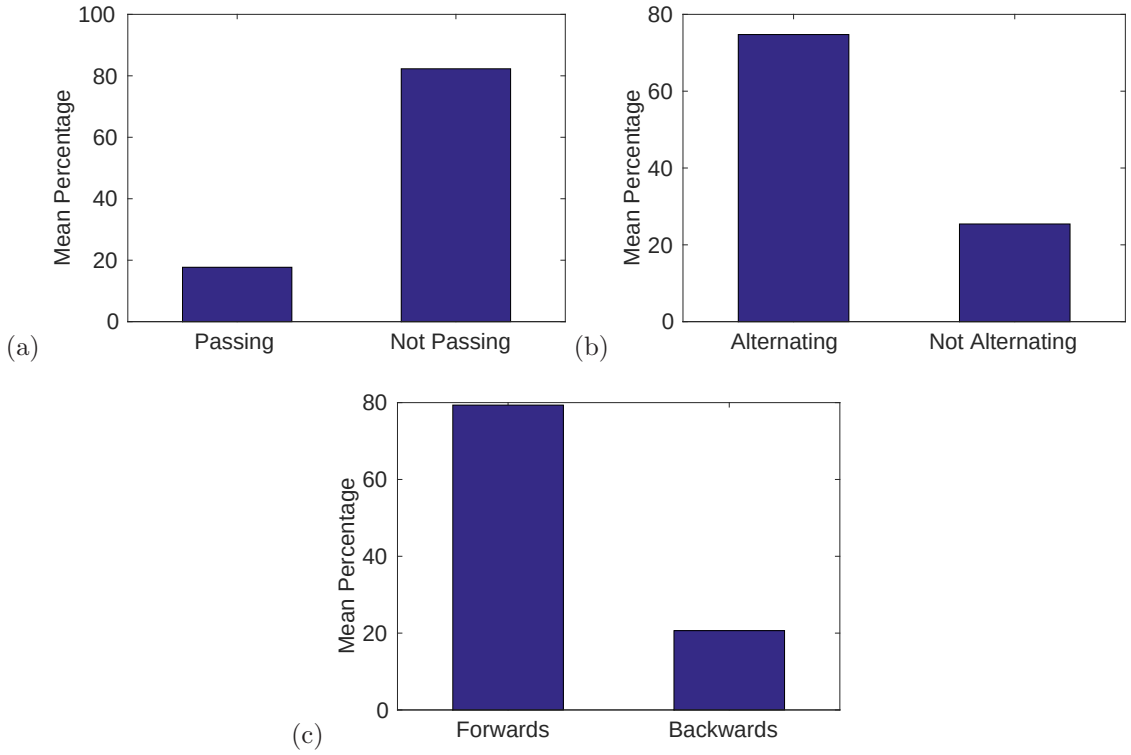

Figure 6.7: Bar charts showing the mean percentage of steps: (a) alternating vs not alternating, (b) passing vs not passing. The data represents the results of 1000 simulations with the probability that MTBD E steps set at 84% if MTBD D had stepped previously and 16% otherwise. Zero steps were included in the model but not counted as part of the alternating stepping pattern. The maximum separation between MTBDs is set to be 48nm and the probability of random backward stepping is 20%.

passing steps. Stronger coordination between the two motor domains could also reduce backward stepping which leads to more efficient stepping as backward steps may be wasteful.

Coordination of the head domains may impact on velocity and run length in ways beyond the simplified model. Our model only considers behaviour when dynein is attached to the microtubule, lack of coordination may lead to detachment from the microtubule thereby decreasing run length and velocity. In the following chapter we consider independent stepping by allowing each head domain to step independently of the state of the other domain.

Chapter 7

ATP Dependent Motion with Independent Head Domains

We have previously assumed some coordination between the two motor domains of dynein, with only one MTBD being able to detach from the microtubule at a time. However, in reality dynein does regularly become completely detached from the microtubule although the conditions under when this occurs are unclear. It has also been proposed that it is the coordination between the two motor domains that keeps the complex attached to the microtubule so that the long processive runs seen in experiments can be achieved. We therefore investigate the scenario where there is no coordination between the two motor domains to test this hypothesis, assuming that the motor domains bind ATP randomly and the MTBDs can detach irrespective of the ATP cycle of the other motor domain.

7.1 Stochastic stepping

The dwell time before the binding of ATP for each motor domain is modelled by the exponential distribution (see Remark 7.1.1). We assume that these waiting times for each motor domain are independent of each other and are given by $\mathbf{q_D} = \{q_D^i\}_{i\in\mathbb{N}}$ for MTBD D and $\mathbf{q_E} = \{q_E^i\}_{i\in\mathbb{N}}$ for MTBD E with q_D^i and q_E^i taken from the exponential distribution with mean dwell time μ. The system continues to be modelled by equations (5.4) - (5.7), with different stepping functions to h_D, h_E in equations (5.8) - (5.9). For MTBD D we assume that it steps after q_D^i seconds, hence

we define the following step function:

$$h_{4,D}(t, \mathbf{q_D}) = \begin{cases} 1 & \text{if} \quad t \in [t_i + q_D^i, t_{i+1}] \\ 0 & \text{if} \quad t \in [t_i, t_i + q_D^i] \end{cases}$$

where t_i and t_{i+1} are the times when MTBD D binds back on to the microtubule after stepping with t_0 the initial time. The stepping function for MTBD E can be defined similarly:

$$h_{4,E}(t, \mathbf{q_E}) = \begin{cases} 1 & \text{if} \quad t \in [t_j + q_E^i, t_{j+1}] \\ 0 & \text{if} \quad t \in [t_j, t_j + q_E^i] \end{cases}$$

with t_j and t_{j+1} the times when MTBD E binds to the microtubule. Here, t_j denotes different time intervals to t_i. Therefore, the ODEs for MTBDs D and E become:

$$\begin{aligned} m_S h_{4,D}(t, \mathbf{q_D}) \frac{d^2 x_D}{dt^2} = h_{4,D}(t, \mathbf{q_D}) \Big[&- \gamma_{ATP} \frac{dx_D}{dt} - K_{ATP}(x_D - p_i - nL_{ATP}) \\ &- K_S(x_D - x_A + L_S \cos(\theta_{AD})) \Big] - \gamma_S \frac{dx_D}{dt}, \end{aligned} \tag{7.1}$$

$$\begin{aligned} m_S h_{4,E}(t, \mathbf{q_E}) \frac{d^2 x_E}{dt^2} = h_{4,E}(t, \mathbf{q_E}) \Big[&- \gamma_{ATP} \frac{dx_E}{dt} - K_{ATP}(x_E - p_{i+1} - nL_{ATP}) \\ &- K_S(x_E - x_B - L_S \cos(\theta_{BE})) \Big] - \gamma_S \frac{dx_E}{dt}, \end{aligned} \tag{7.2}$$

for $t \in [0, T_{Final}]$.

Remark 7.1.1. Experimental observations suggest that the dwell times of tail labelled dynein can be well fit by an exponential distribution and have average dwell times of 2s per ATP cycle, whilst head labelled dynein dwell times are a convolution of two exponential distributions [30, 31]. As we are assuming independent head domains, we use a single exponential distribution for each head domain with identical mean dwell times. However, this work could be extended to explore different mean dwell times fit to more complex distributions in order to study interhead coordination and different characteristics of leading and lagging heads.

7.1.1 Multi-scale non-dimensionalisation

We take a multi-scale approach when non-dimensionalising the model, using one fast time scale for the stepping and one slow time scale for the dwelling, similarly to the previous chapter. For

the dwelling interval, we non-dimensionalise the system as in Section 6.4.1 with $t_c = \mu$:

$$\frac{d\chi_C}{d\tau_1} = \mu\Big[\alpha_1\Big(\frac{1}{\rho_1}\chi_T - 1\Big) - \lambda_2 - \alpha_1\chi_C\Big], \tag{7.3}$$

$$\frac{d\chi_T}{d\tau_1} = \mu\Big[\alpha_2\Big(\frac{1}{\rho_2}(\chi_A + \chi_B) + \cos(\theta_{AT}) - \cos(\theta_{BT})\Big) + \alpha_3\rho_1(\chi_C + 1) - (2\alpha_2 + \alpha_3)\chi_T\Big], \tag{7.4}$$

$$\frac{d\chi_A}{d\tau_1} = \mu\Big[\alpha_4\rho_2(\chi_T - \cos(\theta_{AT})) + \alpha_5(\chi_D + \cos(\theta_{AD})) - (\alpha_4 + \alpha_5)\chi_A\Big], \tag{7.5}$$

$$\frac{d\chi_B}{d\tau_1} = \mu\Big[\alpha_5(\chi_E - \cos(\theta_{BE})) + \alpha_4\rho_2(\chi_T + \cos(\theta_{BT})) - (\alpha_4 + \alpha_5)\Big], \tag{7.6}$$

$$\frac{d\chi_D}{d\tau_1} = 0, \tag{7.7}$$

$$\frac{d\chi_E}{d\tau_1} = 0, \tag{7.8}$$

for $\tau_1 \in [\tau_{1,k}, \tau_{1,k+1}]$ where $\tau_{1,k+1} = \tau_{1,k} + \frac{1}{\mu}q_j^i$ for $j = D$ or $j = E$. Note that the time intervals associated with stepping will depend on the random vectors $\mathbf{q_D}$ and $\mathbf{q_E}$ and will be discussed in more detail below in Section 7.2. For the stepping intervals we take $t_c = \frac{m_C}{\gamma_C}$ the system of ODEs is given as:

$$\alpha_C\frac{d\chi_C}{d\tau_2} = \Big(\frac{1}{\rho_1}\chi_T - 1\Big) - \lambda_1 - \chi_C, \tag{7.9}$$

$$\alpha_T\frac{d\chi_T}{d\tau_2} = \Big(\frac{1}{\rho_2}(\chi_B + \chi_A) - \cos(\theta_{BT}) + \cos(\theta_{AT})\Big) + \rho_1\kappa_1(\chi_C + 1) - (2 + \kappa_1)\chi_T, \tag{7.10}$$

$$\alpha_M\frac{d\chi_A}{d\tau_2} = \rho_2\kappa_2\Big(\chi_T - \cos(\theta_{AT})\Big) + \Big(\chi_D + \cos(\theta_{AD})\Big) - (\kappa_2 + 1)\chi_A, \tag{7.11}$$

$$\alpha_M\frac{d\chi_B}{d\tau_2} = \Big(\chi_E - \cos(\theta_{BE})\Big) + \rho_2\kappa_2\Big(\chi_B + \cos(\theta_{BT})\Big) - (\kappa_2 + 1)\chi_B, \tag{7.12}$$

$$\begin{aligned}\Big(\alpha_S + \alpha_{ATP}h_{4,D}(\tau_2, \mathbf{q_D})\Big)\frac{d\chi_D}{d\tau_2} = h_{4,D}(\tau_2, \mathbf{q_D})\Big[\kappa_3(\beta_i + n\rho_3) \\ + \Big(\chi_A - \cos(\theta_{AD})\Big) - (1 + \kappa_3)\chi_D\Big],\end{aligned} \tag{7.13}$$

$$\begin{aligned}\Big(\alpha_S + \alpha_{ATP}h_{4,E}(\tau_2, \mathbf{q_E})\Big)\frac{d\chi_E}{d\tau_2} = h_{4,E}(\tau_2, \mathbf{q_E})\Big[\kappa_3(\beta_{i+1} + n\rho_3) \\ + \Big(\chi_B + \cos(\theta_{BE})\Big) - (1 + \kappa_3)\chi_E\Big],\end{aligned} \tag{7.14}$$

for $\tau_2 \in [\tau_{2,k}, \tau_{2,k+1}]$, where $\tau_{2,k} = \frac{m_C}{\gamma_C}\tau_{1,k+1}$, and with non-dimensional parameter values:

$$\begin{aligned}&\alpha_C = \frac{\gamma_C\gamma_C}{m_CK_C}, \quad \alpha_T = \frac{\gamma_T\gamma_C}{m_CK_T}, \quad \alpha_M = \frac{\gamma_M\gamma_C}{m_CK_S}, \quad \alpha_S = \frac{\gamma_S\gamma_C}{m_CK_S}, \quad \alpha_{ATP} = \frac{\gamma_{ATP}\gamma_C}{m_CK_S}, \\ &\rho_1 = \frac{L_C}{L_T}, \quad \rho_2 = \frac{L_T}{L_S}, \quad \rho_3 = \frac{L_{ATP}}{L_S}, \\ &\kappa_1 = \frac{K_C}{K_T}, \quad \kappa_2 = \frac{K_T}{K_S}, \quad \kappa_3 = \frac{K_{ATP}}{K_S}, \\ &\beta_i = \frac{p_i}{L_S}, \quad \lambda_1 = \frac{F_C}{K_CL_C}.\end{aligned}$$

7.2 Numerical experiments

Numerical simulations are run in MATLAB using the solver *ode15s* for the dwelling period and *ode45* for the stepping intervals with tolerances given in Table 3.2 [164]. Due to the independence of the two MTBDs, both MTBDs could become detached from the microtubule, if this occurs then we end our simulation, recording the number of steps and the run length. Initially we consider forward stepping with a fixed step size, taking $n = 2$ to give a step size of 16nm. We consider a maximum of $N = 100$ steps with mean dwell time of $\mu = 2$s for each head domain. The initial dwell times q_D^1, q_E^1 are generated and the system is set to dwell for $\tau \in [0, \frac{1}{\mu}\min\{q_D^1, q_E^1\}]$, hence the system is solved for the initial conditions (5.16).

If $q_D^1 < q_E^1$ the system is then solved for MTBD D unbound for $\tau \in [\frac{\gamma_C}{m_C}q_D^1, \min\{\frac{\gamma_C}{m_C}q_E^1, \frac{\gamma_C}{m_C}q_D^1 + T_{step}\}]$ where we take $T_{Step} = 10^6$. This is necessary as the ODE system will become stiff if the time scales are too large. The initial conditions are taken to be those at the end of the dwelling interval:

$$\chi_C(\tau_{2,k}) = \chi_C(\tau_{1,k+1}), \quad \chi_T(\tau_{2,k}) = \chi_T(\tau_{1,k+1}), \quad \chi_A(\tau_{2,k}) = \chi_A(\tau_{1,k+1}),$$
$$\chi_B(\tau_{2,k}) = \chi_B(\tau_{1,k+1}), \quad \chi_D(\tau_{2,k}) = \chi_D(\tau_{1,k+1}), \quad \chi_E(\tau_{2,k}) = \chi_E(\tau_{1,k+1}),$$

for $\tau_{1,k+1} = \frac{1}{\mu}\min\{q_D^1, q_E^1\}$ and $\tau_{2,k} = \frac{\gamma_C}{m_C}q_D^1$. The solution is then truncated to the point when the MTBD reaches the binding site, time t_{bind}, a new dwell time q_D^2 is generated and we compare this dwell time with $q_E^1 - t_{bind}$. If the MTBD does not reach the binding site within the time interval, i.e. the other MTBD detaches early, then the simulation is ended. The system is solved similarly for the case $q_D^1 > q_E^1$ but with MTBD E unbound and $\tau_{2,k} = \frac{\gamma_C}{m_C}q_E^1$. This process is repeated until there have been $N = 100$ steps or both MTBDs have detached.

Example trajectories are plotted in Figure 7.1 with stepping statistics for optimal parameter values plot in Figure 7.2. The steps taken by the MTBDs can be seen to move through the system to the cargo, with clear stepping by both the cargo and the tail domain, and the variable dwell times can also be observed (see Figure 7.1).

By analysing the stepping behaviour of this model we see that for larger values of K_{ATP}, in the 400 to 1000 range in Table 7.1, we achieve 83.63% to 86.97% not passing steps on average which is close to the 83% seen in experiments. However, all values of K_{ATP} in Table 7.1 give much lower values for the average percentage of alternating steps than seen in experiments (predominantly around 50% compared to 74%). This suggests that this independent form of stepping cannot account for the alternating stepping patterns seen in experiments and hence there must be some

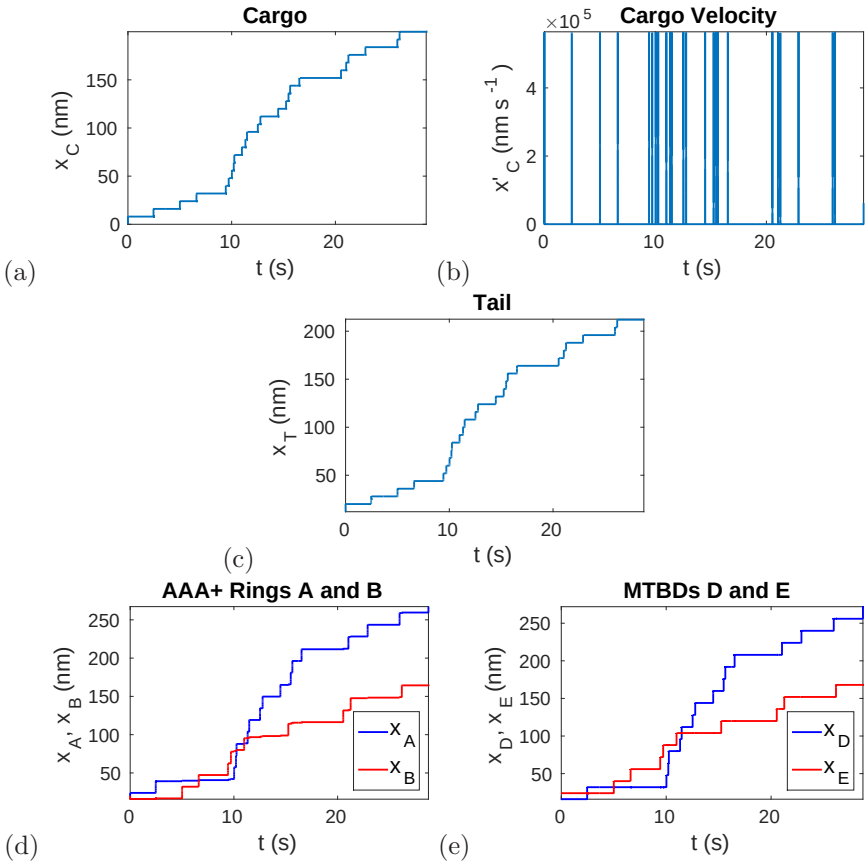

Figure 7.1: Dimensional numerical solutions to the model equations (7.3) - (7.8) and (7.9) - (7.14) with fixed step size ($n = 2$) forwards and parameters $K_{ATP} = 500$, $\gamma_{ATP} = 10$ with all other parameters taken to be at their primary values given in Table 5.1. Plots over the whole time corresponding to (a) trajectory of the cargo, (b) velocity profile of the cargo, (c) trajectory of the tail domain, (d) trajectories of the AAA+ rings, and (e) trajectories of the MTBDs.

form of coordination acting between the two head domains to account for this behaviour.

Variations in the values of K_{ATP} show that run lengths are highly dependent on this parameter (see Table 7.2). We see that for $K_{ATP} = 10$ and $K_{ATP} = 100$ the mean number of steps in a run is less than one, suggesting that most times the run is terminated before the first step can be completed (see Table 7.1). Processivity is therefore dependent on the value of K_{ATP}, although this parameter cannot be directly measured in experiments as it is an approximation of the effects of the ATP force, it suggests that if the ATP cycle of the detached head domain is not completed quickly enough, then an uncoordinated detachment of the attached MTBD is likely to occur and hence the run will be terminated after fewer steps. The optimum value for this parameter is $K_{ATP} \approx 500$ to give a mean number of steps of 33.50 and mean run lengths of 275.95nm for the cargo and 276.69nm for the tail domain (see Tables 7.1 and 7.2). Although $K_C = 550$ gives the highest run lengths, these run lengths are still much lower than seen in experiments, with typical run lengths of 800nm and 1.5μm measured for murine and bovine dynein *in vitro* [84]. This suggests that although some

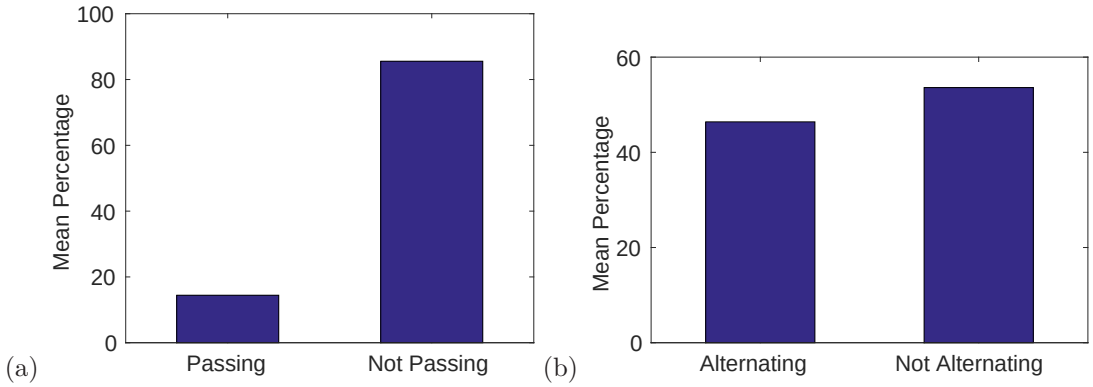

Figure 7.2: Bar charts showing the mean percentage of steps: (a) passing vs not passing, and (b) alternating vs not alternating. The data represents the results of 100 simulations with $K_{ATP} = 500$ and $\gamma_{ATP} = 10$.

K_{ATP}	γ_{ATP}	% Not Passing Steps	% Alternating Steps	Mean Number of Steps
10	10	100	0*	0.36
100	10	100	33.60	0.75
250	10	46.80	66.08	9.56
400	10	83.63	43.89	29.28
500	10	85.56	46.40	33.50
550	10	85.19	50.49	33.37
600	10	86.97	49.22	30.99
750	10	86.39	50.40	27.65
1000	10	84.56	48.07	22.92
500	1	85.06	47.12	32.90
500	10	85.56	46.40	33.50
500	100	84.52	43.58	26.71
500	1000	78.55	46.11	14.84

Table 7.1: Mean percentage of not passing and alternating steps, and mean number of steps in a run given a range of values for the parameters K_{ATP} and γ_{ATP}. The data represents the results of 100 simulations with a mean dwell time of $\mu = 2$s. If x% of steps are not passing then $1 - x$% of steps are passing. Similarly, if x% of steps are alternating then $1 - x$% of steps are not alternating; except for the case labelled * where the number of steps in a run were always less than or equal to one and hence neither alternating or non-alternating steps were present.

processivity can be achieved with independent head domains, coordination is important to obtain the higher run lengths that are seen in experiments. However, the measured run lengths are close to the run lengths of murine dynein in the absence of dynactin measured to be approximately 300nm [84, 35] which may suggest that dynactin has an effect on the coordination of the motor or influences the motor in another way which we have not accounted for in the model.

Variations in γ_{ATP} have little effect on the percentage of not passing and alternating steps, however they do have an effect on run length, with an increase in $\gamma_{ATP} > 10$ leading to a fall in the mean number of steps in a run and lower run length for all variables (see Tables 7.1 and 7.2).

K_{ATP}	γ_{ATP}	Cargo	Tail
10	10	10.96	15.54
100	10	14.09	19.12
250	10	84.52	88.87
400	10	242.20	243.79
500	10	275.95	276.69
550	10	277.54	277.79
600	10	255.87	255.95
750	10	229.17	229.18
1000	10	191.34	191.34
500	1	271.15	271.69
500	10	275.95	276.69
500	100	221.65	222.60
500	1000	126.70	129.37

Table 7.2: Mean run lengths in nanometres for the cargo and tail domain given a range of values for the parameters K_{ATP} and γ_{ATP}. The data represents the results of 100 simulations with a mean dwell time of $\mu = 2$s. If x% of steps are not passing then $1 - x$% of steps are passing. Similarly, if x% of steps are alternating then $1 - x$% of steps are not alternating.

7.2.1 Variable step size with backward stepping

We extend the model to include a variable step size and random backward stepping. The step size is taken to be nL_{ATP} nm where n is taken from the Poisson distribution about 2 for forward steps, giving a predominant step size of 16nm, and $-n$ is taken from the Poisson distribution about 1 for a backward step to give a step size of -8nm. Steps of 'zero ' length are excluded although can easily be included in the model. Random backward stepping is determined by a predetermined value for the probability of backward stepping P_{Back} and a step is set to move backwards if $q_{Back} < P_{Back}$ where q_{Back} is taken from the uniform distribution on $(0, 1)$ for each step. An example plot of the trajectories is given in Figure 7.3, here we can clearly see backward stepping by the MTBDs which feeds through the system resulting in backward steps by the tail domain and cargo.

The addition of a variable step size does appear to reduce the number of steps in a run, from an average of 33.50 to 19.29 (see Tables 7.1 and 7.3), and also sees a reduction in run length, with the average run length of the cargo reducing from 275.95nm to 182.23nm (see Tables 7.2 and 7.4). The mean number of steps in a run and the average run length can be increased by increasing the parameter K_{ATP} to 750 MDa ns^{-2} (see Tables 7.3 and 7.4), however these values are still lower than with fixed step sizes. This reduction in run length may be caused by a larger increase in smaller step sizes (shorter than 16nm) in comparison to the prevalence of larger step sizes (longer than 16nm). However, a reduction in the mean number of steps in a run is an unexpected result. This may be due to larger steps taking longer for the MTBD to reattach and hence the other MTBD may be more likely to detach from the microtubule during these steps. This effect is only likely to occur in reality if the two head domains of dynein are truly independent of each other.

The addition of backward stepping increases the mean number of steps in a run however it reduces the mean run length in comparison to a model with variable step sizes (see Tables 7.5 and 7.6). The reduction in mean run length is to be expected as the increased prevalence of backward steps will delay the complex from progressing along the microtubule. The increase in the mean number of steps was not expected. This may be due to an increase in the prevalence of smaller steps, with backward steps modelled to be predominantly 8nm whilst forward steps are predominantly 16nm. These smaller steps may attach back on to the microtubule more quickly, making it less likely that the other head domain will detach whilst the other head domain is completing a step and therefore detached, terminating a run. We note that the mean number of steps in a run is still significantly lower than for the model of forward stepping with fixed step size.

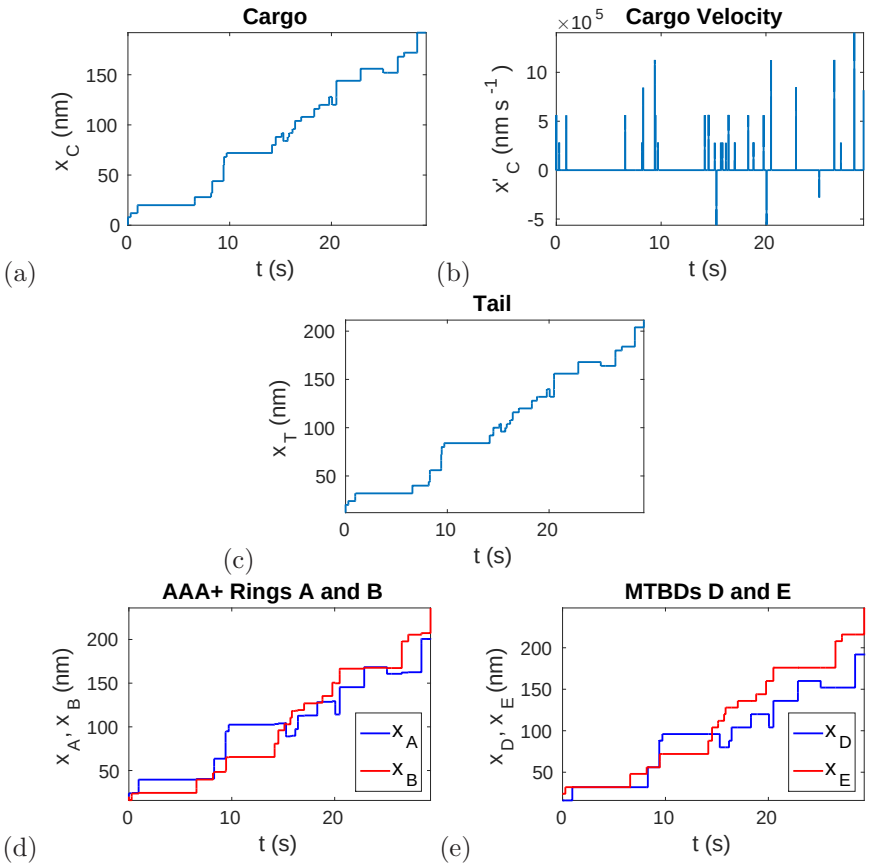

Figure 7.3: Dimensional numerical solutions to the model equations (7.3) - (7.8) and (7.9) - (7.14) with a variable step size ($+n$ taken from the Poisson distribution about 2 and $-n$ taken from the Poisson distribution about 1). The probability of random backward stepping is set to be 10%. Plots over the whole time corresponding to (a) trajectory of the cargo, (b) velocity profile of the cargo, (c) trajectory of the tail domain, (d) trajectories of the AAA+ rings, and (e) trajectories of the MTBDs.

K_{ATP}	γ_{ATP}	% Not Passing Steps	% Alternating Steps	Mean Number of Steps
250	10	74.53	60.76	7.38
500	10	77.70	42.32	19.29
750	10	85.95	48.79	22.41
1000	10	84.50	51.36	18.80
500	1	78.92	45.16	20.71
500	10	77.70	42.32	19.29
500	100	78.87	45.51	18.38
500	1000	79.51	50.15	11.48

Table 7.3: Mean percentage of not passing and alternating steps, and mean number of steps in a run given a range of values for the parameters K_{ATP} and γ_{ATP}. The data represents the results of 100 simulations with a mean dwell time of $\mu = 2$s. If x% of steps are not passing then $1 - x$% of steps are passing. Similarly, if x% of steps are alternating then $1 - x$% of steps are not alternating; except for the case labelled * where the number of steps in a run were always less than or equal to one and hence neither alternating or non-alternating steps were present.

K_{ATP}	γ_{ATP}	Cargo	Tail
250	10	71.61	78.56
500	10	182.23	185.29
750	10	216.31	216.80
1000	10	186.40	186.49
500	1	193.62	196.30
500	10	182.23	185.29
500	100	175.45	178.46
500	1000	112.12	117.54

Table 7.4: Mean run lengths in nanometres for the cargo and tail domain given a range of values for the parameters K_{ATP} and γ_{ATP}. The data represents the results of 100 simulations with a mean dwell time of $\mu = 2$s. If x% of steps are not passing then $1 - x$% of steps are passing. Similarly, if x% of steps are alternating then $1 - x$% of steps are not alternating.

p_{Back}	% Not Passing Steps	% Alternating Steps	Mean Number of Steps
0	77.70	42.32	19.29
10	79.80	46.71	20.64
20	80.09	45.81	24.19

Table 7.5: Mean percentage of not passing and alternating steps, and mean number of steps in a run given a range of values for the probability of backward stepping. The data represents the results of 100 simulations with a mean dwell time of $\mu = 2$s, $K_{ATP} = 500$ and $\gamma_{ATP} = 10$. If x% of steps are not passing then $1 - x$% of steps are passing. Similarly, if x% of steps are alternating then $1 - x$% of steps are not alternating; except for the case labelled * where the number of steps in a run were always less than or equal to one and hence neither alternating or non-alternating steps were present.

P_{Back}	Cargo	Tail
0	182.23	185.29
10	169.98	171.63
20	158.22	159.34

Table 7.6: Mean run lengths in nanometres for the cargo and tail domain given a range of values for the probability of backward stepping. The data represents the results of 100 simulations with a mean dwell time of $\mu = 2$s, $K_{ATP} = 500$ and $\gamma_{ATP} = 10$. If $x\%$ of steps are not passing then $1 - x\%$ of steps are passing. Similarly, if $x\%$ of steps are alternating then $1 - x\%$ of steps are not alternating.

7.3 Discussion

We have been able to model uncoordinated motion and have shown that dynein can still achieve some level of processivity through this mechanism although it can not achieve the high run lengths observed in experiments. We do however, achieve run lengths close to those seen for murine dynein in the absence of dynactin, when using a fixed forward stepping pattern [35, 84]. This may suggest that either dynactin has some influence on the coordination of the motor domains or that we need to account for the effect of dynactin in our model in another way.

Loa mutants in mice have been shown to exhibit shorter run lengths than wildtype complexes [2, 3, 35, 36]. Ori-McKenney *et al.,* measure run lengths of 259nm for *Loa*+/− mutants and 175nm for *Loa*−/− mutants and we are able to achieve similar run lengths by our choice of parameters and stepping patterns [35]. Ori-McKenney *et al.,* suggest that the *Loa* mutation may cause altered coordination in the motor domain of dynein [35]. Our results also suggest that it may be possible that this mutation disrupts the coordination within the complex leading to more frequent detachment of the motor from the microtubule and shorter run lengths. Deng *et al.,* have shown that the *Loa* mutation causes dynein to have a lower affinity to dynactin, and so it may be through this disruption that the mutation affects the transport mechanisms of dynein [37].

We have also shown that when using this mode of stepping, there is unlikely to be a preference for either an alternating or non-alternating stepping pattern, which suggests that the alternating stepping patterns seen for yeast dynein by Qiu *et al.,* and DeWitt *et al.,* must have arisen through some form of coordination within the complex [31, 32].

The mean dwell times for each head domain are assumed to be equivalent, however it would be interesting to investigate the effect of differences in these dwell times. In particular, allowing the lagging and leading heads to have different dwell times may encourage a more coordinated stepping pattern and experiments have shown that the lagging and leading heads have different stepping characteristics [31, 32]. Currently, the motor domain can diverge as we assume that once

the MTBD is bound it is bound until a chemical change from ATP hydrolysis occurs, it would therefore be interesting to introduce the effect of forces on detachment in this model. It has been shown by Gennerich *et al.,* that dynein can walk through applied force alone and so these forces are important to the model [66].

Chapter 8

Conclusions and Future Work

Cytoplasmic dynein 1 is a motor protein that is crucial for many cellular activities and its malfunction has been implicated in neurodegenerative and neurodevelopmental diseases [1, 3, 2, 4, 5]. Developing a complete understanding of its mechanics is therefore important in order to understand these cellular processes and to discover potential medical solutions to manage these diseases. Relatively few models studying dynein's mechanism have been developed, with the main focus being on the chemical cycle [150, 151, 152, 153, 154, 155]. Although some intracellular transport models have been developed with a specific focus on dynein, they do not consider the intrinsic mechanisms employed by dynein [94, 110, 111]. Therefore, we set out to develop a mathematical model from a mechanistic approach in order to study the transport mechanisms of cytoplasmic dynein that could be used to study the mechanistic effects of mutations.

In this study we have derived a general integrative mechanical model that describes the transport mechanisms of cytoplasmic dynein 1. We initially considered a continuous model of transport by dynein undergoing continual stepping along the microtubule in the minus end direction. We were able to obtain either shuffling or hand-over-hand stepping patterns by the choice of functions and parameter values. The model predicts that the relative forces of the two head domains can determine the stepping pattern. This suggests that if one head domain is mutated to reduce its ATPase activity or causes it to bind weakly to the microtubule, then the stepping profile exhibits shuffling as opposed to hand-over-hand stepping.

The model was then developed to incorporate stochasticity in order to reflect the random binding of ATP and random stepping behaviour. The stochastic model is able to describe the shuffling stepping profile as an emergent process, reflecting the experimental observations seen in

the literature [31, 32]. The model also predicts that this pattern is only exhibited when the two head domains are allowed to separate over large distances, and that when dynein is fixed in a tighter conformation the prevalence of both passing and backward steps increases.

We have investigated different levels of interhead coordination within the model framework and shown that this is essential in order to achieve the long run lengths and alternating stepping patterns seen in experiments [31, 32, 84]. We also suggest that the levels of coordination seen in experiments will be higher in reality due to the presence of steps of 'zero' length, i.e. detach and reattach at the same point on the microtubule, as these are not considered in step tracking experiments [31, 32]. Significantly, allowing the head domains to step independently results in run lengths similar to those exhibited by *Loa* mutants, which supports the hypothesis by Ori-McKenney *et al.,* that the mutation affects the coordination between the motor domains of dynein [35]. In the absence of a variable step size and backward stepping, we are also able to achieve run lengths seen for murine dynein in the absence of dynactin, which suggests that dynactin could play a role in coordinating the two head domains. This would support the findings of Deng *et al.,* [37] who found that the *Loa* mutation caused a lower affinity of dynein to dynactin, hence the lower run lengths seen for *Loa* dynein could also be caused by a lower affinity to dynactin [2, 3, 35, 36].

We note that our stepping parameters are based on yeast dynein, and so the stepping behaviour of mammalian dynein may be significantly different. It would therefore be beneficial to our modelling for experimentalists to categorise the different stepping behaviours of different species. However, our modelling can be used to predict these behaviours and future work could involve testing combinations of different distributions of step sizes, proportions of backward stepping, and dwell times in order to predict the likely behaviours of different species according to existing knowledge of their behaviour.

Quantitative comparisons for agreement will require experiments to be carried out on the whole dynein structure to provide modelling with detailed experimental values. This requires experimentalists to design new whole-structure experiments that would aid substantially model refinement and prediction. Parameter optimisation methods may need to be carried out on the given model in order to find appropriate parameter values to achieve the velocities seen in experiments for each of the species and various truncated forms of dynein, both for *in vivo* and *in vitro* experiments.

Variable dwell times for each head domain have been implemented in a model for independent stepping, however extending this model to include some coordination within the dwell times may be beneficial. It is unclear whether dynein's coordination occurs through a gating mechanism, which would prohibit detachment from the microtubule whilst the other head domain is detached (as we

have modelled), or through another mechanism such as a high duty ratio (reviewed in [28, 41, 72]). Hence, exploring these possible mechanisms further could enhance current understanding. Leading and lagging head domains have been shown to exhibit different stepping characteristics [31, 32], this could be incorporated into the model through distinct dwell times and other parameters.

The model is limited in its description of variable step sizes and backward stepping as random processes, and extensions to the model need to be incorporated in order to investigate the mechanics of these phenomena. The influence of dynactin and other regulatory and accessory proteins could also be considered. The three-dimensional nature of the dynein complex needs to be explored further, to investigate how the angle of the stalk and positions of the AAA+ rings play a role in the stepping direction of the motor. Future work to introduce the possibility of strain dependent movement in the model would be beneficial, as the strain within the complex may influence the step size. This would allow a more accurate representation of dynein stepping as the strain within the complex may cause a motor domain to detach independently of ATP. These forces may be significant as Gennerich *et al.,* have shown that dynein can walk through applied force alone [66].

In conclusion, we have derived a general mechanistic model from first principles to describe the stepping behaviour of dynein attached to a cargo. We have been able to describe the behaviour of the whole structure, including the MTBDs which are technically challenging to observe in experiments. The model is used to make several significant predictions about how differences within the complex may result in different stepping patterns, the impact of coordination, and how mutation may effect the stepping ability. We hope that experimentalists can use our model to make new predictions and design new experiments in order to validate the current model predictions. Further development of the model could also lead to valuable insight on how dynein achieves a variable step size and backward stepping which are currently open questions within the literature. Future work will investigate the effects of variable dwell times and strain dependent stepping to establish a complete model which incorporates all aspects of the transport mechanisms for cytoplasmic dynein 1. Therefore, this work has created new insight into the behaviour of dynein and the potential impact of mutations, and can be used as a springboard for further in-depth studies on the function and mechanisms of dynein.

Bibliography

[1] A.J. Roberts, T. Kon, P.J. Knight, K. Sutoh, and S.A. Burgess. Functions and mechanics of dynein motor proteins. Nature Reviews Molecular Cell Biology, 14(11):713–726, 2013.

[2] C.A. Garrett, M. Barri, A. Kuta, V. Soura, W. Deng, E.M.C. Fisher, G. Schiavo, and M. Hafezparast. Dync1h1 mutation alters transport kinetics and erk1/2-cfos signalling in a mouse model of distal spinal muscular atrophy. Brain, 137(7):1883–1893, 2014.

[3] M. Hafezparast, R. Klocke, C. Ruhrberg, A. Marquardt, A. Ahmad-Annuar, S. Bowen, G. Lalli, A.S. Witherden, H. Hummerich, S. Nicholson, P.J. Morgan, R. Oozageer, J.V. Priestley, S. Averill, V.R. King, S. Ball, J. Peters, T. Toda, A. Yamamoto, Y. Hiraoka, M. Augustin, D. Korthaus, S. Wattler, P. Wabnitz, C. Dickneite, S. Lampel, F. Boehme, G. Peraus, A. Popp, M. Rudelius, J. Schlegel, H. Fuchs, M.H. De Angelis, G. Schiavo, D.T. Shima, A.P. Russ, G. Stumm, J.E. Martin, and E.M.C. Fisher. Mutations in dynein link motor neuron degeneration to defects in retrograde transport. Science, 300(5620):808–812, 2003.

[4] G. Schiavo, L. Greensmith, M. Hafezparast, and E.M.C. Fisher. Cytoplasmic dynein heavy chain: The servant of many masters. Trends in Neurosciences, 36(11):641–651, 2013.

[5] M. Scoto, A.M. Rossor, M.B. Harms, S. Cirak, M. Calissano, S. Robb, A.Y. Manzur, A.M. Arroyo, A.R. Sanz, S. Mansour, P. Fallon, I. Hadjikoumi, A. Klein, M. Yang, M. De Visser, W.C.G.T. Overweg-Plandsoen, F. Baas, J.P. Taylor, M. Benatar, A.M. Connolly, M.T. Al-Lozi, J. Nixon, C.G.E.L. De Goede, A.R. Foley, C. McWilliam, M. Pitt, C. Sewry, R. Phadke, M. Hafezparast, W.K.K. Chong, E. Mercuri, R.H. Baloh, M.M. Reilly, and F. Muntoni. Novel mutations expand the clinical spectrum of dync1h1-associated spinal muscular atrophy. Neurology, 84(7):668–679, 2015.

[6] M. Schliwa and G. Woehlke. Molecular motors. Nature, 422(6933):759–765, 2003.

[7] P. Höök and R.B. Vallee. The dynein family at a glance. Journal of Cell Science, 119(21):4369–4371, 2006.

[8] B. Wickstead and K. Gull. Evolutionary biology of dyneins. In S.M. King, editor, Dyneins: Structure, Biology and Disease, chapter 2, pages 191–206. Academic Press, 2012.

[9] L. Crossley, C.A. Garrett, M. Hafezparast, and A. Madzvamuse. From the cell membrane to the nucleus: Unearthing transport mechanisms for dynein. Bulletin of Mathematical Biology, 74(9):2032–2061, 2012.

[10] Y.-S. Gao, C.C. Hubbert, and T.-P. Yao. The microtubule-associated histone deacetylase 6 (hdac6) regulates epidermal growth factor receptor (egfr) endocytic trafficking and degradation. Journal of Biological Chemistry, 285(15):11219–11226, 2010.

[11] T.D. Pollard, W.C. Earnshaw, and J. Lippincott-Schwartz. Cell Biology. Elsevier Inc, Philadelphia, 2nd edition, 2008.

[12] J.W. Murray and A.W. Wolkoff. Roles of the cytoskeleton and motor proteins in endocytic sorting. Advanced Drug Delivery Reviews, 55(11):1385–1403, 2003.

[13] A.G. Hendricks, E.L.F. Holzbaur, and Y.E. Goldman. Force measurements on cargoes in living cells reveal collective dynamics of microtubule motors. Proceedings of the National Academy of Sciences of the United States of America, 109(45):18447–18452, 2012.

[14] V. Soppina, A.K. Rai, A.J. Ramaiya, P. Barak, and R. Mallik. Tug-of-war between dissimilar teams of microtubule motors regulates transport and fission of endosomes. Proceedings of the National Academy of Sciences of the United States of America, 106(46):19381–19386, 2009.

[15] R.D. Vale. The molecular motor toolbox for intracellular transport. Cell, 112(4):467–480, 2003.

[16] E. Bananis, S. Nath, K. Gordon, P. Satir, R.J. Stockert, J.W. Murray, and A.W. Wolkoff. Microtubule-dependent movement of late endocytic vesicles in vitro: Requirements for dynein and kinesin. Molecular Biology of the Cell, 15(8):3688–3697, 2004.

[17] C.L. Brown, K.C. Maier, T. Stauber, L.M. Ginkel, L. Wordeman, I. Vernos, and T.A. Schroer. Kinesin-2 is a motor for late endosomes and lysosomes. Traffic, 6(12):1114–1124, 2005.

[18] O.J. Driskell, A. Mironov, V.J. Allan, and P.G. Woodman. Dynein is required for receptor sorting and the morphogenesis of early endosomes. Nature Cell Biology, 9(1):113–120, 2007.

[19] S. Hoepfner, F. Severin, A. Cabezas, B. Habermann, A. Runge, D. Gillooly, H. Stenmark, and M. Zerial. Modulation of receptor recycling and degradation by the endosomal kinesin kif16b. Cell, 121(3):437–450, 2005.

[20] S. Loubéry, C. Wilhelm, I. Hurbain, S. Neveu, D. Louvard, and E. Coudrier. Different microtubule motors move early and late endocytic compartments. Traffic, 9(4):492–509, 2008.

[21] M. Schuster, R. Lipowsky, M.-A. Assmann, P. Lenz, and G. Steinberg. Transient binding of dynein controls bidirectional long-range motility of early endosomes. Proceedings of the National Academy of Sciences of the United States of America, 108(9):3618–3623, 2011.

[22] N. Hirokawa, Y. Noda, Y. Tanaka, and S. Niwa. Kinesin superfamily motor proteins and intracellular transport. Nature Reviews Molecular Cell Biology, 10(10):682–696, 2009.

[23] A.G. Hendricks, E. Perlson, J.L. Ross, H.W. Schroeder III, M. Tokito, and E.L.F. Holzbaur. Motor coordination via a tug-of-war mechanism drives bidirectional vesicle transport. Current Biology, 20(8):697–702, 2010.

[24] A.G. Hendricks, A.E. Twelvetrees, and E.L.F. Holzbaur. Intracellular transport: New tools provide insights into multi-motor transport. Current Biology, 22(24):R1053–R1055, 2012.

[25] A.P. Carter, C. Cho, L. Jin, and R.D. Vale. Crystal structure of the dynein motor domain. Science, 331(6021):1159–1165, 2011.

[26] T. Kon, K. Sutoh, and G. Kurisu. X-ray structure of a functional full-length dynein motor domain. Nature Structural and Molecular Biology, 18(6):638–642, 2011.

[27] T. Kon, T. Oyama, R. Shimo-Kon, K. Imamula, T. Shima, K. Sutoh, and G. Kurisu. The 2.8Å crystal structure of the dynein motor domain. Nature, 484(7394):345–350, 2012. cited By 78.

[28] A.P. Carter. Crystal clear insights into how the dynein motor moves. Journal of Cell Science, 126(3):705–713, 2013.

[29] J. Lin, K. Okada, M. Raytchev, M.C. Smith, and D. Nicastro. Structural mechanism of the dynein power stroke. Nature Cell Biology, 16(5):479–485, 2014.

[30] S.L. Reck-Peterson, A. Yildiz, A.P. Carter, A. Gennerich, N. Zhang, and R.D. Vale. Single-molecule analysis of dynein processivity and stepping behavior. Cell, 126(2):335–348, 2006.

[31] M.A. DeWitt, A.Y. Chang, P.A. Combs, and A. Yildiz. Cytoplasmic dynein moves through uncoordinated stepping of the aaa+ ring domains. Science, 335(6065):221–225, 2012.

[32] W. Qiu, N.D. Derr, B.S. Goodman, E. Villa, D. Wu, W. Shih, and S.L. Reck-Peterson. Dynein achieves processive motion using both stochastic and coordinated stepping. Nature Structural and Molecular Biology, 19(2):193–201, 2012.

[33] W.J. Walter and S. Diez. Molecular motors: A staggering giant. Nature, 482(7383):44–45, 2012.

[34] M.N. Weedon, R. Hastings, R. Caswell, W. Xie, K. Paszkiewicz, T. Antoniadi, M. Williams, C. King, L. Greenhalgh, R. Newbury-Ecob, and S. Ellard. Exome sequencing identifies a dync1h1 mutation in a large pedigree with dominant axonal charcot-marie-tooth disease. American Journal of Human Genetics, 89(2):308–312, 2011.

[35] K.M. Ori-Mckenney, J. Xu, S.P. Gross, and R.B. Vallee. A cytoplasmic dynein tail mutation impairs motor processivity. Nature Cell Biology, 12(12):1228–1234, 2010.

[36] S. Sivagurunathan, R.R. Schnittker, S. Nandini, M.D. Plamann, and S.J. King. A mouse neurodegenerative dynein heavy chain mutation alters dynein motility and localization in neurospora crassa. Cytoskeleton, 69(9):613–624, 2012.

[37] W. Deng, C. Garrett, B. Dombert, V. Soura, G. Banks, E.M.C. Fisher, M.P. Van Der Brug, and M. Hafezparast. Neurodegenerative mutation in cytoplasmic dynein alters its organization and dynein-dynactin and dynein-kinesin interactions. Journal of Biological Chemistry, 285(51):39922–39934, 2010.

[38] J.R. Kardon and R.D. Vale. Regulators of the cytoplasmic dynein motor. Nature Reviews Molecular Cell Biology, 10(12):854–865, 2009.

[39] V.J. Allan. Cytoplasmic dynein. Biochemical Society Transactions, 39(5):1169–1178, 2011.

[40] R.B. Vallee, R.J. McKenney, and K.M. Ori-Mckenney. Multiple modes of cytoplasmic dynein regulation. Nature Cell Biology, 14(3):224–230, 2012.

[41] A.P. Carter, A.G. Diamant, and L. Urnavicius. How dynein and dynactin transport cargos: A structural perspective. Current Opinion in Structural Biology, 37:62–70, 2016.

[42] S.C. Tan, J. Scherer, and R.B. Vallee. Recruitment of dynein to late endosomes and lysosomes through light intermediate chains. Molecular Biology of the Cell, 22(4):467–477, 2011.

[43] H. Schmidt, E.S. Gleave, and A.P. Carter. Insights into dynein motor domain function from a 3.3-Å crystal structure. Nature Structural and Molecular Biology, 19(5):492–497, 2012.

[44] N. Billington and J.R. Sellers. Dynein struts its stuff. Nature Structural and Molecular Biology, 18(6):635–636, 2011.

[45] C. Cho and R.D. Vale. The mechanism of dynein motility: Insight from crystal structures of the motor domain. Biochimica et Biophysica Acta - Molecular Cell Research, 1823(1):182–191, 2012.

[46] P. Höök and R. Vallee. Dynein dynamics. Nature Structural and Molecular Biology, 19(5):467–469, 2012.

[47] E.S. Gleave, H. Schmidt, and A.P. Carter. A structural analysis of the aaa+ domains in saccharomyces cerevisiae cytoplasmic dynein. Journal of Structural Biology, 186(3):367–375, 2014.

[48] A.J. Roberts, B. Malkova, M.L. Walker, H. Sakakibara, N. Numata, T. Kon, R. Ohkura, T.A. Edwards, P.J. Knight, K. Sutoh, K. Oiwa, and S.A. Burgess. Atp-driven remodeling of the linker domain in the dynein motor. Structure, 20(10):1670–1680, 2012.

[49] H. Schmidt, R. Zalyte, L. Urnavicius, and A.P. Carter. Structure of human cytoplasmic dynein-2 primed for its power stroke. Nature, 518(7539):435–438, 2015.

[50] C. Cho, S.L. Reck-Peterson, and R.D. Vale. Regulatory atpase sites of cytoplasmic dynein affect processivity and force generation. Journal of Biological Chemistry, 283(38):25839–25845, 2008.

[51] T. Kon, M. Nishiura, R. Ohkura, Y.Y. Toyoshima, and K. Sutoh. Distinct functions of nucleotide-binding/hydrolysis sites in the four aaa modules of cytoplasmic dynein. Biochemistry, 43(35):11266–11274, 2004.

[52] M.P. Nicholas, F. Berger, L. Rao, S. Brenner, C. Cho, and A. Gennerich. Cytoplasmic dynein regulates its attachment to microtubules via nucleotide state-switched mechanosensing at multiple aaa domains. Proceedings of the National Academy of Sciences of the United States of America, 112(20):6371–6376, 2015.

[53] M.A. DeWitt, C.A. Cypranowska, F.B. Cleary, V. Belyy, and A. Yildiz. The aaa3 domain of cytoplasmic dynein acts as a switch to facilitate microtubule release. Nature Structural and Molecular Biology, 22(1):73–80, 2015.

[54] G. Bhabha, H.-C. Cheng, N. Zhang, A. Moeller, M. Liao, J.A. Speir, Y. Cheng, and R.D. Vale. Allosteric communication in the dynein motor domain. Cell, 159(4):857–868, 2014.

[55] S.A. Burgess, M.L. Walker, H. Sakakibara, P.J. Knight, and K. Oiwa. Dynein structure and power stroke. Nature, 421(6924):715–718, 2003.

[56] A.J. Roberts, N. Numata, M.L. Walker, Y.S. Kato, B. Malkova, T. Kon, R. Ohkura, F. Arisaka, P.J. Knight, K. Sutoh, and S.A. Burgess. Aaa+ ring and linker swing mechanism in the dynein motor. Cell, 136(3):485–495, 2009.

[57] N. Numata, T. Shima, R. Ohkura, T. Kon, and K. Sutoh. C-sequence of the dictyostelium cytoplasmic dynein participates in processivity modulation. FEBS Letters, 585(8):1185–1190, 2011.

[58] M.P. Nicholas, P. Höök, S. Brenner, C.L. Wynne, R.B. Vallee, and A. Gennerich. Control of cytoplasmic dynein force production and processivity by its c-terminal domain. Nature Communications, 6:6206, 2015.

[59] M.A. Gee, J.E. Heuser, and R.B. Vallee. An extended microtubule-binding structure within the dynein motor domain. Nature, 390(6660):636–639, 1997.

[60] A.P. Carter, J.E. Garbarino, E.M. Wilson-Kubalek, W.E. Shipley, C. Cho, R.A. Milligan, R.D. Vale, and I.R. Gibbons. Structure and functional role of dynein's microtubule-binding domain. Science, 322(5908):1691–1695, 2008.

[61] Y. Nishikawa, T. Oyama, N. Kamiya, T. Kon, Y.Y. Toyoshima, H. Nakamura, and G. Kurisu. Structure of the entire stalk region of the dynein motor domain. Journal of Molecular Biology, 426(19):3232–3245, 2014.

[62] W.B. Redwine, R. Hernández-López, S. Zou, J. Huang, S.L. Reck-Peterson, and A.E. Leschziner. Structural basis for microtubule binding and release by dynein. Science, 337(6101):1532–1536, 2012.

[63] I.R. Gibbons, J.E. Garbarino, C.E. Tan, S.L. Reck-Peterson, R.D. Vale, and A.P. Carter. The affinity of the dynein microtubule-binding domain is modulated by the conformation of its coiled-coil stalk. Journal of Biological Chemistry, 280(25):23960–23965, 2005.

[64] T. Kon, K. Imamula, A.J. Roberts, R. Ohkura, P.J. Knight, I.R. Gibbons, S.A. Burgess, and K. Sutoh. Helix sliding in the stalk coiled coil of dynein couples atpase and microtubule binding. Nature Structural and Molecular Biology, 16(3):325–333, 2009.

[65] H. Imai, T. Shima, K. Sutoh, M.L. Walker, P.J. Knight, T. Kon, and S.A. Burgess. Direct observation shows superposition and large scale flexibility within cytoplasmic dynein motors moving along microtubules. Nature Communications, 6:8179, 2015.

[66] A. Gennerich, A.P. Carter, S.L. Reck-Peterson, and R.D. Vale. Force-induced bidirectional stepping of cytoplasmic dynein. Cell, 131(5):952–965, 2007.

[67] G. Bhabha, G.T. Johnson, C.M. Schroeder, and R.D. Vale. How dynein moves along microtubules. Trends in Biochemical Sciences, 41(1):94–105, 2016.

[68] K. Imamula, T. Kon, R. Ohkura, and K. Sutoh. The coordination of cyclic microtubule association/dissociation and tail swing of cytoplasmic dynein. Proceedings of the National Academy of Sciences of the United States of America, 104(41):16134–16139, 2007.

[69] R.B. Vallee and P. Höök. A magnificent machine. Nature, 421(6924):701–702, 2003.

[70] A.P. Carter and R.D. Vale. Communication between the aaa+ ring and microtubule-binding domain of dynein. Biochemistry and Cell Biology, 88(1):15–21, 2010.

[71] T. Shima, K. Imamula, T. Kon, R. Ohkura, and K. Sutoh. Head-head coordination is required for the processive motion of cytoplasmic dynein, an aaa+ molecular motor. Journal of Structural Biology, 156(1):182–189, 2006.

[72] A. Gennerich and R.D. Vale. Walking the walk: how kinesin and dynein coordinate their steps. Current Opinion in Cell Biology, 21(1):59–67, 2009.

[73] V. Belyy, N.L. Hendel, A. Chien, and A. Yildiz. Cytoplasmic dynein transports cargos via load-sharing between the heads. Nature Communications, 5:5544, 2014.

[74] R.J. McKenney, S.J. Weil, J. Scherer, and R.B. Vallee. Mutually exclusive cytoplasmic dynein regulation by nude-lis1 and dynactin. Journal of Biological Chemistry, 286(45):39615–39622, 2011.

[75] E. Barbar. Native disorder mediates binding of dynein to nude and dynactin. Biochemical Society Transactions, 40(5):1009–1013, 2012.

[76] M.J. Egan, K. Tan, and S.L. Reck-Peterson. Lis1 is an initiation factor for dynein-driven organelle transport. Journal of Cell Biology, 197(7):971–982, 2012.

[77] J. Huang, A.J. Roberts, A.E. Leschziner, and S.L. Reck-Peterson. Lis1 acts as a "clutch" between the atpase and microtubule-binding domains of the dynein motor. Cell, 150(5):975–986, 2012.

[78] M.A. Schlager, H.T. Hoang, L. Urnavicius, S.L. Bullock, and A.P. Carter. In vitro reconstitution of a highly processive recombinant human dynein complex. EMBO Journal, 33(17):1855–1868, 2014.

[79] S.J. King and T.A. Schroer. Dynactin increases the processivity of the cytoplasmic dynein motor. Nature Cell Biology, 2(1):20–24, 2000.

[80] J.R. Kardon, S.L. Reck-Peterson, and R.D. Vale. Regulation of the processivity and intracellular localization of saccharomyces cerevisiae dynein by dynactin. Proceedings of the National Academy of Sciences of the United States of America, 106(14):5669–5674, 2009.

[81] N. Flores-Rodriguez, S.S. Rogers, D.A. Kenwright, T.A. Waigh, P.G. Woodman, and V.J. Allan. Roles of dynein and dynactin in early endosome dynamics revealed using automated tracking and global analysis. PLoS ONE, 6(9):e24479, 2011.

[82] J.L. Ross, K. Wallace, H. Shuman, Y.E. Goldman, and E.L.F. Holzbaur. Processive bidirectional motion of dynein-dynactin complexes in vitro. Nature Cell Biology, 8(6):562–570, 2006.

[83] S. Toba, T.M. Watanabe, L. Yamaguchi-Okimoto, Y.Y. Toyoshima, and H. Higuchi. Overlapping hand-over-hand mechanism of single molecular motility of cytoplasmic dynein. Proceedings of the National Academy of Sciences of the United States of America, 103(15):5741–5745, 2006.

[84] J. Xu and S. P. Gross. Biophysics of dynein in vivo. In S.M. King, editor, Dyneins: Structure, Biology and Disease, chapter 6, pages 191–206. Academic Press, 2012.

[85] R. Mallik, B.C. Carter, S.A. Lex, S.J. King, and S.P. Gross. Cytoplasmic dynein functions as a gear in response to load. Nature, 427(6975):649–652, 2004.

[86] X.J. Chen, E.N. Levedakou, K.J. Millen, R.L. Wollmann, B. Soliven, and B. Popko. Proprioceptive sensory neuropathy in mice with a mutation in the cytoplasmic dynein heavy chain 1 gene. Journal of Neuroscience, 27(52):14515–14524, 2007.

[87] C. Fiorillo, F. Moro, J. Yi, S. Weil, G. Brisca, G. Astrea, M. Severino, A. Romano, R. Battini, A. Rossi, C. Minetti, C. Bruno, F.M. Santorelli, and R. Vallee. Novel dynein dync1h1 neck and motor domain mutations link distal spinal muscular atrophy and abnormal cortical development. Human Mutation, 35(3):298–302, 2014.

[88] G.T. Banks, M.A. Haas, S. Line, H.L. Shepherd, M. Alqatari, S. Stewart, I. Rishal, A. Philpott, B. Kalmar, A. Kuta, M. Groves, N. Parkinson, A. Acevedo-Arozena, S. Brandner, D. Bannerman, L. Greensmith, M. Hafezparast, M. Koltzenburg, R. Deacon, M. Fainzilber, and E.M.C. Fisher. Behavioral and other phenotypes in a cytoplasmic dynein light intermediate chain 1 mutant mouse. Journal of Neuroscience, 31(14):5483–5494, 2011.

[89] A. Wynshaw-Boris. Lissencephaly and lis1: Insights into the molecular mechanisms of neuronal migration and development. Clinical Genetics, 72(4):296–304, 2007.

[90] J. Eschbach and L. Dupuis. Cytoplasmic dynein in neurodegeneration. Pharmacology and Therapeutics, 130(3):348–363, 2011.

[91] G. Lan and S.X. Sun. Mechanochemical models of processive molecular motors. Molecular Physics, 110(9-10):1017–1034, 2012.

[92] S.I. Rubinow and J.J. Blum. A theoretical approach to the analysis of axonal transport. Biophysical Journal, 30(1):137–147, 1980.

[93] I.A. Kuznetsov and A.V. Kuznetsov. Modeling anterograde and retrograde transport of short mobile microtubules from the site of axonal branch formation. Journal of Biological Physics, 40(1):41–53, 2014.

[94] J. Gou, L. Edelstein-Keshet, and J. Allard. Mathematical model with spatially uniform regulation explains long-range bidirectional transport of early endosomes in fungal hyphae. Molecular Biology of the Cell, 25(16):2408–2415, 2014.

[95] D.A. Smith and R.M. Simmons. Models of motor-assisted transport of intracellular particles. Biophysical Journal, 80(1):45–68, 2001.

[96] A. Friedman and G. Craciun. A model of intracellular transport of particles in an axon. Journal of Mathematical Biology, 51(2):217–246, 2005.

[97] A.T. Dinh, C. Pangarkar, T. Theofanous, and S. Mitragotri. Theory of spatial patterns of intracellular organelles. Biophysical Journal, 90(10):L67–L69, 2006.

[98] A.V. Kuznetsov and K. Hooman. Modeling traffic jams in intracellular transport in axons. International Journal of Heat and Mass Transfer, 51(23-24):5695–5699, 2008.

[99] K. Sadegh Zadeh and S.B. Shah. Mathematical modeling and parameter estimation of axonal cargo transport. Journal of Computational Neuroscience, 28(3):495–507, 2010.

[100] A.V. Kuznetsov. Coupling a dynein transport model with a model of anterograde and retrograde transport of intracellular organelles. International Communications in Heat and Mass Transfer, 38(7):833–837, 2011.

[101] A.V. Kuznetsov. Modeling of retrograde nanoparticle transport in axons and dendrites. International Communications in Heat and Mass Transfer, 38(5):543–547, 2011.

[102] R. Lipowsky, S. Klumpp, and T.M. Nieuwenhuizen. Random walks of cytoskeletal motors in open and closed compartments. Physical Review Letters, 87(10):108101/1–108171/3, 2001.

[103] S. Klumpp and R. Lipowsky. Traffic of molecular motors through tube-like compartments. Journal of Statistical Physics, 113(1-2):233–268, 2003.

[104] S. Klumpp and R. Lipowsky. Asymmetric simple exclusion processes with diffusive bottlenecks. Physical Review E - Statistical, Nonlinear, and Soft Matter Physics, 70(6 2):066104/1–066104/9, 2004.

[105] M.J.I. Müller, S. Klumpp, and R. Lipowsky. Molecular motor traffic in a half-open tube. Journal of Physics Condensed Matter, 17(47):S3839–S3850, 2005.

[106] S. Klumpp and R. Lipowsky. Active diffusion of motor particles. Physical Review Letters, 95(26):268102, 2005.

[107] S. Klumpp, T.M. Nieuwenhuizen, and R. Lipowsky. Self-organized density patterns of molecular motors in arrays of cytoskeletal filaments. Biophysical Journal, 88(5):3118–3132, 2005.

[108] Y. Chai, R. Lipowsky, and S. Klumpp. Transport by molecular motors in the presence of static defects. Journal of Statistical Physics, 135(2):241–260, 2009.

[109] Y. Chai, S. Klumpp, M.J.I. Müller, and R. Lipowsky. Traffic by multiple species of molecular motors. Physical Review E - Statistical, Nonlinear, and Soft Matter Physics, 80(4):041928, 2009.

[110] P. Ashwin, C. Lin, and G. Steinberg. Queueing induced by bidirectional motor motion near the end of a microtubule. Physical Review E - Statistical, Nonlinear, and Soft Matter Physics, 82(5):051907, 2010.

[111] M. Schuster, S. Kilaru, P. Ashwin, C. Lin, N.J. Severs, and G. Steinberg. Controlled and stochastic retention concentrates dynein at microtubule ends to keep endosomes on track. EMBO Journal, 30(4):652–664, 2011.

[112] C. Lin, P. Ashwin, and G. Steinberg. Motor-mediated bidirectional transport along an antipolar microtubule bundle: A mathematical model. Physical Review E - Statistical, Nonlinear, and Soft Matter Physics, 87(5):052709, 2013.

[113] R. Juhász. Weakly coupled, antiparallel, totally asymmetric simple exclusion processes. Physical Review E - Statistical, Nonlinear, and Soft Matter Physics, 76(2):021117, 2007.

[114] R. Juhász. Dynamics at barriers in bidirectional two-lane exclusion processes. Journal of Statistical Mechanics: Theory and Experiment, 2010(3):P03010, 2010.

[115] M. Ebbinghaus and L. Santen. A model for bidirectional traffic of cytoskeletal motors. Journal of Statistical Mechanics: Theory and Experiment, 2009(3):P03030, 2009.

[116] M. Ebbinghaus, C. Appert-Rolland, and L. Santen. Bidirectional traffic on microtubules. Lecture Notes in Computer Science (including subseries Lecture Notes in Artificial Intelligence and Lecture Notes in Bioinformatics), 6350 LNCS:542–551, 2010.

[117] S. Klumpp and R. Lipowsky. Cooperative cargo transport by several molecular motors. Proceedings of the National Academy of Sciences of the United States of America, 102(48):17284–17289, 2005.

[118] M.J.I. Müller, S. Klumpp, and R. Lipowsky. Tug-of-war as a cooperative mechanism for bidirectional cargo transport by molecular motors. Proceedings of the National Academy of Sciences of the United States of America, 105(12):4609–4614, 2008.

[119] M.J.I. Müller, S. Klumpp, and R. Lipowsky. Motility states of molecular motors engaged in a stochastic tug-of-war. Journal of Statistical Physics, 133(6):1059–1081, 2008.

[120] M.J.I. Müller, S. Klumpp, and R. Lipowsky. Bidirectional transport by molecular motors: enhanced processivity and response to external forces. Biophysical Journal, 98(11):2610–2618, 2010.

[121] F. Berger, C. Keller, S. Klumpp, and R. Lipowsky. Distinct transport regimes for two elastically coupled molecular motors. Physical Review Letters, 108(20):208101, 2012.

[122] F. Berger, C. Keller, R. Lipowsky, and S. Klumpp. Elastic coupling effects in cooperative transport by a pair of molecular motors. Cellular and Molecular Bioengineering, 6(1):48–64, 2013.

[123] F. Berger, C. Keller, S. Klumpp, and R. Lipowsky. External forces influence the elastic coupling effects during cargo transport by molecular motors. Physical Review E - Statistical, Nonlinear, and Soft Matter Physics, 91(2):022701, 2015.

[124] A. Kunwar, M. Vershinin, J. Xu, and S.P. Gross. Stepping, strain gating, and an unexpected force-velocity curve for multiple-motor-based transport. Current Biology, 18(16):1173–1183, 2008.

[125] C.B. Korn, S. Klumpp, R. Lipowsky, and U.S. Schwarz. Stochastic simulations of cargo transport by processive molecular motors. Journal of Chemical Physics, 131(24):245107, 2009.

[126] J.W. Driver, A.R. Rogers, D.K. Jamison, R.K. Das, A.B. Kolomeisky, and M.R. Diehl. Coupling between motor proteins determines dynamic behaviors of motor protein assemblies. Physical Chemistry Chemical Physics, 12(35):10398–10405, 2010.

[127] S. Liepelt and R. Lipowsky. Kinesin's network of chemomechanical motor cycles. Physical Review Letters, 98(25):258102, 2007.

[128] S. Liepelt and R. Lipowsky. Steady-state balance conditions for molecular motor cycles and stochastic nonequilibrium processes. EPL, 77(5):50002, 2007.

[129] R. Lipowsky and S. Liepelt. Chemomechanical coupling of molecular motors: Thermodynamics, network representations, and balance conditions. Journal of Statistical Physics, 130(1):39–67, 2008.

[130] S. Liepelt and R. Lipowsky. Operation modes of the molecular motor kinesin. Physical Review E - Statistical, Nonlinear, and Soft Matter Physics, 79(1):011917, 2009.

[131] S. Liepelt and R. Lipowsky. Impact of slip cycles on the operation modes and efficiency of molecular motors. Journal of Statistical Physics, 141(1):1–16, 2010.

[132] C. Keller, F. Berger, S. Liepelt, and R. Lipowsky. Network complexity and parametric simplicity for cargo transport by two molecular motors. Journal of Statistical Physics, 150(2):205–234, 2013.

[133] J. Munárriz, J.J. Mazo, and F. Falo. Model for hand-over-hand motion of molecular motors. Physical Review E - Statistical, Nonlinear, and Soft Matter Physics, 77(3):031915, 2008.

[134] M. Bier. Brownian ratchets in physics and biology. Contemporary Physics, 38(6):371–379, 1997.

[135] M. Bier. Processive motor protein as an overdamped brownian stepper. Physical Review Letters, 91(14):148104/1–148104/4, 2003.

[136] M. Bier. Modelling processive motor proteins: Moving on two legs in the microscopic realm. Contemporary Physics, 46(1):41–51, 2005.

[137] M. Bier. The stepping motor protein as a feedback control ratchet. BioSystems, 88(3):301–307, 2007.

[138] M. Bier. The energetics, chemistry, and mechanics of a processive motor protein. BioSystems, 93(1-2):23–28, 2008.

[139] M. Bier and F.J. Cao. How occasional backstepping can speed up a processive motor protein. BioSystems, 103(3):355–359, 2011.

[140] Y. Zhang. Three phase model of the processive motor protein kinesin. Biophysical Chemistry, 136(1):19–22, 2008.

[141] Y. Zhang. A general two-cycle network model of molecular motors. Physica A: Statistical Mechanics and its Applications, 388(17):3465–3474, 2009.

[142] M.E. Fisher and A.B. Kolomeisky. Molecular motors and the forces they exert. Physica A: Statistical Mechanics and its Applications, 274(1):241–266, 1999.

[143] M.E. Fisher and A.B. Kolomeisky. Simple mechanochemistry describes the dynamics of kinesin molecules. Proceedings of the National Academy of Sciences of the United States of America, 98(14):7748–7753, 2001.

[144] Y. Zhang and M.E. Fisher. Measuring the limping of processive motor proteins. Journal of Statistical Physics, 142(6):1218–1251, 2011.

[145] Y. Imafuku, N. Thomas, and K. Tawada. Hopping and stalling of processive molecular motors. Journal of Theoretical Biology, 261(1):43–49, 2009.

[146] A.G. Hendricks, B.I. Epureanu, and E. Meyhöfer. Mechanistic mathematical model of kinesin under time and space fluctuating loads. Nonlinear Dynamics, 53(4):303–320, 2008.

[147] B. Lisowski, T. Kuśmierz, M. Zabicki, and M. Bier. Cargo-mooring as an operating principle for molecular motors. Journal of Theoretical Biology, 374:26–34, 2015.

[148] B. Lisowski, D. Valenti, B. Spagnolo, M. Bier, and E. Gudowska-Nowak. Stepping molecular motor amid lévy white noise. Physical Review E - Statistical, Nonlinear, and Soft Matter Physics, 91(4):042713, 2015.

[149] Y. Jamali, M.E. Foulaadvand, and H. Rafii-Tabar. Computational modeling of the collective stochastic motion of kinesin nano motors. Journal of Computational and Theoretical Nanoscience, 7(1):146–152, 2010.

[150] M.P. Singh, R. Mallik, S.P. Gross, and C.C. Yu. Monte carlo modeling of single-molecule cytoplasmic dynein. Proceedings of the National Academy of Sciences of the United States of America, 102(34):12059–12064, 2005.

[151] S. Mukherji. Model for the unidirectional motion of a dynein molecule. Physical Review E - Statistical, Nonlinear, and Soft Matter Physics, 77(5):051916, 2008.

[152] D. Tsygankov, A.W.R. Serohijos, N.V. Dokholyan, and T.C. Elston. Kinetic models for the coordinated stepping of cytoplasmic dynein. Journal of Chemical Physics, 130(2):025101, 2009.

[153] D. Tsygankov, A.W.R. Serohijos, N.V. Dokholyan, and T.C. Elston. A physical model reveals the mechanochemistry responsible for dynein's processive motion. Biophysical Journal, 101(1):144–150, 2011.

[154] A. Šarlah and A. Vilfan. The winch model can explain both coordinated and uncoordinated stepping of cytoplasmic dynein. Biophysical Journal, 107(3):662–671, 2014.

[155] W. Zheng. Coarse-grained modeling of the structural states and transition underlying the powerstroke of dynein motor domain. Journal of Chemical Physics, 136(15):155103, 2012.

[156] J. Howard. Mechanics of Motor Proteins and the Cytoskeleton. Sinauer Associates Inc, Sunderland, USA, 2001.

[157] G. Zhang. Computational Bioengineering. CRC Press, Boca Raton, USA, 2015.

[158] Y. Bakhshan and A. Omidvar. Calculation of friction coefficient and analysis of fluid flow in a stepped micro-channel for wide range of knudsen number using lattice boltzmann (mrt) method. Physica A: Statistical Mechanics and its Applications, 440:161–175, 2015.

[159] Invitrogen - Life Technologies Corporation. Personal communication, 2012.

[160] C.K. Mathews, K.E. van Holde, and K.G. Ahern. Biochemistry. Addison Wesley Longman Inc, San Francisco, 3rd edition, 2000.

[161] S. Mitragotri and J. Lahann. Physical approaches to biomaterial design. Nature Materials, 8(1):15–23, 2009.

[162] S.C. Schaffner and J.V. José. Biophysical model of self-organized spindle formation patterns without centrosomes and kinetochores. Proceedings of the National Academy of Sciences of the United States of America, 103(30):11166–11171, 2006.

[163] J.W. Wojcieszyn, R.A. Schlegel, E.S. Wu, and K.A. Jacobson. Diffusion of injected macromolecules within the cytoplasm of living cells. Proceedings of the National Academy of Sciences of the United States of America, 78(7 I):4407–4410, 1981.

[164] MATLAB. R2014a. The Mathworks, Inc, Natick, Massachusetts, 2014.

[165] L. Crossley. Modelling the dynamics of mutant dynein in a model for nuerodegeneration. Master's thesis, University of Sussex, 2012.